ISSN 1732-9353 (suspended)
eISSN 2543-7496

Scientific Review

Engineering and Environmental Sciences

Przegląd Naukowy
Inżynieria i Kształtowanie Środowiska

Vol. 32 (2) 2023 Issue 100
Quarterly

SCIENTIFIC REVIEW
ENGINEERING AND ENVIRONMENTAL SCIENCES
Quarterly

EDITORIAL OFFICE ADDRESS
Wydział Budownictwa i Inżynierii Środowiska SGGW, ul. Nowoursynowska 159, 02-776 Warsaw, Poland
tel. (+48 22) 59 35 363, 59 35 210, 59 35 302
e-mail: srees@sggw.edu.pl
https://srees.sggw.edu.pl

Electronic version of the Scientific Review Engineering and Environmental Sciences is primary version

All papers are indexed in the data bases as follows: AGRO(Poznań), BazTech, Biblioteka Nauki, **CrossRef**, **DOAJ**, **Google Scholar**, **Index Copernicus**, INFONA, POL-Index, **SCOPUS**, SIGŻ(CBR)

Scientific Review

Engineering and Environmental Sciences

Przegląd Naukowy

Inżynieria i Kształtowanie Środowiska

Vol. 32 (2) 2023 Issue 100

Contents

Wydawnictwo SGGW, Warsaw 2023

Wydawnictwo SGGW wydawnictwosggw

Editorial work – Anna Dołomisiewicz, Violetta Kaska, Tomasz Ruchniewicz

ISSN 1732-9353 (suspended) eISSN 2543-7496

Scientific Review Engineering and Environmental Sciences (2023), 32 (2), 101–116

Sci. Rev. Eng. Env. Sci. (2023), 32 (2) https://srees.sggw.edu.pl

ISSN 1732-9353 (suspended) eISSN 2543-7496 DOI 10.22630/srees.4743

Received: 22.01.2023
Accepted: 30.03.2023

Haider K. AMMASH https://orcid.org/0000-0003-3672-6295

Noora N. SHAFFAF✉ https://orcid.org/0000-0002-8624-203X

University of Al-Qadisiyah, College of Engineering, Al-Qadisiyah, Iraq

Behavior study of the steel plate girder with a cellular honeycomb web

Keywords: finite element analysis, steel plate girder, honeycomb web, corrugated web, shear strength, web failure, shear stress, numerical analysis

Introduction

Steel plate girders with corrugated webs can enhance their shear strength against web buckling and circumvent steel's mass reduction issues (De'nan & Hashim, 2013). The purpose of this study is to investigate the shear behavior and failure mode of hollow honeycomb steel plate web girders (HWsG) numerically and to compare the finite element (FE) research with the authors' experimental programs that were carried out by Shaffaf and Ammash (2022). Various researchers have examined the shear buckling behavior of the corrugated steel plate web. Under concentrated load, Ammash and Dashi (2022) studied the shear behavior of inclined and vertical corrugated steel plate web girders. They created fourteen specimens with varying modes, angles, and depths of web corrugation. Compared to the flat web, they obtained an increase in ultimate load of inclined corrugated web shear

✉eng.civil.20.mas.18@qu.edu.iq

resistance of 49–79% for 300 mm depth and 49.3–103.0%. Ammash and Kadhim (2022) calculated the shear behavior of a concrete-filled core sandwich corrugated steel plate web girder. The authors constructed and tested sixteen specimens of simply supported girders under concentrated load. The composite core sandwich web girders demonstrated a 29–36% increase in the web shear compared to the flat web. The trapezoidal corrugated web was utilized to fabricate eight-steel plate web girders by Nie, Zhu, Tao and Tang (2013). The ANSYS was chosen as the software to be used for this investigation. A concentration was applied to all eight models in the middle of the span. According to the findings of the calculations, the load-carrying capacity values of the trapezoidal corrugated web recorders are greater than those of the flat web. Abbas, Ibrahim and Korashy (2019) presented an experimental thesis and numerical analysis with multiple parameters, including the web depth, width, corrugation angle, and plate thickness. They concluded that corrugation angles could improve web shear resistance. Pasternak and Kubieniec (2010), Hassanein, Salem and Mohmoud (2018) investigated the shear behavior of trapezoidal and sinusoidal webs subjected to two concentrated loads. They gained on the progression of steel web strength. Leblouba, Barakat and Al-Saadon (2018) evaluated the web geometry and shear web strength properties of nine plate girder specimens with trapezoidal corrugated web until failure. They concluded that the width of the corrugated web has a negative relationship with shear strength. Ammash and Al-Bader (2021) investigated the shear behavior of core sandwich corrugated steel plate web I-section girders experimentally and numerically. They constructed ten steel plate girders with simple support and tested them under a midspan concentrated load. Three different trapezoidal, triangular, and rectangular corrugated steel web patterns were manufactured, with differences in corrugation widths (20 mm, 40 mm and 60 mm) and corrugation angles (90° and 45°). The results demonstrated that the trapezoidal corrugated web had a higher ultimate load value than flat web and other web modes by a ratio of 28%. Shaffaf and Ammash (2022) investigated the shear behavior of honeycomb steel web girders through an experimental study. Twelve honeycomb web girders with simple support were tested under a concentrated midspan load. The girders were divided into three groups: 60 mm, 80 mm and 100 mm thick honeycomb webs. The steel plate thickness of honeycomb web (HW) was 0.70 mm, 600 mm, 1,200 mm and 1,800 mm lengths were fabricated for each HW specimen. The experimental test results demonstrated that the 60 mm honeycomb corrugation width provided a higher ultimate load than the flat web. Figure 1 depicts the specimen's deformed shape.

FIGURE 1. Deformation shape of steel plate honeycomb web girders: A – girder with 60 mm HW corrugation width and 600 mm length ($HW60L_1$); B – girder with 60 mm HW corrugation width and 1,200 mm length ($HW60L_2$); C – girder with 60 mm HW corrugation width and 1,800 mm length ($HW60L_3$); D – girder with 80 mm corrugation width and 600 mm length ($HW80L_1$); E – honeycomb girder with 80 mm corrugation width and 1,200 mm length ($HW80L_2$); F – girder with 80 mm corrugation width and 1,800 mm length ($HW80L_3$); G – girder with 100 mm HW corrugation width and 600 mm length ($HW100L_1$); H – girder with 100 mm web corrugation width and 1,200 mm length ($HW100L_2$); I – honeycomb girder with 100 mm HW corrugation width and 1,800 mm length ($HW100L_3$)

Source: own work adopted from Shaffaf and Ammash (2022).

Material and methods

This paper is distinguished by a numerical investigation and numerically comparing the test results of the previous experimental work by Shaffaf and Ammash (2022) with the finite element analysis results of the current study. Shaffaf and Ammash (2022) constructed twelve simply supported girders with honeycomb web steel plates

(HSW) and tested them with a concentrated midspan load. Twelve simply supported girders were tested at the University of Al-Qadisiyah Structures Laboratory, and the results were recorded. In this paper, honeycomb web specimens were modelled with a three-dimensional analysis (3D), reduced integration, and shell elements (3D-S4R) in Abaqus software with six degrees of freedom per node and simulated with exactly the same mechanical properties and details of the corresponding material of the steel plate that had been used in the experimental study. The details including dimensions, properties, loading method, and boundary conditions of all specimens of simply supported ends. Experimentally, the mechanical properties and the tensile test method was conducted in accordance with the American Institute of Steel Construction specifications (American Institute of Steel Construction [AISC], 2016). All steel plate girder specimens have the same web depth (300 mm), while the steel plate thicknesses for the flat and honeycomb webs are 2 mm and 0.70 mm, respectively. The width of the flange was 200 mm, while the thickness and width of the constant flange were 6 mm and 200 mm, respectively. The girder length of each group varies among 600 mm, 1,200 mm and 1,800 mm. The twelve specimens were divided into four groups: flat, honeycomb steel web with a 60 mm corrugation width (HW60), honeycomb steel web with a 80 mm corrugation width (HW80), and with a 100 mm corrugation width of the honeycomb web (HW100). Each group was fabricated with aspect ratios of 1%, 2% and 3% for three 600 mm, 1,200 mm and 1,800 mm, respectively. All specimens were tested with a concentrated midspan load. Furthermore, the boundary conditions were simulated in the Abaqus software using the load option to prevent displacements and rotations in all directions [$X(U_1)$, $Y(U_2)$ and $Z(U_3)$] at the pin-supported end, while at the roller-supported end, rotations and displacements were prevented in the X and Y directions [$X(U_1)$ and $Y(U_2) = 0$]. The finite element meshing size of all simulated simply supported girders was 10 mm. The 10 mm mesh size gives a very close load displacement curve compared with the experimental test results. The details of the finite element models (FEM) for the honeycomb web steel plate girder model are shown in Figure 2.

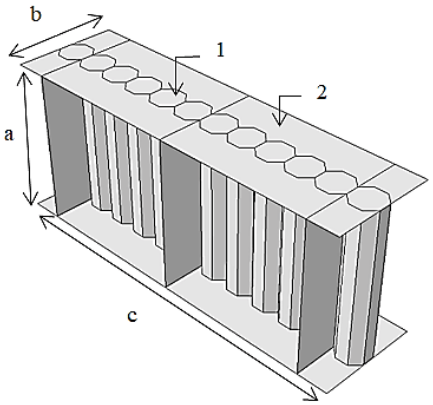

FIGURE 2. Finite element model of steel plate honeycomb steel web girder: a – web depth; b – flange width; c – girder length; 1 – honeycomb steel web; 2 – steel web

Source: Ammash and Shaffaf (2022).

Results and discussion

This section will discuss the validation of the FE analysis results obtained from Shaffaf and Ammash (2022) experimental test results. Table 1 compares twelve steel plate I-girders with two web modes (flat web and honeycomb web) that are simply supported. Figures 3 and 4 depict the comparison between load and deflection. Figure 5 illustrates two varieties of shear web buckling failure (global and interactive shear buckling). The corrugated web geometry can influence the shear buckling mode. The global buckling is almost all of the web failure that occurs at the web panel with the flat mode due to the applied shear stress. Global buckling was only observed at the web panel of the flat web girder, whereas intermediate buckling or interactive shear buckling was observed at most honeycomb web corrugations (Fig. 5B). Also, Figure 3A illustrates a good correlation between the two studies' load-carrying capacities (the experimental and present FEM study). The results indicate a slight increase in the shear buckling strength of the HW specimens, particularly $HW60L_1$, which recorded a higher ultimate load than FWL_1 and other HW corrugations (80 mm and 100 mm) due to an increase in the slenderness ratio of cross-section of the honey-

TABLE 1. Comparison between Shaffaf and Ammash (2022) experimental test results and the finite element analysis of the present research

Girder	Ultimate load (Pu, ex) [kN]	Ultimate load (Pu, FE) [kN]	$\frac{Pu,FE\_Pu,ex}{Pu,ex}$ [%]	Failure mode
FWL_1	132	137.0	3.6	global buckling
FWL_2	110	108.7	–1.2	global buckling
FWL_3	105	110.6	5.3	global buckling
$HW60L_1$	142	129.5	–8.8	interactive buckling
$HW60L_2$	116	118.9	2.5	interactive buckling
$HW60L_3$	110	114.0	3.6	interactive buckling
$HW80L_1$	126	126.0	0.0	interactive buckling
$HW80L_2$	118	121.0	2.5	interactive buckling
$HW80L_3$	98	102.0	4.0	interactive buckling
$HW100L_1$	93	97.12	4.5	interactive buckling
$HW100L_2$	80	81.3	1.6	interactive buckling
$HW100L_3$	72	69.5	0.0	interactive buckling

L_1, L_2, L_3 refers to 600 mm, 1,200 mm and 1,800 mm, respectively.

Source: own work adopted from Shaffaf and Ammash (2022).

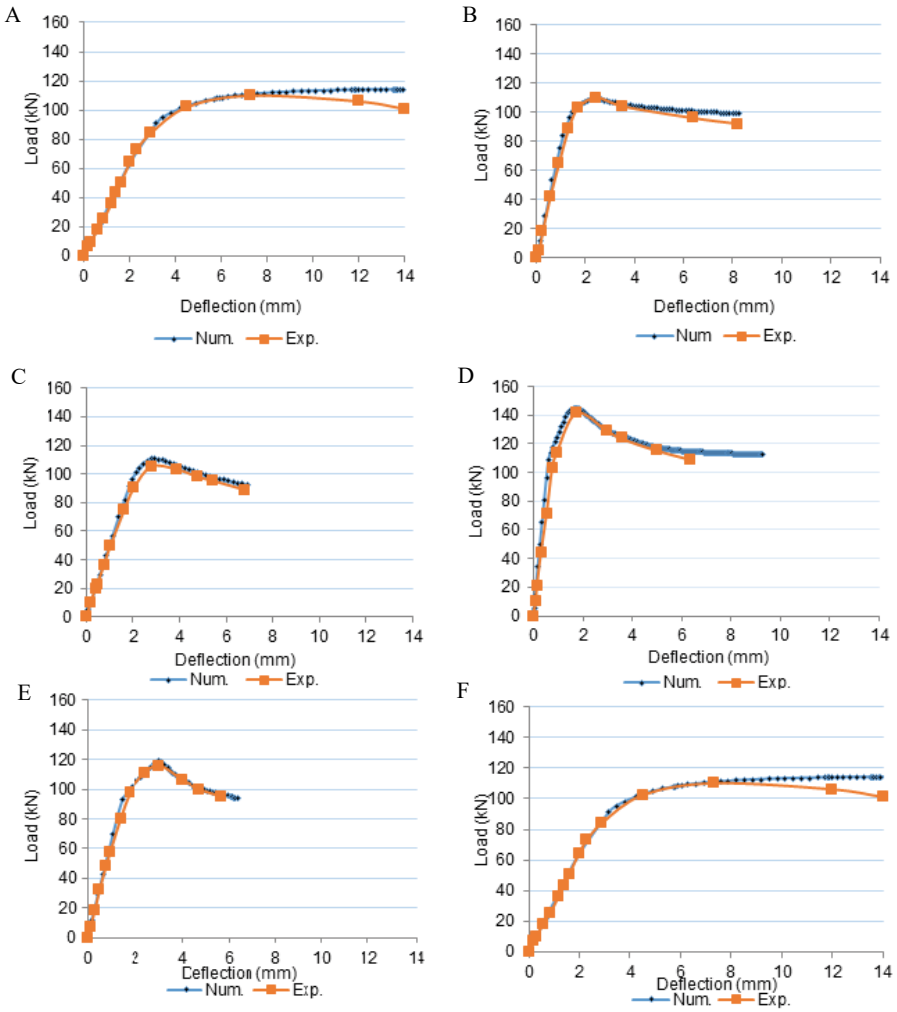

FIGURE 3. Comparison of the load–deflection curves between the experimental test results of Shaffaf and Ammash (2022) and finite element investigation of the current research: A – FWL_1 specimens; B – FWL_2 specimens; C – FWL_3 specimens; D – $HW60L_1$ specimens; E – $HW60L_2$ specimens; F – $HW60L_3$ specimens

Source: own work adopted from Shaffaf and Ammash (2022).

comb web as corrugation dimension increases. Furthermore, when the corrugation dimension of the honeycomb web decreases, the moment of inertia of the minor axis or Y axis increase, because the inside empty spacing between the hollow honeycomb cell decreases which can reduce the web shear strength. Table 1 illustrates the maximum difference of the load carrying capacity between the numerical and experimental results was 8.8% from the comparison results of honeycomb steel web

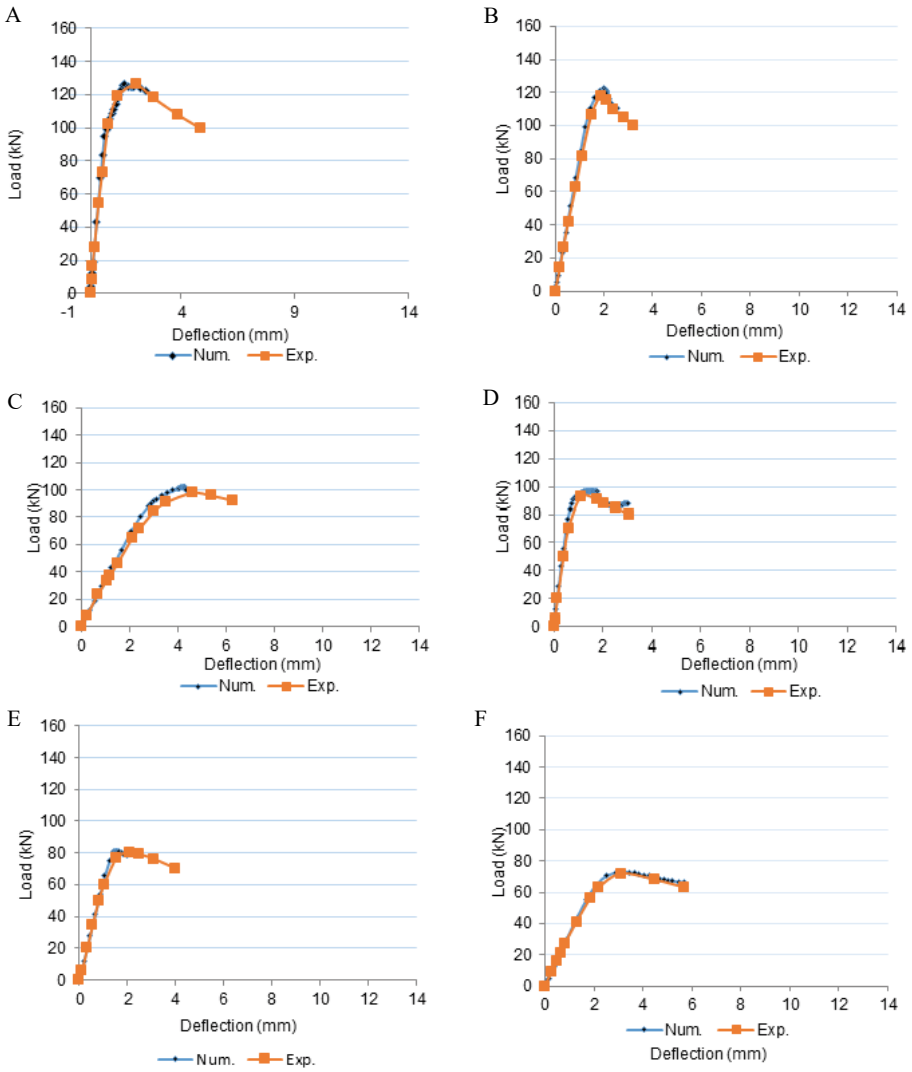

FIGURE 4. Comparison of the load–deflection curves between the experimental test results of Shaffaf and Ammash (2022) and finite element investigation of the current research: A – $HW80L_1$ specimens; B – $HW80L_2$ specimens; C – $HW80L_3$ specimens; D – $HW100L_1$ specimens; E – $HW100L_2$ specimens; F – $HW100L_2$ specimens

Source: own work adopted from Shaffaf and Ammash (2022).

with 60 mm thick ($HW60L_1$). This ratio indicates that the current simulated models of the flat web and the honeycomb web I-girder specimens is able to estimate shear behavior, buckling modes, ultimate load and maximum midspan deflection of all plate girder in this paper.

Figures 3A, 3B and 3C illustrate the load carrying capacity of the flat steel web girders with 600 mm, 1,200 mm and 1,800 mm length, respectively. The FWL_1 specimen recorded 132 kN. This value is greater than other specimens of flat web FWL_2 and FWL_3 due to increasing in the shear span to depth ratio from 1 to 2% and 3% for FWL_1, FWL_2 and FWL_3, respectively. The aspect ratio (a/d) has inverse relation with the web shear strength. The load carrying capacity verse maximum middle displacement that is illustrated in Figure 3 indicates the appropriate comparison between the experimental test results and FE investigation of this paper.

Figure 3D shows the FE results and the experimental test result of honeycomb web plate girder 60 mm thick. The increase in the load carrying capacity and decrease in the maximum displacement of girder midspan was clearly noticed. The $HW60L_1$ specimens recorded an enhancement in the web shear strength, which reaches the 8% development compared with same weight of the flat web girder. This slight increase was due to using extremely thin web thickness of about 0.70 mm. The steel plate thickness has a great effect on the web shear strength. However, reducing the dimension web corrugations can contribute to enhancing the buckling resistance due to increasing the moment of inertia of the Y axis (I_y).

While the decrease in the ultimate load of $HW60L_2$ and $HW60L_3$ obviously appeared as illustrated in Figures 3E and 3F. This decrease was a result of increasing the spacing between the intermediate stiffeners to the web depth ratio. When the shear span to depth ratio increases, the tension field action that developed between inside web panel also decreases. The tension field action can resist the diagonal tension.

Figures 4A, 4B and 4C show the elastic buckling load values: 102 kN, 106 kN and 84 kN, while the ultimate loads: 126 kN, 118 kN and 98 kN and the linear vertical displacement of midspan; 2.00 mm, 1.90 mm and 4.60 mm for $HW80L_1$, $HW80L_2$ and $HW60L_3$, respectively. Figure 4 shows the difference in load carrying capacity when the aspect ratio increased from 1%, 2% and 3%. The ultimate load decreased when the aspect ratio increased. In the failure mode, intermediate buckling failure was noticed at all these categories of honeycomb steel plate web specimens.

As Figures 4D, 4E and 4F state, three tested specimens of honeycomb web steel plate I-girder specimens: $HW100L_1$, $HW100L_2$ and $HW100L_3$ with a/d equal to 1%, 2% and 3%. The thickness of the steel plate was 0.70 mm, which it is a constant for all honeycomb web pattern. The test results of the load carrying capacity of honeycomb steel plate web with a/d equal to 1.0% $HW100L_1$ was 93 kN while the other honeycomb specimens with corresponding aspect ratio values; 2% and 3% were (80 kN and 72 kN) for $HW100L_2$ and $HW100L_3$ specimens, respectively. Noticeably, these specimens recorded less value in the shear strength and midspan deflection compared with other specimens of honeycomb steel web with fold dimensions

equal to 60 mm and 80 mm. The maximum deflections were 1.10 mm, 2.10 mm and 3.10 mm. What is more, the local buckling and intermediate shear web buckling failure was obtained.

For the honeycomb web steel plate girders with *a*/*d* equal to 3% or with 1,800 mm length, the maximum percentage decreases in the shear strength of honeycomb web value of 31.4% from test results of the $HW100L_3$. While the maximum percentage decreases in the midspan vertical deflection value of 62% from the test results of the honeycomb web $HW60L_3$. As noticed, dimension folds, plate thickness of honeycomb web, and aspect ratio have an important influence on the ultimate load and deflection.

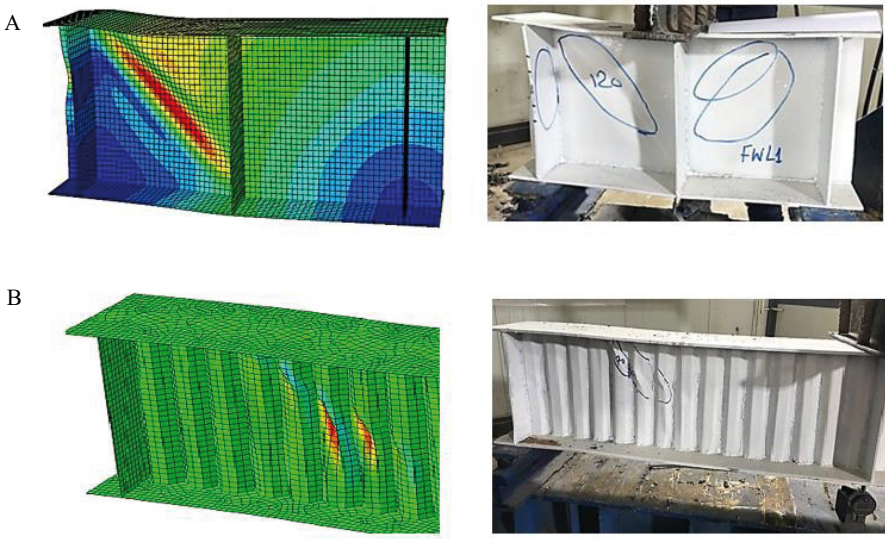

FIGURE 5. Comparison of shear buckling failure between Shaffaf and Ammash (2022) experimental study and present finite element model buckling for girders with flat and honeycomb steel plate web: A – global buckling mode of flat web girder with 600 mm length FWL_1; B – intermediate buckling of honeycomb web girder with 60 mm thick and 1,800 mm length $HW60L_3$

Source: own work adopted from Shaffaf and Ammash (2022).

Slenderness ratio of honeycomb web and aspect ratio

This paper uses the numerical analysis to investigate the effect of the web slenderness ratio on the shear buckling strength. Fifteen I-section specimens of simply supported steel plate web girders were manufactured using the honeycomb corrugated steel plate web in the FE, Abaqus/CAE software. These specimens were sepa-

rated into five distinct groups. Each has a unique honeycomb corrugated steel web dimension of 20 mm, 40 mm, 60 mm, 80 mm and 100 mm, and each group consists of three specimens with lengths of 600 mm, 1,200 mm and 1,800 mm, or aspect ratios of 1%, 2% and 3%.

Figure 6 depicts the relationship between the ultimate strength and slenderness ratio of the web (b/t_w) of 600 mm long honeycomb web specimens (HWL_1). Figure 6 demonstrates that the honeycomb web with a 20 mm fold dimension and a b/t_w of 29% had the highest load capacity value compared to other fold dimensions (40 mm, 60 mm, 80 mm and 100 mm). Figure 7 depicts the shear strength change versus slenderness ratio of 1,200 mm long honeycomb web girders (HWL_2). As shown in Figure 7, as the ratio of web slenderness decreases, the shear strength against shear web buckling failure increases. Hence, in the structural web design of steel plate girders in steel constructions, increasing the web corrugation will be ineffective and may increase cost, mass, and shear strength without providing any benefit.

In addition, Figure 8 illustrates the honeycomb web girder with 1,800 mm long HWL_3 and its negative relationship with load carrying capacity or shear strength and b/t_w. As the ratio of web slenderness increases, shear strength decreases. So, it can be concluded that, for a constant steel plate thickness, when the corrugated dimensions of the web are reduced, the steel plate will behave like a thick plate that resists shear stress with a high yield strength, as opposed to a thin plate that resists shear stress with a lower yield strength. The shear span also influences the shear

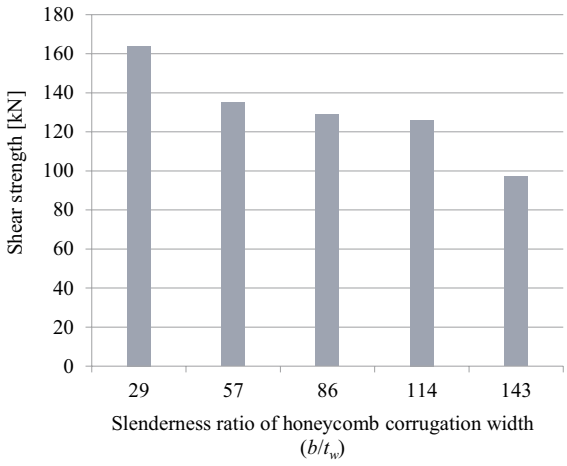

FIGURE 6. Shear strength verse slenderness ratio of honeycomb web cross-section for the HWL_1 specimen with various corrugation dimension: 60 mm, 80 mm and 100 mm and with 600 mm length

Source: Ammash and Shaffaf (2022).

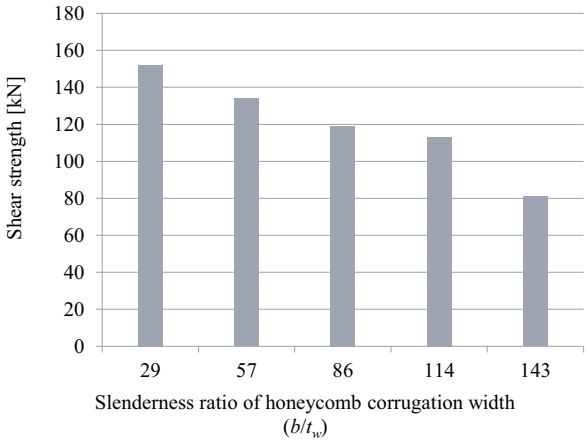

FIGURE 7. Shear strength verse slenderness ratio of honeycomb web cross-section for the HWL_2 specimen various corrugation dimension: 60 mm, 80 mm and 100 mm and with 1,200 mm length

Source: Ammash and Shaffaf (2023).

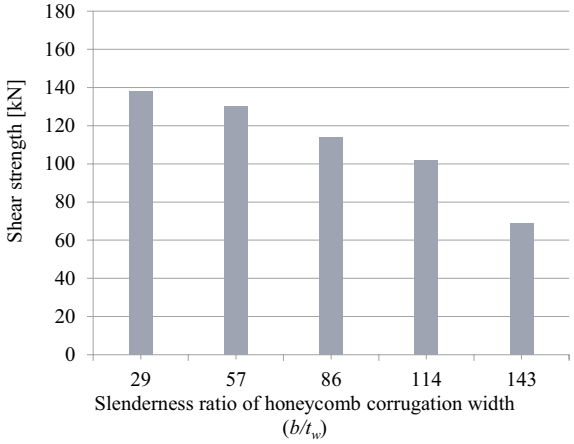

FIGURE 8. Shear strength verse slenderness ratio of honeycomb web cross-section for HWL_3 specimen various corrugation dimension: 60 mm, 80 mm and 100 mm and with 1,800 mm length

Source: Ammash and Shaffaf (2022).

strength-to-depth or *a*/*d*. The shear buckling strength decreases as the distance between the intermediate stiffeners and the effective depth increases (Abdullah, Muhaisin & Ammash, 2022). In this numerical analysis, Figure 9 depicts the relationships between the shear strength results of twelve honeycomb and plain web FE girder models and *a*/*d* values.

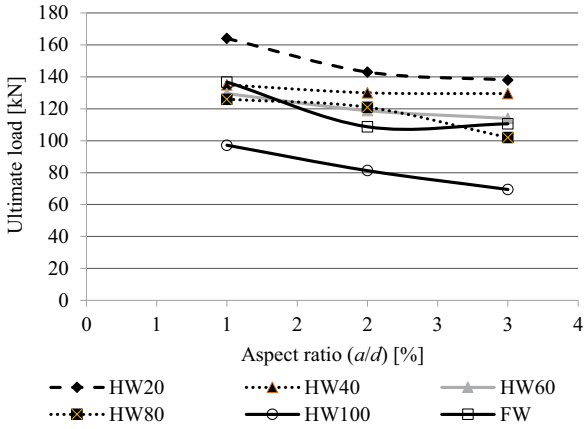

FIGURE 9. Ultimate load verse shear span to depth ratio (a/d) for all plate girder specimens flat web and honeycomb web

Source: Ammash and Shaffaf (2022).

Effect of honeycomb steel plate web thickness

Regarding the effect of thickness on the buckling strength, shear buckling in the steel honeycomb web is directly proportional to the thickness. The positive relationship between the increased steel web thickness and shear buckling strength holds true for flat and curved webs. Under a concentrated load, Figure 10 depicts the load--carrying capacity of the flat and honeycomb corrugations plate web with a thickness ranging from 1 to 4 mm.

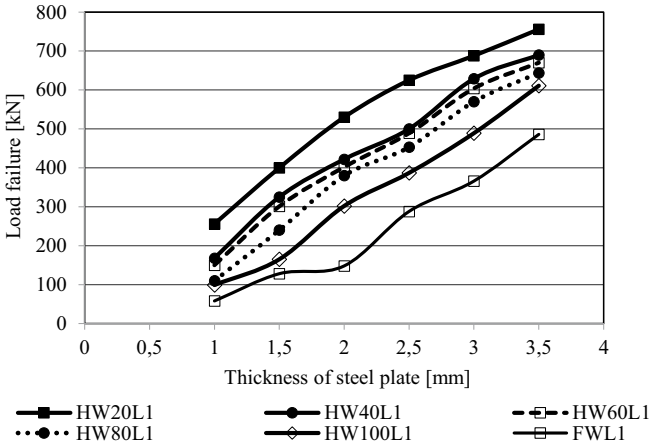

FIGURE 10. Variation in the shear web buckling resistance of the flat web and the honeycomb web specimens which have 600 mm length verse the thickness of steel plate (t_w)

Source: Ammash and Shaffaf (2022).

Types of shear failure

When a simply supported girder is subjected to a concentrated load, a maximum vertical shear force will develop at each support and be opposed by the web of both panels. Due to the intermediate stiffeners at each simply supported edge and under concentrated load, tension field action carried by the width of the web subpanels at a 45° angle against the shear web buckling failure diagonal will withstand the applied shear stress. Increasing the inside spacing between intermediate stiffeners can effectively reduce the shear buckling strength. Consequently, the web subpanel will fail gradually under local, global, or middle shear buckling. Theoretically, the inelastic shear buckling failure is controlled if the web is designed with thin dimensions, wide corrugation width, and compact flange. Failure is primarily determined by web shear buckling or pure shear (Fig. 11A). Steel plate with a small corrugation dimension (20 mm) while maintaining other parameters (flanges thicknesses, width, web depth, and thickness) has improved critical shear strength (τ_{cr}) to the yield strength (τ_y) against the slenderness ratio (b/t_w) and exhibits an elastic behavior that significantly enhances the web shear strength compared to other corrugation dimensions (40 mm, 60 mm, 80 mm, and 100 mm). Shear stress includes a component for flexural failure. It is known as flexural shear, as shown in Figure 11B.

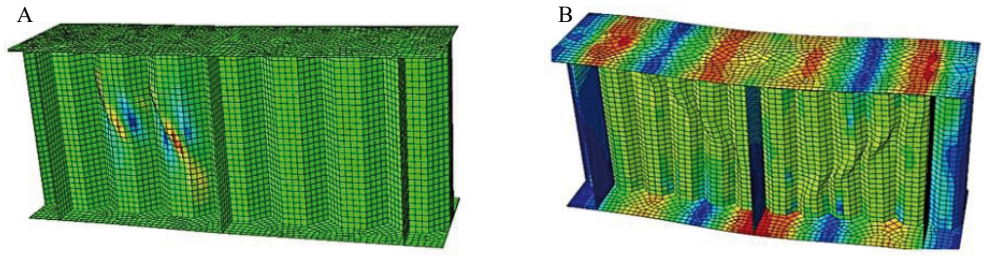

FIGURE 11. The failure of the honeycomb steel plate web girder: A – shear buckling failure of the girder with 60 mm corrugation dimension and 600 mm length; B – flexural-shear failure of the girder with 20 mm corrugation dimension and 600 mm length

Source: Ammash and Shaffaf (2022).

Conclusions

This paper numerically investigates the shear behavior and failure modes, flexural failure and buckling web shear failure of the specimen flat web and the honeycomb web patterns. This innovative honeycomb web (corrugated web) system

typically has high shear strength and less midspan vertical displacement compared with fat web mode.

There are two numerical analyses carried out in the present paper. The first step is the elastic or the linear shear buckling. The second step is the non-linear or inelastic buckling which was adopted to simulate the post shear buckling behavior of all plate girder specimens under the effect of one concentrated load applied at midspan of girders. From the numerical and experimental comparison of the present study, it is possible to conclude the following:

- The shear buckling resistance of the honeycomb web plate girder was significantly higher than that of the flat web, particularly at a thickness of 60 mm.
- The dimensions of the corrugated honeycomb web can adversely affect the critical shear stress.
- Girders with 20 mm thick honeycomb steel plates provided greater ultimate load and less midspan deflection than girders with larger corrugation web dimensions.
- Due to the increase in the web slenderness ratio, shear strength decreased as honeycomb web dimensions increased.
- The load-carrying capacity of the steel web can be enhanced by increasing the thickness of the steel plate.
- The ultimate load increased from 8 to 30% when the width of the corrugated honeycomb web was reduced from 60 to 20 mm.
- The shear web strength of honeycomb web increased from 60 to 450% when steel plate thickness was increased from 1 to 4 mm.
- According to the Euler equation, as the honeycomb web's moment of inertia increases, the corrugated web's critical buckling load increases. Thus, when the corrugation dimension decreases, the moment of inertia of the X axis (I_x) increases, and then the shear strength of the corrugated steel web increases.
- Shear strength is negatively affected by the slenderness ratio of the corrugation dimension.

References

Abbas, M., Ibrahim, S. M. & Korashy, M. M. (2019). Lateral torsional buckling of partial corrugated web steel beams. *International Journal of Scientific & Engineering Research*, *10* (6), 602–609.

Abdullah, M. D., Muhaisin, M. H. & Ammash, H. K. (2022). Effect of shear span-to-depth ratio on behavior of sandwich core steel girder with corrugated web. *Scientific Review Engineering and Environmental Sciences*, *31* (2), 79–87.

American Institute of Steel Construction [AISC] (2016). *Code of standard practice for steel buildings and bridges* (ANSI/AISC 303-16). Chicago: American Institute of Steel Construction.

Ammash, H. K. & Al-Bader, M. A. (2021). Shear behaviour of steel girder with web corrugated core sandwich panels. *IOP Conference Series: Materials Science and Engineering*, *1090* (1), 2017.

Ammash, H. K. & Dashi, R. H. (2022). *Effect of shear span on behavior of steel girder with corrugated web* [unpublished].

Ammash, H. K. & Kadhim, A. W. (2022). Shear behaviour of filled concrete core sandwich steel web girder. *Journal of Physics: Conference Series*, *1895* (1), 12062.

De'nan, F. & Hashim, N. S. (2013). Experimental study on bending behaviour of triangular web profile steel beam section. *International Journal of Research in Engineering and Technology*, *2* (10), 384–390.

Hassanein, S. A., Salem, E. S. & Mohmoud, A. M. (2018). Post-buckling shear behavior of corrugated steel web girders. *Al-Azhar University Civil Engineering Research Magazine (CERM)*, *40* (2), 288–305.

Leblouba, M., Barakat, S. & Al-Saadon, Z. (2018). Shear behavior of corrugated web panels and sensitivity analysis. *Journal of Constructional Steel Research*, *151*, 94–107.

Nie, J. G., Zhu, L., Tao, M. X. & Tang, L. (2013). Shear strength of trapezoidal corrugated steel webs. *Journal of Constructional Steel Research*, *85*, 105–115.

Pasternak, H. & Kubieniec, G. (2010). Plate girders with corrugated webs. *Journal of Civil Engineering and Management*, *16* (2), 166–171.

Shaffaf, N. N. & Ammash, H. K. (2023). *Experimental study of steel plate girder with innovative shape of web under concentrated load.* Retrieved from: https://assets.researchsquare.com/files/rs-2583040/v1/c4b5f9027b96edb87aefa9de.pdf?c=1676435938 [accessed: 20.01.2023].

Summary

Behavior study of the steel plate girder with a cellular honeycomb web. Based on the experimental test results of the authors, this investigation is concerned with the finite element analysis to examine and compare the load values and failure modes of the authors' results. This research was conducted using the Abaqus software. The experimental work included the fabrication of twelve plate girders with honeycomb and flat web plate corrugation patterns, which were then tested under a single concentrated load at the midspan. According to the corrugation dimension or outer honeycomb web thickness, the honeycomb steel plate web girder is divided into three groups (60 mm, 80 mm and 100 mm). The specimens also involved plate girders with a flat web. The specimens were created with three lengths (600 mm, 1,200 mm and 1,800 mm). The Abaqus software was used in finite element models to simulate the concentrated load. The numerical results demonstrated that the 60 mm thick honeycomb web provides a greater load-bearing capacity and shear strength than other girders. The 20 mm honeycomb corrugation on the steel plate girder indicates the increased and improved shear

resistance. The conclusion was that as the width of the corrugation increased, so did the steel web's ultimate load and shear strength, resulting in a positive relationship between the critical shear buckling load of the web and the moment of inertia at the strong axis. When the dimension of the corrugation increases, the moment of inertia of the Y axis (I_y) decreases; thus, the plate girder will fail with a less critical buckling load (P_{cr}). Also, it can be concluded that as the steel plate thickness of the honeycomb web increases, the shear resistance increases as well. However, the spacing between the intermediate stiffener or the horizontal spacing of the web panel can enhance the shear resistance of honeycomb web girder if it was decreased due to increasing the action of tension field force that resists the diagonal tension developed at the web panel by the applied midspan concentrated force.

Scientific Review Engineering and Environmental Sciences (2023), 32 (2), 117–134

Sci. Rev. Eng. Env. Sci. (2023), 32 (2) https://srees.sggw.edu.pl

ISSN 1732-9353 (suspended) eISSN 2543-7496 DOI 10.22630/srees.4768

Received: 31.01.2023
Accepted: 14.04.2023

Aya M.E. AHMED[1] https://orcid.org/0000-0002-8636-4598
Osman HAMDY[2] https://orcid.org/0000-0002-4397-9015
Youssef L.Z. SAAD[3] https://orcid.org/0000-0003-0182-0329
Seleem S.E. AHMAD[4]✉ https://orcid.org/0000-0001-9894-0209

[1, 2]Zagazig Higher Institute of Engineering & Technology, Department of Civil Engineering, Zagazig, Egypt
[3, 4]Zagazig University, Faculty of Engineering, Zagazig, Egypt

Residual strength and toughness after impact loading for RC slabs strengthened with different layers of geogrid

Keywords: impact load, geogrid, RC slab, residual strength, static flexural load, toughness, toughness index

Introduction

Concrete is very brittle under tensile stresses and impact loads, so reinforcing bars or pre-stressing steel are added. Augmented concrete slabs are the structural elements extensively used in building structures. Basic concrete components require materials such as glass, carbon, steel fibers and Geosynthetic composites, including geogrid and geocells, to improve their strength, stiffness, flexural resistance, as well as impact and abrasion resistance (Vijay, Raj & Babu, 2021). Geogrids are polymers, such as polyester, polypropylene, and polyethylene, and consist of regular rectangular, square or triangular apertures (Dong, Han & Bai, 2011). Three main types of geogrids are

✉seleemahmad62@yahoo.com

used for reinforcement: uniaxial, biaxial, and triaxial (El Meski & Chehab, 2014). Many advantages lead to the use of geogrid, such as high resistance to attack by chlorides and sulfates, corrosion, being very light in terms of weight, relatively cheap, easy to transport, cut and use, and providing shear strength and high tensile resistance (Chidambaram & Agarwal, 2015; Yousif, Mahmoud, Abd Hacheem & Rasheed, 2021). Therefore, geogrid can replace tension steel in reinforced concrete elements (Nishanthi et al., 2021). Ibrahim, Turk and Fares (2020) scrutinize the effect of slab thickness on the mechanical behavior of high-strength concrete slabs containing geogrid as reinforcement layers. It was observed that the increase in the slab thickness from 50 to 80 mm led to an increase in the ultimate loads and the absorbed energy for the plain concrete control slab. Increasing slab thickness increased the slabs' ultimate loads for specimens reinforced using uniaxial, biaxial, and triaxial geogrid by about 216.3%, 100%, and 167.3%, respectively. Still, it decreased the absorbed energy for specimens reinforced using the biaxial and triaxial geogrid by about 22.5% and 16.75%, respectively. The study by Fares, Hassan and Arab (2020) considered the flexural behavior of high-strength concrete slabs reinforced with the treated and untreated geogrid. They found that using two layers of uniaxial and triaxial geogrid as reinforcement for ordinary concrete slabs gives lower results than biaxial geogrid. The maximum loading capacity of flexural behavior for the tested slab treated chemically increased by about 8.5% for one geogrid and 13% for two geogrids compared to the untreated samples. Moreover, the addition of the geogrid reduced the maximum flexural loading capacity, but substantially increased the flexibility of the slab. Geogrid may be an effective alternative material for concrete confining. Chidambaram and Agarwal (2014) studied the effect of geogrid confining on the mechanical properties of concrete samples reinforced with steel fiber under flexural and compression. They found that the geo-network power and number of layers played an essential role in enhancing deformation and crack propagation. Meng, Jiang and Liu (2021) studied previous concrete strength, permeability, and flexural behavior with various coarse aggregate sizes, geogrid positions and layers by experimentation. They found that geogrids improved the concrete beam's flexural strength, deformability and energy absorption capability. The optimum flexural behavior of the concrete beam was obtained by putting the geogrid at both one-third and two-thirds of the concrete heights. The geogrid was put in a suitable position in the previous concrete. Besides, the large size (10–15 mm) aggregates resulted in remarkable post-cracking performance, while the small size (5–10 mm) aggregates provided high flexural strength for the concrete beam. The study performed by Mohammed and Najim (2020) investigated the mechanical strength, flexural behavior and fracture energy by using aggregates of a recycled concrete (RCA) to make self-compacting concrete (RASCC).

It was concluded that the mechanical strength, including flexural, splitting, and compressive strengths was decreased by adding RCA with slight decline in the modulus of elasticity. However, this reduction of the required mechanical strength did not affect its use as structural concrete. Vijay, Kumar, Vandhiyan, Mahender and Tharani (2020) experimented with the impact behavior of the geogrid-reinforced concrete slabs. The experimental results showed that the RC slab samples reinforced with geogrid and steel had a superior performance by refining the resistance to the impacted shear stress, and this helped spread the tensile stress from the impact loading to a large area, thus evading the accumulation stress at a specific loading point. These specimens can withstand a higher number of impact loading blows, which affects the performance of impact energy absorption and impact ductility index. Muda et al. (2013) experimentally studied the behavior of the lightweight oil palm shells (OPS) concrete slab reinforced with geogrid of 30 × 30 cm size with 2 cm, 3 cm, and 4 cm thick cast with various geogrid orientations and boundary conditions exposed to low impact projectile test. The results showed that using geogrid amplified the impact resistance and had good cracking resistance compared to the samples without geogrid. The orientation of the geogrid in the OPS concrete slab has little significance in the crack resistance. A worthy linear relationship exists between the ultimate and the first crack resistance against the thickness of the slab. Al Qadi, Al-Kadi, and Al-Zaidyeen (2015) studied the impact resistance of oil-palm shells (OPS) experimentally on lightweight concrete slabs reinforced with a geogrid. Adding a geogrid layer in the sample raised the cracking resistance, both for the first crack and the ultimate failure. Geogrid 80/80, with a characteristic short-term tensile strength of 80 $kN \cdot m^{-1}$ in both directions, had a better impact on cracking resistance. Yahaghi, Muda and Beddu (2016) studied the impact resistance of the oil palm shells (OPS) concrete reinforced with the polypropylene (PP) fiber. There was a strong linear relationship between the volume fraction of the PP fiber, impact resistance and cracking resistance ratio. This relation was unbeatable by any change in the thickness from 20 to 40 mm. Although the thickness increment enhanced the impact resistance meaningfully, the effect was more obvious for ultimate failure crack resistance than for first crack resistance. Ahmad, Seleem, Badaway and El Safoury (2016) studied the behavior of high-performance concrete slabs supported by steel and polypropylene fiber under flexural impact loading. The used specimen was slab of dimensions 500 × 500 × 60 mm reinforced with 10 mm diameter steel bars in two directions. They found that there were fully damaged ones that took place among the specimens under impact from height of 270 cm. While partial damage had happened for impacted specimens from height 80 cm and can be tested under central flexural test the residual strength was different according to fiber type and content. Ganesh, Muthukannan, Dhivya, Sangeetha and Daffodile (2020)

studied the mechanical properties of hybrid fiber-reinforced geopolymer concrete specimens. The polypropylene fibers and the glass were added in several quantities. They found that using 1% polypropylene fiber produced maximum toughness index values. They used 1% glass fiber to produce maximum stiffness under yield and ultimate strain conditions. Ye, Liu, Zhang, Wang and Peng (2020) carried out an experiment to study the effect of high-strength steel fiber lightweight aggregate concrete (HSLAC) on the mechanical properties together with the toughness index. Three types of steel fibers were studied, and these were: being micro (M), end-hooked (H), and corrugated (C), and they were the proportions of the studied fiber content 0.5–2.0%. The M steel fibers reinforcement had the best results on the mechanical properties. It had the best toughness value with the same fiber content. Furthermore, the toughening effect of H and C steel fibers could only reach 66% and 50% of M steel fibers, respectively. Su and Fan (2021) studied the flexural toughness of steel––polyvinyl alcohol hybrid fiber reinforced. The results proved that the concurrent integration of the steel fiber and polyvinyl alcohol fiber critically improved the concrete's maximum load and the toughness index throughout bending failure, while fiber concrete had a noticeable strain-hardening phenomenon. When polyvinyl alcohol fiber volume content is 0.75% and steel fiber volume content is 1.25%, hybrid fiber concrete shows a good positive hybrid effect, which is perfect for advancing the bending performance. Ou, Tsai, Liu and Chang (2012) studied the properties of the compressive stress–strain behavior of steel fiber-reinforced concrete (SFRC) with a high reinforcing index. They found that the toughness of concrete increased with a fiber volume fraction equal to 2% when using steel fibers. Also, longer fibers increased the toughness of concrete more than the short ones. In this work, an experimental study carried out for three groups of reinforced concrete slabs of different thicknesses supported by biaxial geogrid layers at different distances, and each group contained six slabs. In each group, ultimate load, deflections, toughness, and toughness index were measured while testing specimens.

Experimental program

Table 1 shows the different configurations of the geogrid reinforcement used of the RC slabs studied in the current work. Each RC slab was reinforced by 5Ø10/m as lower steel reinforcement in both directions. The dimensions of the slabs were 50 × 50 cm, where three different thicknesses considered 12 cm, 15 cm and 18 cm. Moreover, different locations from the upper face of concrete were considered in the current study.

TABLE 1. Configurations of tested RC slabs

Slab thickness (*ts*) [cm]	Geogrid configuration	Test condition	Location from upper face (*CC*) [cm]
12	without	static, control	–
	one layer	static, control	3
	one layer	impact	3
	two layers	impact	3
	one layer	impact	5
	two layers	impact	5
	two layers	impact	3 and 6
15	without	static, control	–
	one layer	static, control	3
	one layer	impact, static	3
	two layers	impact, static	3
	one layer	impact, static	5
	two layers	impact, static	5
	two layers	impact, static	3 and 7.5
18	without	static, control	–
	one layer	static, control	3
	one layer	impact, static	3
	two layers	impact, static	3
	one layer	impact, static	5
	two layers	impact, static	5
	two layers	impact, static	3 and 9

Source: own work.

Each slab sample was casted in timber mold painted with oil with inner dimensions of 50 × 50 cm with 5Ø10/m as lower steel reinforcement in both directions. The mold sides were in timber with a thickness of 2.5 cm, whereas the bottom timber side was 0.5 cm, the geogrid reinforcement layers added at their position in accordance with each case individually throughout the casting process.

Tests preparation

Material

Material properties of the concrete used, steel reinforcement, and geogrid reinforcement were precisely measured before the experiment. The mix design of the used concrete is shown in Table 2, together with the average compressive strength of tested three standard cubes with dimensions of 15 × 15 × 15 cm.

Ahmed, A. M. E., Hamdy, O., Saad, Y. L. Z., Ahmad, S. S. E. (2023). Residual strength and toughness after impact loading for RC slabs strengthened with different layers of geogrid. *Sci. Rev. Eng. Env. Sci.*, *32* (2), 117–134. DOI 10.22630/srees.4768

TABLE 2. Concrete trail mix proportions of concrete mixes

Concrete ingredient	Unit	Dosage value
Cement	$kg \cdot m^{-3}$	300
Water	$l \cdot m^{-3}$	160
Gravel	$kg \cdot m^{-3}$	1 120
Sand	$kg \cdot m^{-3}$	720
The average result of three cubes of compressive strength	$kg \cdot cm^{-2}$	252

Source: own work.

TABLE 3. Properties of biaxial geogrid

Index properties	Unit	Value
Aperture dimensions from center to center	cm	3.7
Rib thickness	cm	0.2
Tensile strength	$kN \cdot m^{-2}$	30
Elongation	%	11
Weight	$g \cdot m^{-2}$	320
Roll width	cm	50
Roll length	cm	400

Source: own work.

A tension test, according to the Egyptian ES 262-2/2015 standard (Egyptian Organization for Standardization & Quality [EOS], 2015), and ISO 6935-2/2007 standard (International Organization for Standardization [ISO], 2007), were done for the reinforcement steel bars. Three samples were tested. The average results for reinforcement were 411 MPa as yield strength, 633 MPa as tensile strength and 15% as maximum elongation. Moreover, the geometric and strength properties of the geogrid reinforcement used, as recommended by the manufacturer, are given in Table 3.

Casting and curing

Mixing the concrete components was done by a mechanical mixer, then casted and placed in layers inside the mold. The compaction for the unreinforced slab by geogrid, control specimen, was done completely by using a mechanical vibrating table. On the other hand, for slabs reinforced by geogrid layers, we used a combination of a vibrating table and manual compaction so that we kept the geogrid layer at a distance during fixing, as shown in Figure 1. After that, the surface was finished and flattened.

Plastic sheets were used to cover the slab samples and cubes for 24 h, as shown in Figure 2, and all samples were unmolded and labeled. The cubes were submerged in clean water for 28 days as a curing process before performing the compression test as shown in Figure 3. The average result of the three cubes of compressive strength is 25.2 MPa.

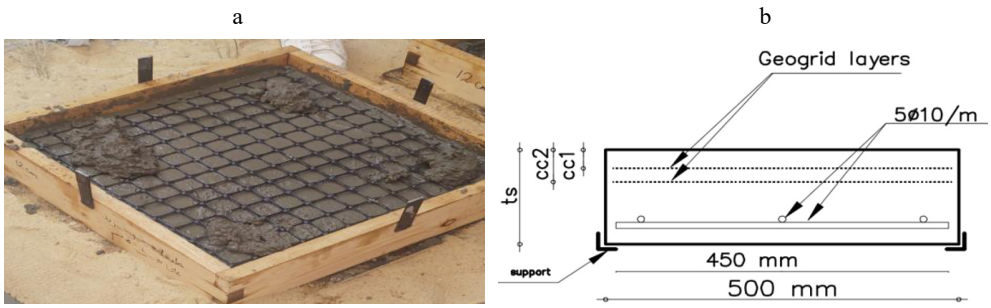

FIGURE 1. Placing a geogrid layer through the casting process (a) and schematic figure for tested specimens (b)

Source: own work.

FIGURE 2. Labeled RC samples after unmolding

Source: own work.

FIGURE 3. Compression test

Source: own work.

Tests

Impact test

A special impact testing machine was designed and fabricated at the laboratories in the Faculty of Engineering, Zagazig University by Seleem, Mohamed, Aml and Ashraf and Safoury in 2016, considering the drop weight impact test mechanism. The impact-testing machine can perform flexural impact tests for 50 × 50 cm slabs with different thicknesses. The components of the impact-testing machine are detailed in Figure 4b.

The machine steel frame was fabricated from steel sections considering the mechanism of dropping weight to act as rails to ensure the direction of the drop is in the specimen's center. The drop weight weighs 70 kg. The dropping weight is elevated

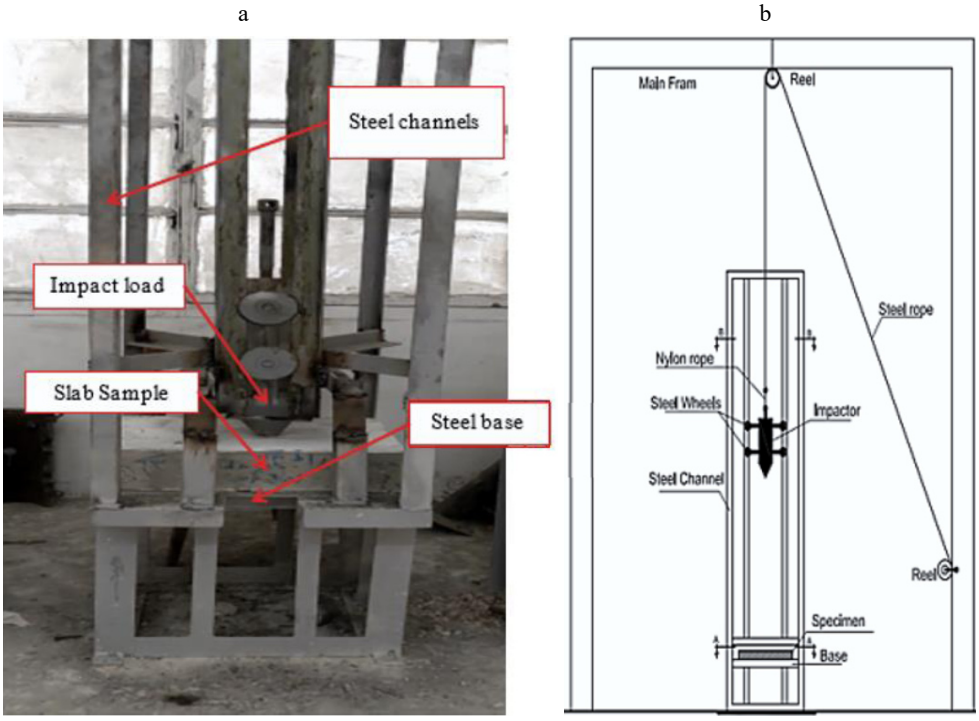

FIGURE 4. Set up of the impact test (a); impact testing machine components (b)
Source: own work.

up to the specified height (150 cm), using a steel cable hung on a steel wheel at the top of the frame, as shown in Figure 4b. The drop weight is changed by moving the wheel arm to pull the steel cable to the specified height. After dropping the impactor, it released from the specimen and was fixed for the next drop; the number of drops for each specimen is five.

Static and residual load test

After subjecting the slabs to the impact load (Fig. 4), the residual strength is determined by loading the slabs with the static load (Fig. 5). As residual strength refers to the ability of a material or structure to resist further damage and maintain its load--carrying capacity even after experiencing some level of damage due to pre-loading. The residual load is here determined by exposing the samples to an impact test under a load of 70 kg, dropped from a height of 150 cm, and subjected to five blows, then exposing the samples again to the flexural test, and then the load is recorded (residual load).

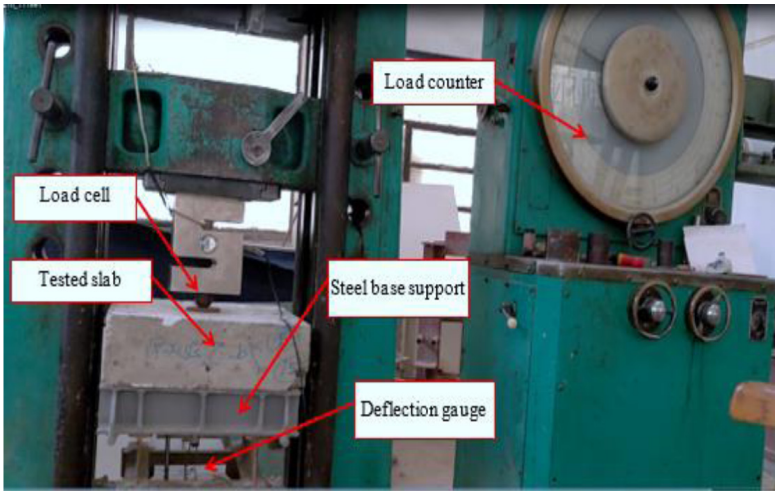

FIGURE 5. Set up of the static test
Source: own work.

The load and deflection are recorded through different stages of the loading process during the slab loading centrally. The static applied load of the test machine was concentrated on the center point using a hard steel ball with a 30 mm diameter on the top face of the specimen, as shown in Figure 4a. White water paint was used to paint the bottom face of the slab; this face was divided into squares 100 × 100 mm to notice the crack pattern during and after the static loading test.

Results and discussion

Control specimens

Six control samples with/without geogrids are subjected directly to a static load test without any impact for comparison. The load and deflection relation are recorded through a static loading process for all specimens. Figures 6–8 show the load–deflection curves for control 12 cm, 15 cm, and 18 cm control specimens with/without geogrid.

As shown in Figures 6–8, the specimens with a geogrid showed more loading capacity and maximum deflection than slabs without geogrids. Where for 12 cm thick slabs, the maximum load was enhanced from 95 kN to reach 103 kN and the maximum deflection increased from 2.714 mm to 5.486 mm. For 15 cm thick slabs, the maximum load was enhanced from 122 kN to reach 150.12 kN, and the maximum

Ahmed, A. M. E., Hamdy, O., Saad, Y. L. Z., Ahmad, S. S. E. (2023). Residual strength and toughness after impact loading for RC slabs strengthened with different layers of geogrid. *Sci. Rev. Eng. Env. Sci.*, *32* (2), 117–134. DOI 10.22630/srees.4768

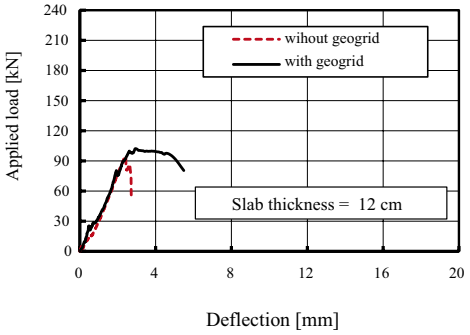

FIGURE 6. Load against deflection for control slab with thickness of 12 cm

Source: own work.

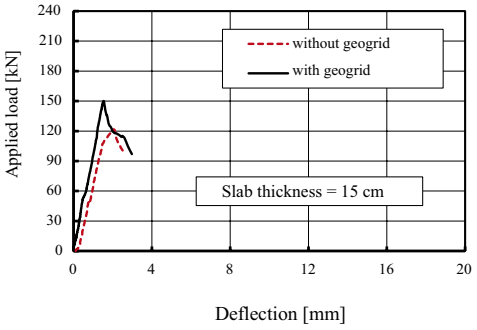

FIGURE 7. Load against deflection for control slab with thickness of 15 cm

Source: own work.

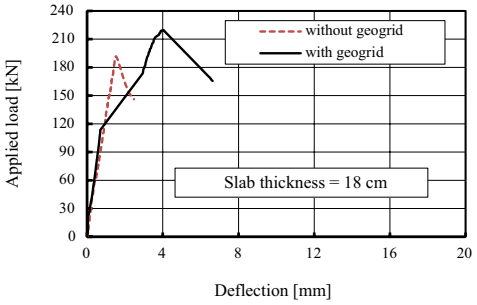

FIGURE 8. Load against deflection for control slab with thickness of 18 cm

Source: own work.

deflection was increased from 2.53 mm to reach 2.983 mm. Also, for 18 cm thick slabs, the maximum load was enhanced from 192 kN to reach 220 kN, and the maximum deflection was increased from 2.478 mm to reach. 6.633 mm. These results confirmed the positive effect of geogrid reinforcement on the slab strength and toughness. Moreover, the data indicated that the slab toughness enhancement was due to the existence of a geogrid with the increasing slab thickness.

Failure mode of control specimens

Figures 9–12 illustrate a comparison of the failure modes and crack pattern for the tested control specimens with geogrid and without geogrid under static loads only. The Figures show that a geogrid effectively affects the crack pattern and distribution, especially for thickness of 12 cm and 18 cm.

By comparing the crack behavior for all specimens, it is clear that the geogrid affects the number of cracks, as samples containing the geogrid reduce the number and distribution of cracks and mitigate their severity. It is clear that the geogrid samples have an optimal fracture pattern and distribution due to good resistance to flexural load and high values of ultimate loads than samples without geogrid, which comply with the previous load deflection figures.

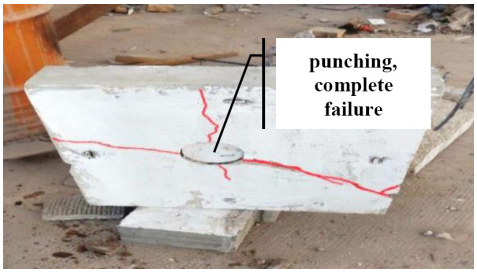

FIGURE 9. Failure mode of control specimen t12 without geogrid under static loads only

Source: own work.

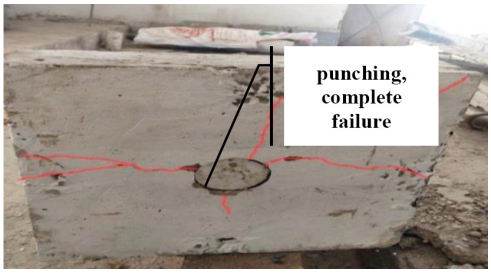

FIGURE 10. Failure mode of control specimen t12 with one-layer geogrid under static loads only

Source: own work.

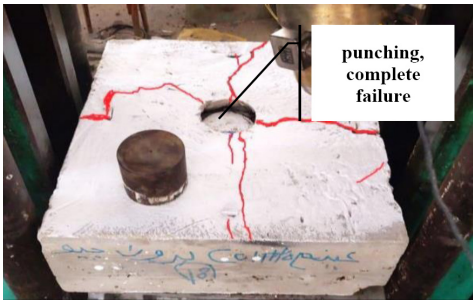

FIGURE 11. Failure mode of control specimen t18 without geogrid under static loads only

Source: own work.

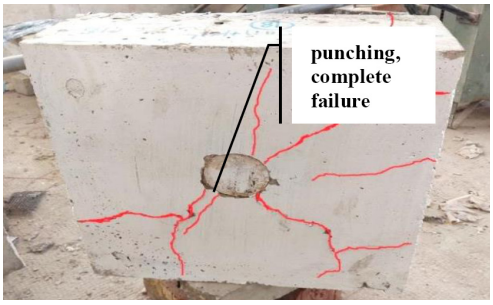

FIGURE 12. Failure mode of control specimen t18 with one-layer geogrid under static loads only

Source: own work.

Impact test results

The test was conducted on 15 slabs (50 × 50 cm) of different thicknesses (12 cm, 15 cm and 18 cm). All samples were tested under a load of 70 kg, dropped from a height of 150 cm, and subjected to five blows. The slab samples with a thickness of 12 cm got completely damaged, as shown in Figures 13 and 14, so they were not tested by the static load test, i.e., their residual strength equals.

Table 4 shows the number of drops required for full damage for 12 cm slabs. The results showed that slabs reinforced with one layer of geogrid are stronger than slabs reinforced with two layers for 12 cm.

The slabs with a thickness of 15 and 18 cm did not have complete damage, so a static flexural test was performed for them. Figures 13–16 show some details of failure for slabs after being subjected to impact load with thicknesses of 12 cm, 15 cm and 18 cm, respectively.

Ahmed, A. M. E., Hamdy, O., Saad, Y. L. Z., Ahmad, S. S. E. (2023). Residual strength and toughness after impact loading for RC slabs strengthened with different layers of geogrid. *Sci. Rev. Eng. Env. Sci.*, *32* (2), 117–134. DOI 10.22630/srees.4768

FIGURE 13. Failure pattern of 12 cm slabs with two layers of geogrid at 3 cm after impact loading
Source: own work.

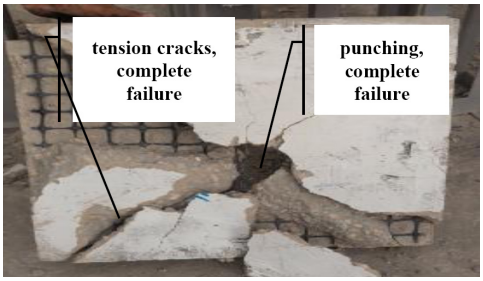

FIGURE 14. Failure pattern of 12 cm slabs with one layer of geogrid at 5 cm after impact loading
Source: own work.

FIGURE 15. Failure pattern of 18 cm slabs with two layers of geogrid at 3 cm after impact loading
Source: own work.

FIGURE 16. Failure pattern of 15 cm slabs with two layers of geogrid at 5 cm after impact loading
Source: own work.

TABLE 4. Number of drops for full damage for 12 cm slabs

Sample case	Drops for full damage
t12 one layer of 3 cm	5
t12 one layer of 5 cm	5
t12 two layers of 3 cm	4
t12 two layers of 5 cm	4
t12 two layers of 3 and 6 cm	4

Source: own work.

Residual static test results

The results of the residual static tests are recorded for each slab in the form of a relation between static loads with its corresponding deflection. As mentioned before, the load is concentrated in each slab's center, where the deflection is recorded for the same point of the slab center. Figures 17 and 18 show the residual load–deflection curves of each sample under static load, whereas, as shown from the graphs, the load–deflection relation proceeds a positive linear relation at the first stage until reaching the maximum load, followed by a nonlinear negative relation till complete failure.

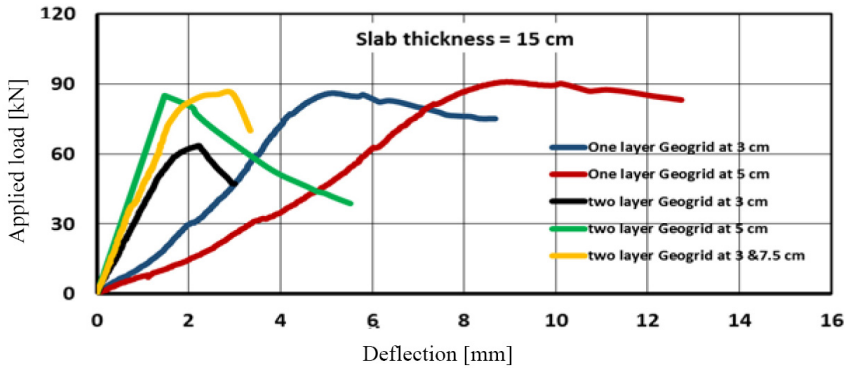

FIGURE 17. Residual load against deflection for slab with thickness of 15 cm with geogrid
Source: own work.

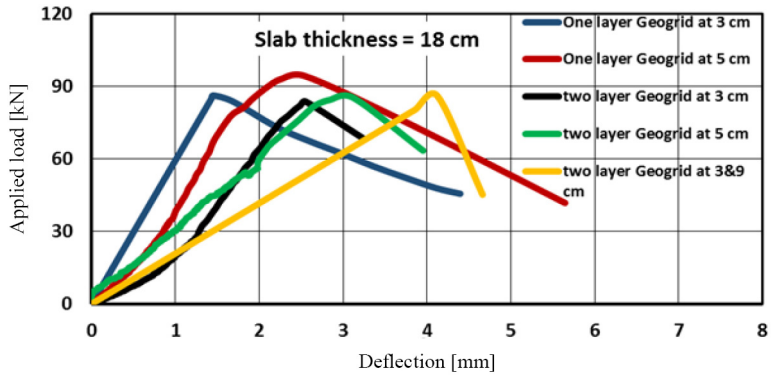

FIGURE 18. Residual load against deflection for slab with thickness of 18 cm with geogrid
Source: own work.

The maximum load, maximum deflection, deflection at maximum load, toughness, and toughness index for each specimen are shown in Table 5 for comparison. Also, Table 5 shows the deflection at maximum load, maximum deflection, toughness index, and toughness for each sample separately.

As shown in Table 5, the residual strength value increased by increasing the slab thickness value or location of geogrid from the upper face of the slab. On the other hand, the higher number of geogrid layers, the lower the residual strength value. Moreover, the results in Table 5 also show that the higher the slab thickness or the number of geogrid layers, the lower the toughness value. Three control samples were considered in this study; the control slabs contain one layer of geogrid

Ahmed, A. M. E., Hamdy, O., Saad, Y. L. Z., Ahmad, S. S. E. (2023). Residual strength and toughness after impact loading for RC slabs strengthened with different layers of geogrid. *Sci. Rev. Eng. Env. Sci.*, *32* (2), 117–134. DOI 10.22630/srees.4768

TABLE 5. Results of residual test

Sample case	Maximum load (P_{max}) [kN]	Deflection at maximum or cracked load [mm]	Maximum deflection (Δmax)	Toughness index at maximum load (Δmax/Δ)	Toughness [kN·mm]
t15 one layer of 3 cm	86.07	5.18	8.676	1.674	502.673
t15 one layer of 5 cm	90.90	9.04	12.730	1.408	732.607
t15 two layers of 3 cm	63.50	2.21	3.006	1.358	130.980
t15 two layers of 5 cm	85.00	1.48	5.521	3.742	303.580
t15 two layers of 3 and 7.5 cm	85.77	2.96	3.342	1.128	288.908
t18 one layer of 3 cm	86.28	1.45	4.394	3.030	250.940
t18 one layer of 5 cm	94.50	2.53	5.645	2.232	349.328
t18 two layers of 3 cm	83.79	2.55	3.236	1.269	145.824
t18 two layers of 5 cm	85.50	3.11	3.951	1.270	244.914
t18 two layers of 3 and 9 cm	86.00	4.13	4.661	1.130	212.616

Source: own work.

with a 3 cm upper concrete cover for slabs with thicknesses of 12 cm, 15 cm, and 18 cm. Since the 12 cm slab already damaged in the impact process so the 12 cm, control slab ignored.

The control samples were subjected to the static load test without the impact test. Its results were compared with the same corresponding impact samples, i.e., samples subjected to impact loading before the static test. Figures 19 and 20 show the static load–deflection curves for control and corresponding samples exposed to impact for both 15 and 18 slabs containing one geogrid layer with a 3 cm upper concrete cover.

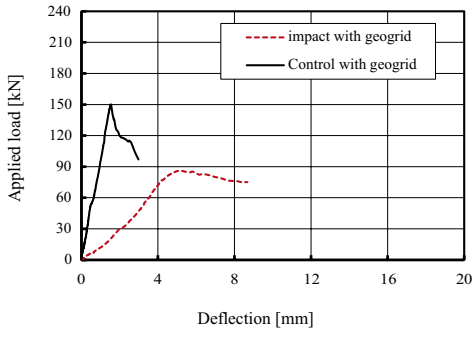

FIGURE 19. load against deflection for slab with thickness of 15 cm with one layer of 3 cm and control case

Source: own work.

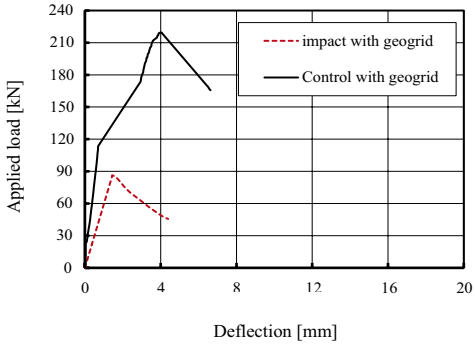

FIGURE 20. load against deflection for slab with thickness of 18 cm with one layer of 3 cm and control case

Source: own work.

Figures 19 and 20 clearly show the effect of exposing the slabs to five times the impact load on the residual load test. The residual strength ratio is calculated as a percentage value of the maximum load capacity of the samples exposed to impact loads compared to the maximum load capacity of the control samples that were exposed to static load tests only. The 50 × 50 cm slabs exposed to a five-time drop 70 kg load from 150 cm have residual forces equal to 48.6% and 48.0% for 15 cm and 18 cm slabs, respectively, of the maximum failure load capacity.

Failure modes for residual load test

This test was performed for samples that were not completely damaged after the impact test from a height of 150 cm. Figures 21–24 illustrate the mode of fracture for tested specimens under a central flexural load after the impact test. The cracks during residual test are continuing from cracks generated during the impact test or newly generated cracks during the residual test. These figures show that the number and distribution of these cracks are clearly different according to the number and location of the geogrid layers and thicknesses of the slabs.

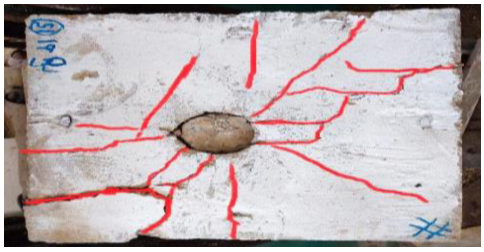

FIGURE 21. Failure mode of specimen with t15 and one layer of geogrid at 5 cm

Source: own work.

FIGURE 22. Failure mode of specimen with t15 and two layers of geogrid at 5 cm

Source: own work.

FIGURE 23. Failure mode of specimen with t18 and one layer of geogrid at 5 cm

Source: own work.

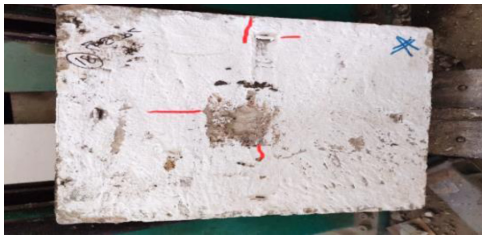

FIGURE 24. Failure mode of specimen with t18 and two layers of geogrid at 5 cm

Source: own work.

As shown from previous Figures, more slab thickness, fewer cracks' numbers or length, more geogrid layers, fewer cracks' numbers or length occurred, especially for double layers with the same concrete cover.

Conclusions

The subsequent conclusions from this experiment are:

1. The increase in the slab thickness gives an enhancement in the strength and residual strength.
2. Moreover, as the location of geogrid from the slab's upper surface increased, the strength, residual strength, and toughness improved.
3. The higher numbers of geogrid layers have a negative effect on the strength.
4. The higher the slab thickness or the number of geogrid layers, the lower the toughness value.
5. The residual strength of the slabs reinforced with upper geogrid after the impact test equals around 48% of the maximum failure load of the same slab.
6. A geogrid reduced the number and distribution of cracks and mitigated their severity more than that of specimens without a geogrid, especially for double layers with the same concrete cover.
7. Because of no rust in geogrids, that allows putting geogrid very near the surface, which leads to a greater capability of shrinkage resisting and preventing surface cracks.

References

Ahmad, S. S., Seleem, M. H., Badaway, A. A. & El Safoury, A. (2016). *Fracture and damage in high-performance concrete under impact loading*. Retrieved from: https://www.researchgate.net/profile/SeleemAhmad/publication/279445985_Flexural_behavior_of_fiber_reinforced_concrete_slabs_under_central_impact_load/links/582abf3008aef19cb805fecd/Flexural-behavior-of-fiber-reinforced-concrete-slabs-under-central-impact-load.pdf [accessed: 30.01.2023].

Al Qadi, A. N., Al-Kadi, Q. N. & Al-Zaidyeen, S. M. (2015). Impact strength of oil-palm shell on lightweight concrete slabs reinforced with a geo-grid. *Journal of Materials in Civil Engineering*, *27* (10), 04014264.

Chidambaram, R. S. & Agarwal, P. (2014). The confining effect of geo-grid on the mechanical properties of concrete specimens with steel fiber under compression and flexure. *Construction and Building Materials*, *71*, 628–637. https://doi.org/10.1016/j.conbuildmat.2014.08.059

Chidambaram, R. S. & Agarwal, P. (2015). Flexural and shear behavior of geo-grid confined RC beams with steel fiber reinforced concrete. *Construction and Building Materials*, *78*, 271–280. https://doi.org/10.1016/j.conbuildmat.2015.01.021

Dong, Y. L., Han, J. & Bai, X. H. (2011). Numerical analysis of tensile behavior of geogrids with rectangular and triangular apertures. *Geotextiles and Geomembranes*, *29* (2), 83–91. https://doi.org/10.1016/j.geotexmem.2010.10.007

Egyptian Organization for Standardization & Quality [EOS] (2015). *Steel for the reinforcement of concrete. Part 2: Ribbed bars* (ES 262-2/2015). Cairo: Egyptian Organization for Standardization & Quality [in Arabic].

El Meski, F. & Chehab, G. R., (2014). Flexural behavior of concrete beams reinforced with different types of geogrids. *Journal of Materials in Civil Engineering*, *26* (8), 04014038. https://ascelibrary.org/doi/10.1061/%28ASCE%29MT.1943-5533.0000920

Elsayed, A., Hamdy, O., Saad, Y. & Ahmad, S. (2023). Assessment of shrinkage strain reduction SSR for RC slabs with different thicknesses strengthen with different layers of geogrid. *The Egyptian International Journal of Engineering Sciences and Technology*, *41* (1), 48–55.

Fares, A. E. R., Hassan, H. & Arab, M. (2020). Flexural behavior of high strength self-compacted concrete slabs containing treated and untreated geogrid reinforcement. *Fibers*, *8* (4), 23. https://doi.org/10.3390/fib8040023

Ganesh, A. C., Muthukannan, M., Dhivya, M., Sangeetha, C. B. & Daffodile, S. P. (2020). Structural performance of hybrid fiber geopolymer concrete beams. *IOP Conference Series: Materials Science and Engineering*, *872* (1), 012155. https://doi.org/10.1088/1757-899X/872/1/012155

Ibrahim, H. M., Turk, A. M. & Fares, A. M. (2020). Effect of slab thickness on the behavior of concrete slabs containing geogrid layers as reinforcement. *International Journal of Advanced Research in Science, Engineering and Technology*, *7* (7), 14999–14307.

International Organization for Standardization [ISO] (2007). *Steel for the reinforcement of concrete. Part 2: Ribbed bars* (ISO 6935-2:2007). Geneva: International Organization for Standardization.

Meng, X., Jiang, Q. & Liu, R. (2021). Flexural performance and toughness characteristics of geogrid-reinforced pervious concrete with different aggregate sizes. *Materials*, *14* (9), 2295. https://doi.org/10.3390/ma14092295

Mohammed, S. I. & Najim, K. B. (2020). Mechanical strength, flexural behavior and fracture energy of Recycled Concrete Aggregate self-compacting concrete. *Structures*, *23*, 34–43. https://doi.org/10.1016/j.istruc.2019.09.010

Muda, Z. C., Malik, G., Usman, F., Beddu, S., Alam, M. A., Mustapha, K. N., Birima, A. H., Zarroq, O. S., Sidek, L. M. & Rashid, M. A. (2013). Impact resistance of sustainable construction material using light weight oil palm shells reinforced geogrid concrete slab. *IOP Conference Series: Earth and Environmental Science*, *16*, 012062. https://doi.org/10.1088/1755-1315/16/1/012062

Nishanthi, P., Vidjeapriya, R., Sivaram, S., Sathish, K., Bharath, K. & Muhammed Mukhthar Khan, M. K. (2021). Effect of geo-grid and steel fibres on flexural behaviour of reinforced concrete beams. *Materials Today: Proceedings*, *47*, 4597–4605. https://doi.org/10.1016/j.matpr.2021.05.452

Ou, Y. C., Tsai, M. S., Liu, K. Y. & Chang, K. C. (2012). Compressive behavior of steel-fiber--reinforced concrete with a high reinforcing index. *Journal of Materials in Civil Engineering*, *24* (2), 207–215. https://ascelibrary.org/doi/10.1061/%28ASCE%29MT.1943-5533.0000372

Su, N. & Fan, X. (2021). Experimental Study on Flexural Toughness of Steel-Polyvinyl Alcohol Hybrid Fiber Reinforced Concrete. *IOP Conference Series: Earth and Environmental Science*, *719* (2), 022080. https://doi.org/10.1088/1755-1315/719/2/022080

Vijay, T. J., Kumar, K. R., Vandhiyan, R., Mahender, K. & Tharani, K. (2020). Performance of geogrid reinforced concrete slabs under drop weight impact loading. *IOP Conference Series: Materials Science and Engineering*, *981* (3), 032070.

Vijay, T. J., Raj, A. V. S. & Babu, M. S. (2021). Experimental investigation of concrete beams reinforced with polypropylene bars. *Materials Today: Proceedings*, *37*, 1654–1658. https://doi.org/10.1016/j.matpr.2020.07.181

Yousif, M. A., Mahmoud, K. S., Abd Hacheem, Z. & Rasheed, M. M. (2021). Effect of geogrid on the structural behavior of reinforced concrete beams. *Journal of Physics: Conference Series*, *1895* (1), 012048. https://doi.org/10.1088/17426596/1895/1/012048

Yahaghi, J., Muda, Z. C. & Beddu, S. B. (2016). Impact resistance of oil palm shell concrete reinforced with polypropylene fibre. *Construction and Building Materials*, *123*, 394–403. https://doi.org/10.1016/j.conbuildmat.2016.07.026

Ye, Y., Liu, J., Zhang, Z., Wang, Z. & Peng, Q. (2020). Experimental study of high-strength steel fiber lightweight aggregate concrete on mechanical properties and toughness index. *Advances in Materials Science and Engineering*, *2020*, 1–10. https://doi.org/10.1155/2020/5915034

Summary

Residual strength and toughness after impact loading for RC slabs strengthened with different layers of geogrid. This study presents an experiment for investigating the residual strength and toughness of reinforced concrete, RC, and slab reinforced by a geogrid as shrinkage reinforcement along with lower tensile steel reinforcement. Three different parameters were considered: slab thickness, number of geogrid layers, and thickness of the upper concrete cover. Fifteen slab samples with sizes of 50 × 50 cm exposed to the impact load on its center before being re-loaded by the static load and six slab samples exposed to the static load only. The load and deflection relation were recorded through the static loading process for all specimens, where loading capacity, toughness, and toughness index were measured. The results show an enhancement in the slabs residual strength as the slab thickness and concrete cover increased. On the other hand, the residual strength of slabs has a remarkable decrease with the increase in geogrid layers. Moreover, the toughness has a positive relation with the concrete cover and has an inverse relation with the slab thickness and the number of layers. A geogrid reduced the number and distribution of cracks and mitigated their severity, especially for double layers with the same concrete cover.

Scientific Review Engineering and Environmental Sciences (2023), 32 (2), 135–154

Sci. Rev. Eng. Env. Sci. (2023), 32 (2) https://srees.sggw.edu.pl

ISSN 1732-9353 (suspended) eISSN 2543-7496 DOI 10.22630/srees.4548

Received: 19.11.2023
Accepted: 28.03.2023

Rafi Mohammed QASIM https://orcid.org/0000-0002-1882-0766
Tahseen Ali JABBAR https://orcid.org/0000-0002-0602-9627
Safaa Hameed FAISAL✉ https://orcid.org/0000-0002-7752-9071
Southern Technical University, Basra Engineering Technical College, Basra, Iraq

Simulation of laminar flow passing through a T-splitter plate and bridge pier

Keywords: hydrodynamic laminar flow, open channel, pier, splitter plate

Introduction

The flow around the pier represents a serious subject due to the direct relationship between the structural hydraulic collapse and the stability of the upper structure, which is supported by the pier. The erosion in the soil particle depends mainly on the flow velocity, water depth and the size of the soil particle. Here, the flow velocity has a major impact on the erosion process regardless of the type of flow as compared with the remaining previous factors. Therefore, the type of flow has a direct influence on the stability of mobile material (soil bed). Here, the hydraulic designer encounters a noticeable challenge based on how we satisfy a reasonable balance between a huge hydraulic field and the structural resistance to this hydraulic field without any negative aspect on the serviceability life of the pier. However, to protect the pier against the hydraulic field, several ways must be applied to produce a proper equilibrium between the hydraulic field and pier stability, therefore

✉s_hfaisal100@stu.edu.iq

this problem gives evidence regarding the risk that may occur when the hydraulic field suddenly alters its behavior. Several papers dealt with water fields around the pier. Here, we mention some of these significant papers. In general, the previous paper adopted a splitter plate with a rectangular shape. The rectangular shape will divide the flow in two directions along the solid boundary side of the plate. Thus, only the separation process will be developed at the corner edge of the rectangular shape and these separation points constitute fixed separation points. The authors suggest duplicating the separation process with the dissipation process, therefore they use the T-shaped splitter plate. The T-shaped splitter plate consists of two parts; the first part is longitudinal, which is parallel to the flow direction, while the second part is transverse, which is perpendicular to the flow direction. Here, the expected dissipation process will occur largely in the second part in addition to the separation process, which occurs at the corner edge of the second part. Qasim, Jabbar and Abdulhussein (2022a), Jabbar, Qasim and Mohammed (2022a), as well Qasim and Jabbar (2021) tried to produce safe hydrodynamic fields around a pier by installing a vane at the upstream part of the pier. These efforts gave a good indicator regarding the way we dominate the hydrodynamic field and this is shown clearly in the reduction, which is earned especially in the drag coefficient. Furthermore, these papers dealt with several hydraulic parameters and implied how the vane made the reduction in these parameters at a feasible level. Shen, Lin, Wei, Dou and Tu (2019) achieved an experimental work to reveal the characteristics of the vortex shedding behind a cylinder under the impact of the flexible film, in this experimental study the ratio of the flexible film length to the cylinder diameter L/D and Reynolds number is increased. This research focused on efforts to identify the effect of the flexible film flapping with various L/D parameters on the distribution of the fluctuation pressure and the vortex shedding frequency. Hu and Wang (2013) used the particle imaging velocimetry (PIV) to study the structure of the flow around an oscillating cylinder attached to a flexible tail. The paper concentrated on the flow velocity along the wake center line as well as the vertical flow velocity around the flexible tail trailing edge. Shukla, Govardhan and Arakeri (2013) investigated the issue of a flexible splitter plate in the wake of a cylinder experimentally; the plate flexural rigidity has been adopted in the investigation. Meanwhile, the Reynolds number value depends on the cylinder diameter. Periodic splitter plate motions are shown to exist in two regimes. Ahmed (2015) conducted a numerical analysis of vortex shedding while taking laminar flow with $30 \leq \mathrm{Re} \leq 300$ into consideration. The numerical solution of the hydraulic issue uses two-dimensional, incompressible, and unsteady flow. The results also showed that the flow is asymmetric and unsteady at Reynolds numbers over 60, and

a strong comparison could be made between the findings with those of studies that were conducted earlier. Govardhan and Williamson (2000), as well as Carberry, Sheridan and Rockwell (2005), discovered the mechanism that started the changes in the phase and amplitude of the lift force, also the relations with the mod of vortex shedding. Mehdi, Namdev, Kumar and Tyagi (2016) performed a numerical solution in two-dimensions to study the flow around a cylinder. Here, three values of the Reynolds number are used, which are 1,000, 500, and 200 with various values of attack angles 10°, 5°, and 0°. The numerical investigation concentrated on vortex shedding, drag coefficient, and pressure. Bai and Li (2011) implemented a two dimensional flow analysis around the cylinder numerically for seeking the hydrodynamic pattern characteristics. The flow is simulated as unsteady, uniform, and laminar. The study focused on the Strouhal number, lift coefficient, drag coefficient, and pressure distribution, the study adopted Re = 200. Dennis and Chang (1970) utilized the formulation of stream-vorticity and discretization of finite difference to find a solution for a steady incompressible flow across the cylinder up to Re = 100. Henderson (1995) utilized the spectral element method to calculate the base pressure, pressure drag, and viscous drag for the flow around a cylinder, which has a circular cross-section. Recently, Qasim, Jabbar and Faisal (2022b) have investigated the hydrodynamic field response of a cylindrical pier due to using a curved vane with the assumption of a laminar flow. They observed alteration in the direction of the flow velocity, especially at the leading and rear surfaces of the curved vane due to the existence of flow separation and dissipation along the boundary of the vane. Jabbar, Qasim and Faisal (2022b) studied the flow characteristics around a circular pier that adjacent T-shape splitter in a numerical manner. The analysis includes vortex's length, streamlines, flow velocity contour, and pressure contour. They found that the streamlines, flow velocity field, and pressure field are affected mainly by the horizontal distance between the rear part of the splitter and the pier center. In addition, the Re number will directly control the streamlines, flow field, and pressure field. Qasim, Faisal and Jabbar (2022c) introduced another study about the hydrodynamic behavior surrounding the pier near a T-shape splitter. The study covers water velocity contours, pressure contours, and streamlines. Results reveal that bubbles are developed due to the presence of the splitter and the size and length of these bubbles are controlled by the Reynolds number.

The aim of this paper can be summarized into the following points:

1. Investigate the velocity vector around a bridge pier to understand the direction of water flow due to the existence of a T-splitter plate. Here, various values of the Reynolds number are used with a constant value of ratio X (ratio X is defined later in the next section).

Qasim, R. M., Jabbar, T. A., Faisal, S. H. (2023). Simulation of laminar flow passing through a T-splitter plate and bridge pier. *Sci. Rev. Eng. Env. Sci.*, *32* (2), 135–154. DOI 10.22630/srees.4548

2. Investigate the drag coefficient and lift coefficient for two different cases, considering various values of the Reynolds number and horizontal distance between the leading part of the pier and the rear part of T-splitter plate.

3. Investigate the skin friction coefficient for two different cases, considering various values of Reynolds number and horizontal distance between the leading part of the pier and the rear part of T-splitter plate.

Methodology

The entire hydraulic problem comprises of three parts, which are the fluid, a circular pier, and a T-shaped splitter plate. The numerical model is accomplished in two dimensions and the flow is considered to be laminar. The values of the Reynolds number, which is used to implement the hydraulic analysis, are 40, 80, 120, and 200. The calculated Reynolds number is based on the pier diameter and flow velocity. The stream flow of water starts from the left, first crosses the T-splitter, and then moves towards the circular pier. The hydraulic analysis deals with two different cases, which are illustrated in Figure 1. Furthermore, Figure 1 depicts the hydraulic dimensions of the fluid domain. Here, the T-splitter plate produces

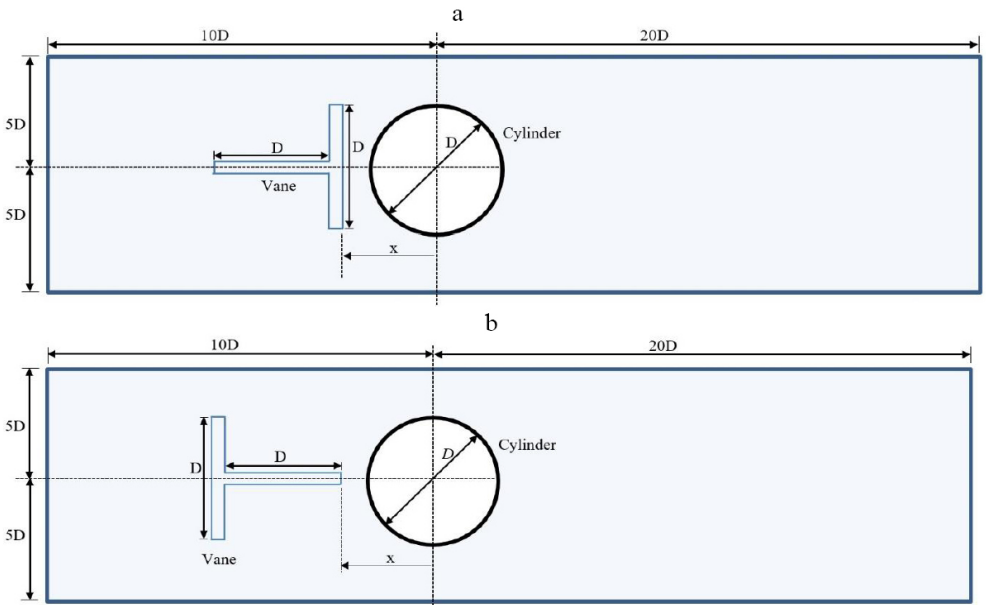

FIGURE 1. The hydraulic domain including the cylinder and T-splitter plate: a – Case 1; b – Case 2
Source: own work.

a deformation to the water flow when the flow passes the splitter, therefore the flow field around the pier is always changing based on flow separation and dissipation. The T-splitter plate arm's dimensions are equal to the diameter of the pier. Various locations of T-splitter plate reference to the location of the pier are investigated in the current study. Here, x refers to the horizontal distance from the pier center to the rear part of the splitter plate.

The steady flow analysis is implemented by ANSYS Fluent and in all cases, the splitter plate is considered to be rigid. The governing equations that will be used for the simulation and solved by the software are incompressible fluid continuity equation and the conservation of momentum equation as given in Eqs (1)–(3), (Dahkil, Gabbar & Jaber, 2014; Sharma & Barman, 2020).

$$u\frac{\partial u}{\partial x}+v\frac{\partial u}{\partial y}=-\frac{1}{\rho}\frac{\partial P}{\partial x}+\frac{\mu}{\rho}\left(\frac{\partial^2 u}{\partial x^2}+\frac{\partial^2 u}{\partial y^2}\right). \tag{1}$$

$$u\frac{\partial v}{\partial x}+v\frac{\partial v}{\partial y}=-\frac{1}{\rho}\frac{\partial P}{\partial y}+\frac{\mu}{\rho}\left(\frac{\partial^2 v}{\partial x^2}+\frac{\partial^2 v}{\partial y^2}\right). \tag{2}$$

$$\frac{\partial(u)}{\partial x}+\frac{\partial(v)}{\partial y}=0. \tag{3}$$

The calculations are performed using the default commercial CFD code in ANSYS Fluent 2020 R1. The feeding information submitted to the fluent software is the inlet flow velocity, while the output data includes the flow velocity components and the pressure magnitude. The discretization equations are solved using the semi-implicit method for pressure-linked equations (SIMPLE) method and formula from the upwind scheme. Furthermore, the convergence criteria is 1E – 4 for momentum equations and 1E – 6 for energy equation. The simulation was performed with an 8 GB RAM Intel Core i7 processor.

The drag coefficient (CD) is defined as:

$$CD=\frac{F_D}{\frac{1}{2}\rho U_\infty^2 A_{ref}}, \tag{4}$$

where F_D is the drag force, U_∞ is the free-stream velocity, and A_{ref} is the reference area. The reference area in this case is the projection area, which is equal to the diameter for the unit depth.

Qasim, R. M., Jabbar, T. A., Faisal, S. H. (2023). Simulation of laminar flow passing through a T-splitter plate and bridge pier. *Sci. Rev. Eng. Env. Sci.*, *32* (2), 135–154. DOI 10.22630/srees.4548

Concerning lift coefficient (CL) is defined by:

$$CL = \frac{F_L}{\frac{1}{2}\rho U_\infty^2 A_{ref}}, \tag{5}$$

where F_L is the lift force. The reference area (wing area) is also equal to the diameter for unit depth.

The skin friction factor is obtained from the formula:

$$Cf = \frac{\tau_L}{\frac{1}{2}\rho U_\infty^2}, \tag{6}$$

where τ_L is the shear stress at the wall.

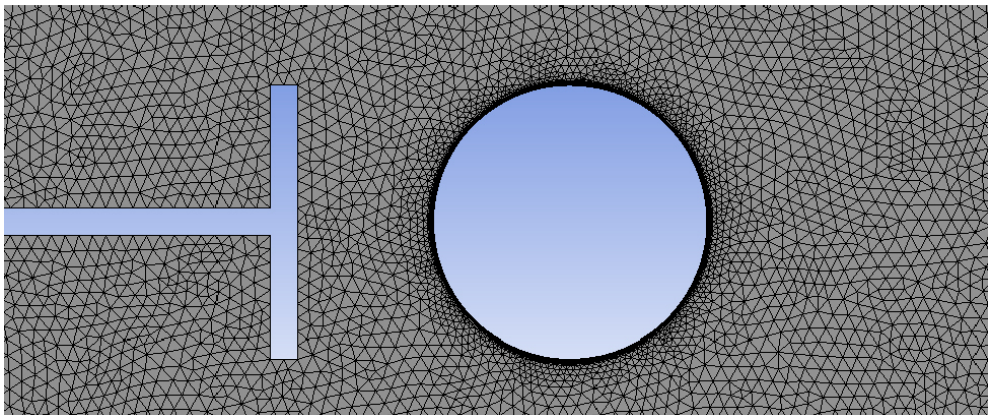

FIGURE 2. Mesh geometry of Case 1
Source: own work.

The element specifications adopted in this study are: the number of the element is 71,566 elements for Case 1 and 71,267 elements for Case 2, triangle mesh type, and the diameter of the cylinder-to-element size ratio of 20. Figure 2 shows the mesh of Case 1 and Table 1 illustrates the boundary conditions applied for the entire hydraulic system. The mesh is

TABLE 1. Boundary conditions

Inlet	Velocity
Outlet	pressure
T-splitter and pier	no-slip
Channel bed and sides	no-slip

Source: own work.

concentrated highly around the pier and the splitter plate. The smooth mesh is employed for both cases. The properties of water are taken as ρ = 997.1 kg·m^{-3} and μ = 89.05E – 5 kg·s^{-1}·m^{-1}.

Referring to Figure 1, the ratio X is defined as:

$$X = \frac{x}{D}, \tag{7}$$

where x is the horizontal distance between the leading part of the pier and the rear part of the T-splitter plate. The pier diameter is denoted by D.

Validation

It is very important to check the effectiveness of the used software. Here, before solving the current problem, we check the software by adopting a previous case study performed by Rajani, Kandasamy and Majumdar (2009). Depending on the comparative study between the result of the previous paper and the current result, it is apparent that there is no fluctuation among the results. Therefore, we can now start the required analysis of the current hydraulic problem. Figure 3 reveals that the separation angle decreases with the increase of the Reynolds number. Both studies (previous and current) are achieved in a two-dimensional flow analysis.

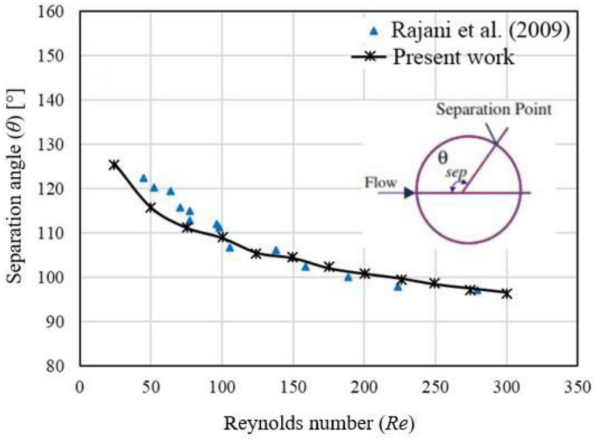

FIGURE 3. The variation of separation angle (θ) with Reynolds number (Re)
Source: own work.

Qasim, R. M., Jabbar, T. A., Faisal, S. H. (2023). Simulation of laminar flow passing through a T-splitter plate and bridge pier. *Sci. Rev. Eng. Env. Sci.*, *32* (2), 135–154. DOI 10.22630/srees.4548

Results and discussion

In this paper, two different cases have been investigated and compared. The target is to show the direct influence of the splitter plate on the hydrodynamic patterns around the bridge pier. The hydraulic problem is analyzed by adopting fluid with the same physical properties for both cases. Here, water is the flow material around the splitter plate and pier. Figure 4 shows the velocity vector for Case 1 considering Re and ratio X. We take four points to understand the velocity vector behavior, two approximately counterpoints located at the leading portion of the pier or in other words these two points fall on the boundary layer zone while the other counterpoints located at the rear portion of the pier or fall on the wake zone. For the case Re = 40 and $X = 1.2$, for points at the leading of the pier, we notice the flow is divided into two portions. Here, a portion goes toward the zone between the splitter plate and the pier leading portion while the remaining flow portion goes toward the wake zone. Now, for points at the rear of the pier, we noticed that flow comes from the boundary layer zone combined with the flow at the rear of the pier and goes toward the hydraulic system downstream. The same hydraulic behavior remains without any alteration for the following cases Re = 80 and ratio $X = 1.2$ and Re = 140 and ratio $X = 1.2$. When Re becomes 200 and the ratio X is constant, dramatic hydraulic behavior in the flow will take place, here, we investigate the flow at the pier circumference on both sides along the boundary zone and wake zone. We find that the flow at the wake zone tends to move towards the boundary zone, while a small quantity of flow moves towards the downstream of the pier. We must bring to light two different processes, which happened to the flow stream before crossing the rear portion of the splitter plate. These processes are separation and dissipation processes. In Case 1 the flow will first be separated by the longitudinal splitter plate and then the flow will be reflected by the transverse splitter plate. Here, the flow velocity will vary due to the unbalanced processes that occurred to the flow velocity at the splitter plate. Therefore, the flow suffers from the losses in energy and changing in its direction. Therefore, some water goes to fill the gap (distance) between the rear portion of the splitter plate and the leading portion of the bridge pier while the remainder goes toward the wake zone. Now for the flow between the splitter plate and the pier, at the pier boundary layer zone, the flow suffered from losses in kinetic energy or losses in the flow velocity. Moreover, some flow recirculates to the wake zone and some recirculates in the zone between the rear portion of the splitter plate and the leading portion of the pier, as well this flow will suffer from the losses in the flow velocity. The value of the Reynolds number will contribute to the disturbance of the flow velocity vector. With the rise in Reynolds number value, the water flow suffered tremendous changes in the flow velocity magnitude and direction.

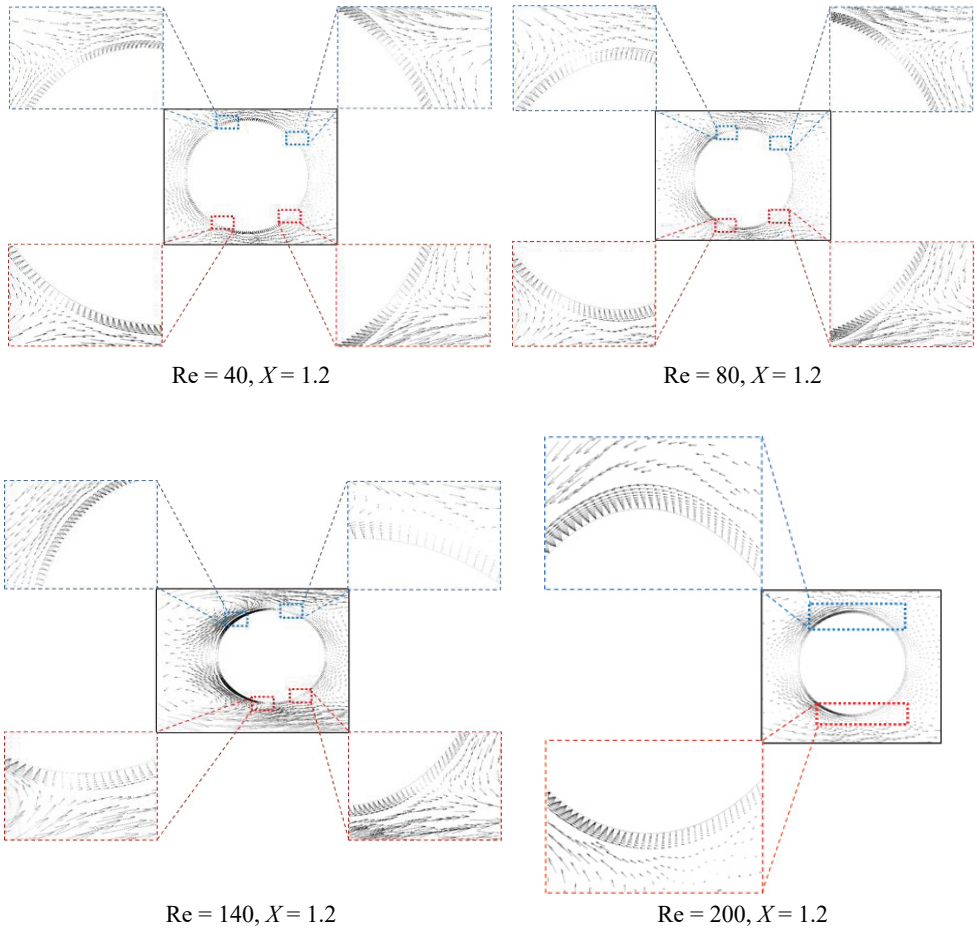

FIGURE 4. Indicates the velocity vector for Case 1
Source: own work.

Figure 5 shows the velocity vector for Case 2 considering Re and the ratio *X*. The same procedure, which is adopted in Case 1 is employed to investigate Case 2. When Re = 40 and Re = 80 with a constant value of ratio *X*, the hydraulic behavior in Case 2 is similar to the hydraulic behavior of Case 1, while when Re = 140 and Re = 200 with a constant value of the ratio *X* there is no identically in the hydraulic behavior, i.e with the increase in flow velocity, the hydraulic behavior will be changed according to the magnitude of velocity. Here, approximately the entire flow diverted its direction toward the gap (distance) between the leading portion of the pier and the rear portion of the splitter plate. For this event, the water flow suffered from the separation process

Qasim, R. M., Jabbar, T. A., Faisal, S. H. (2023). Simulation of laminar flow passing through a T-splitter plate and bridge pier. *Sci. Rev. Eng. Env. Sci.*, *32* (2), 135–154. DOI 10.22630/srees.4548

at the splitter plate and losing (shortages) of the kinetic energy at the circumference of the pier leading portion. The remaining flow goes immediately towards the wake zone.

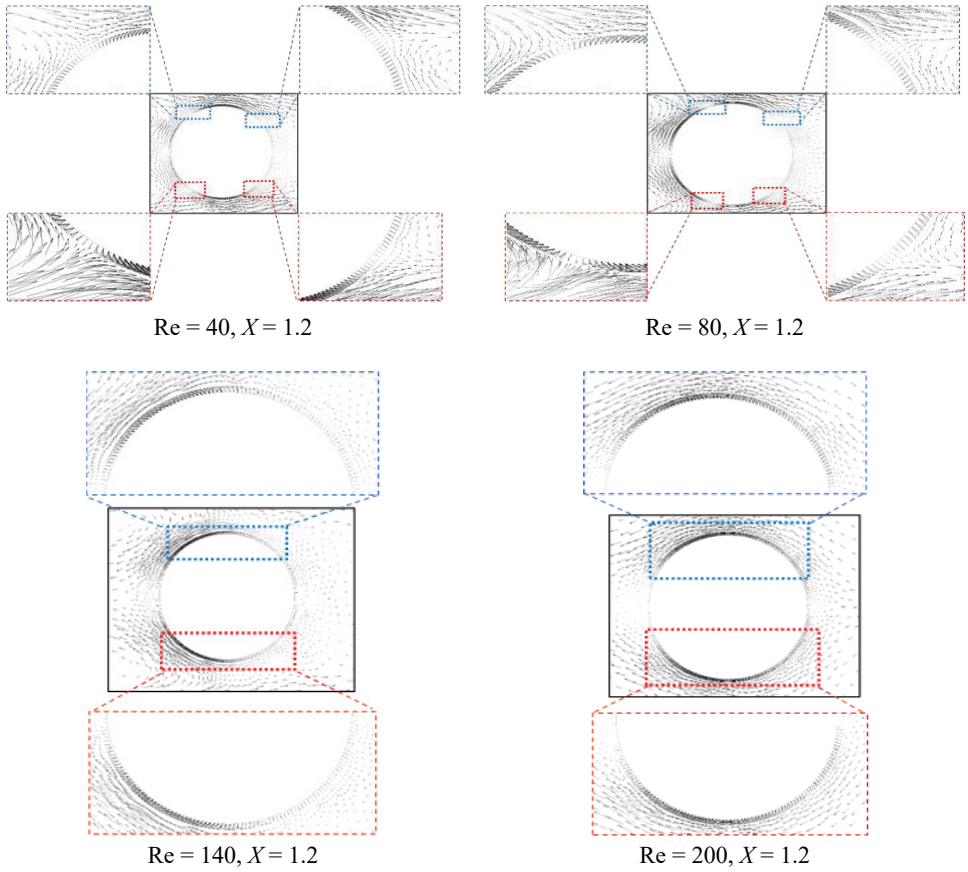

FIGURE 5. Indicates the velocity vector for Case 2
Source: own work.

The variation of the drag coefficient ratio of the bridge pier with the ratio X is outlined in Figure 6. From the figure, we can infer that the drag coefficient of the pier nearby the T-splitter plate is less than the drag coefficient of the pier alone. A nonlinear trend in relation is found among various values of the drag coefficient ratio with the ratio X. In spite of the variation in the Reynolds number values, negative drag coefficient values are found regardless of the values of the ratio X. On the front surface

of the pier, the stagnation pressure is reduced due to the existence of the upstream T-splitter plate. When the pressure is reduced, the flow velocity will rise and this rising leads to a reduction in the drag coefficient. The figure shows that there is a slight variation in the curve trend when Re = 140 and Re = 200 as compared to the others. In addition, the variation in the lift coefficient ratio of the bridge pier with the ratio X is outlined in Figure 7. The values of the lift coefficient vary among negative values and positive values with various values of the ratio X. It is shown that no dramatic change in the lift coefficient values regardless of the values of the Reynolds numbers and all the obtained values of the lift coefficient are close together. From Figures 6 and 7, we can conclude that as the drag coefficient increases, the lift coefficient decreases. In the laminar flow, negative lift coefficients exist due to the low angle of attack.

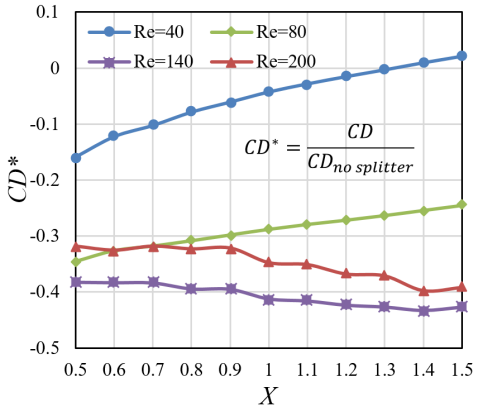

FIGURE 6. Drag coefficient (CD*) for Case 1
Source: own work.

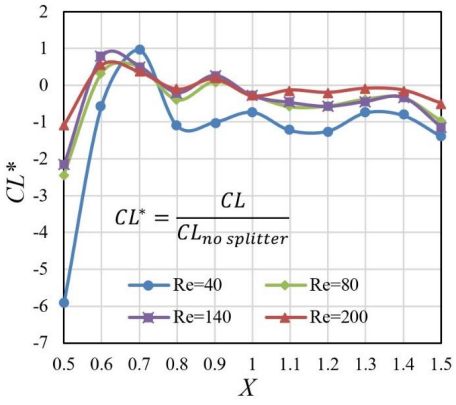

FIGURE 7. Lift coefficient (CL*) for Case 1
Source: own work.

Figures 6 and 7 are drawn for Case 1. For Case 2, Figure 8 illustrates the variation in the drag coefficient ratio with the ratio X for various values of the Reynolds numbers. The behavior of the drag coefficient for Case 2 is similar to the behavior of Case 1 except that the trend in Case 2 varied in terms of the linear and non-linear aspect. The alteration in trend relies on the flow velocity. Here, the flow velocity is based on the separation and dissipation processes and which one will occur first. Figure 9 illustrates the variation in the lift coefficient ratio with the ratio X for various values of the Reynolds numbers. It is clear from Figure 9 that all values of the lift coefficient are equal to or approximate to zero, this is due to shortages in the flow mass, which produce the lift in the pier.

Qasim, R. M., Jabbar, T. A., Faisal, S. H. (2023). Simulation of laminar flow passing through a T-splitter plate and bridge pier. *Sci. Rev. Eng. Env. Sci.*, *32* (2), 135–154. DOI 10.22630/srees.4548

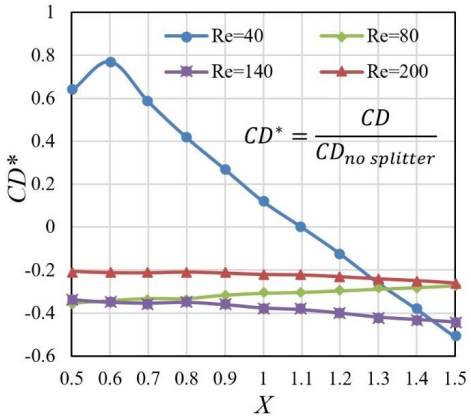

FIGURE 8. Drag coefficient (*CD**) for Case 2
Source: own work.

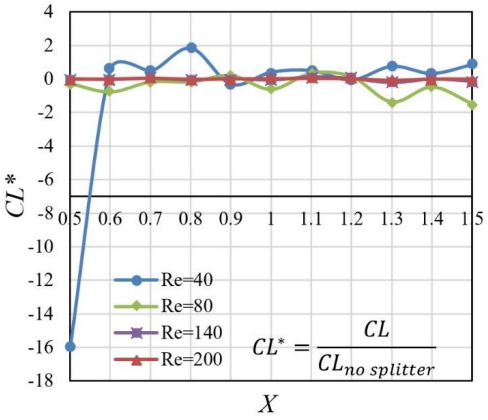

FIGURE 9. Lift coefficient (*CL**) for Case 2
Source: own work.

Figure 10 reveals a comparative study between the drag coefficient ratio of the two cases taking into consideration four different values of the Reynolds number and various values of the ratio *X*. The argument here relies on the fact which processes occur at the leading portion of the T-splitter plate, leading portion of the pier, and rear portion of the T-splitter plate. In addition, the kinetic energy flow suffers losses. From the figure, for Re = 40, the curve of Case 1 has a moderate trend while the curve of the Case 2 drops sharply from positive values to negative values without any contrast. When Re = 80, the curves of both cases rise dramatically without any variation. Also, when Re = 140 and Re = 200 both curves drop sharply without any fluctuation. From Figure 10 we can deduce the benefit of installing a splitter plate at the upstream of the bridge pier in order to reduce the drag coefficient and produce a suitable flow field around the pier to prevent pier collapse under hydraulic loading and keep safe applied hydraulic loading.

Figure 11 is drawn to express the relation between the skin friction coefficient ratio and the ratio *X* for different values of the Reynolds numbers. We deduce that the skin friction of the bridge pier alone is greater than the skin friction of the bridge pier nearby the splitter plate. It is obvious from the Figure as the ratio *X* increases, the skin friction coefficient increases as well regardless of the value of the Reynolds number. In general, skin friction or skin friction drag is caused by fluid viscosity and relies on flow velocity and the projection area of the pier that has direct contact with the fluid. For the contact area in case of the splitter plate existence or without splitter plate existence, the area is always constant. Here, the flow velocity has a vital role in determining the skin friction value. When the Reynolds number increases, it

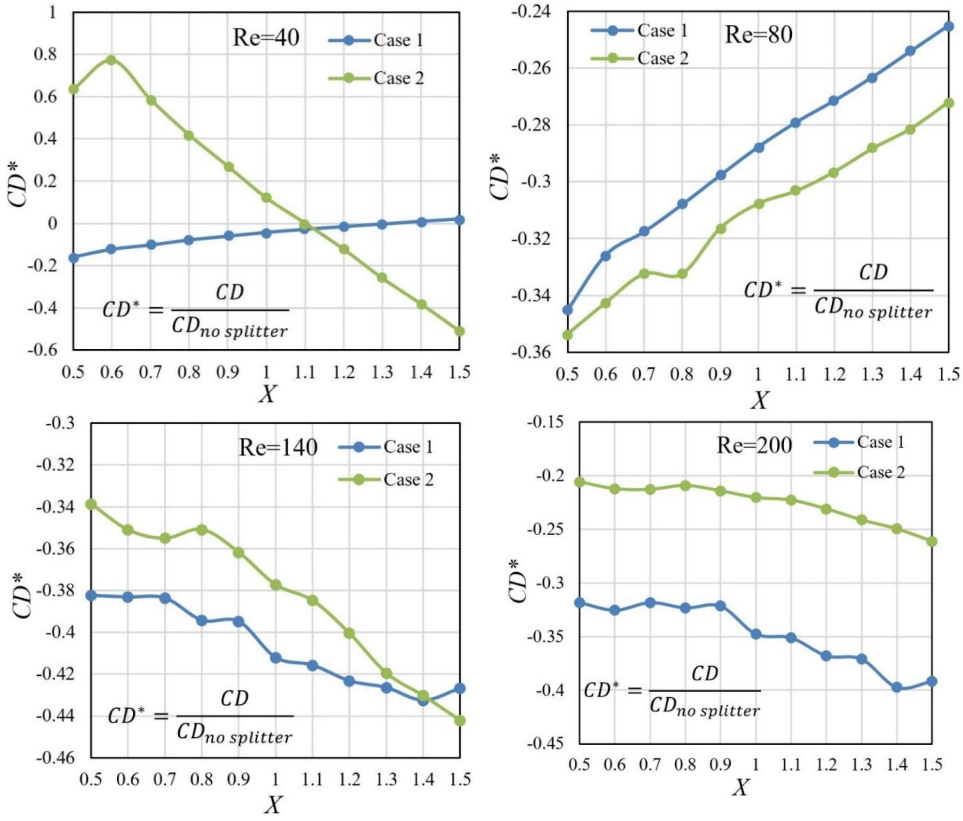

FIGURE 10. Variation of drag coefficient (CD^*) with the ratio X for various values of Reynolds number (Re)

Source: own work.

means that the viscous force will decrease together with the skin friction coefficient. Therefore, the Reynolds number is independent of the skin friction, this situation is clear in the figure, at Re = 40 where the blue curve represents the upper limit, while the remaining curves of Re greater than 40 fall under the curve which has Re = 40. Moreover, laminar sub-layer thickness decreases with an increase in the Reynolds numbers values. All curves in Figure 11 have a nonlinear trend.

Figure 12 shows the variation in relation between the skin friction ratio and different Reynolds numbers values for three different values of the ratio X. It is evident from the figure as the Reynolds number increases, the skin friction ratio decreases and this condition is discussed in the previous section but here we noticed that the distance between the splitter plate and the bridge pier does not affect the skin friction value. That is because skin friction depends directly on fluid viscosity and flow

Qasim, R. M., Jabbar, T. A., Faisal, S. H. (2023). Simulation of laminar flow passing through a T-splitter plate and bridge pier. *Sci. Rev. Eng. Env. Sci.*, *32* (2), 135–154. DOI 10.22630/srees.4548

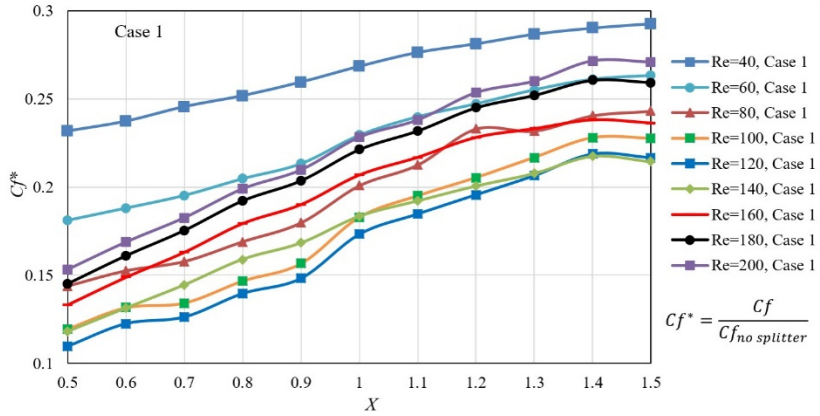

FIGURE 11. Relation between skin friction ratio (*Cf**) and ratio *X* for Case 1

Source: own work.

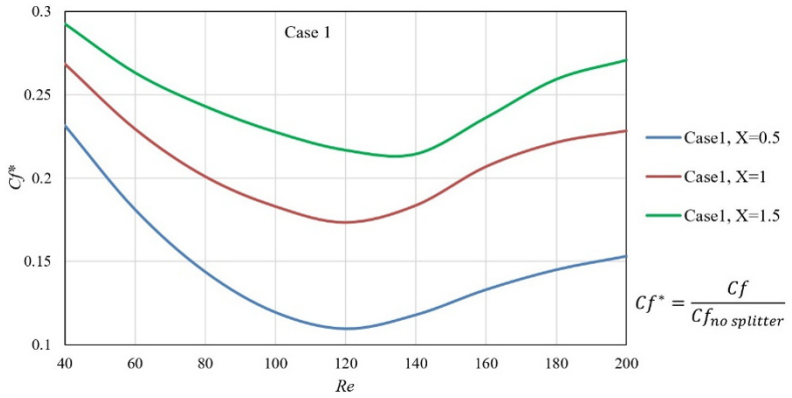

FIGURE 12. Relation between skin friction ratio (*Cf**) and Reynolds numbers (Re) for Case 1

Source: own work.

velocity magnitude. Also, we can see from the figure a nonlinear trend in the relation between the Reynolds numbers and the skin friction ratio.

Figure 13 and Figure 14 are drawn for Case 2. Figure 13 is outlined to express the relation between the skin friction coefficient ratio and the ratio *X* for different values of the Reynolds numbers. Figure 14 shows the variation in relation between skin friction ratio and different Reynolds numbers values for three different values of the ratio *X*. In both figures, the hydraulic behavior of Case 2 is similar to the hydraulic behavior of Case 1 regardless of the configuration of the T-splitter plate. All the curves in Figure 14 have a harmonic trend as compared with curves in Figure 12, this feature is attributed to the flow velocity magnitude.

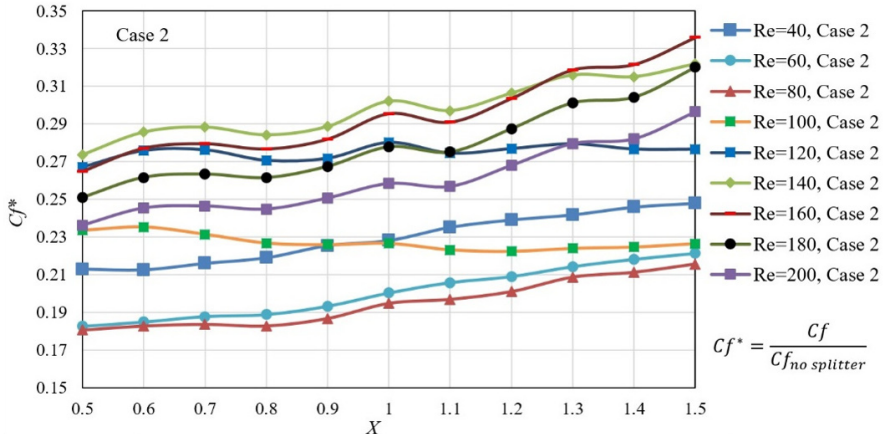

FIGURE 13. Relation between skin friction ratio (Cf^*) and ratio X for Case 2
Source: own work.

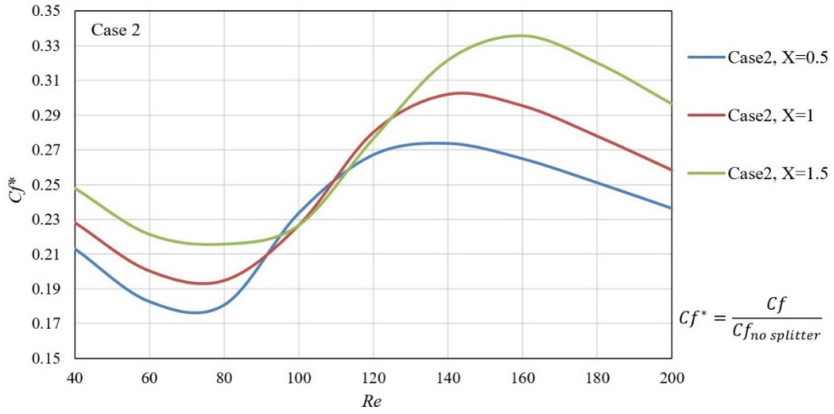

FIGURE 14. Relation between skin friction ratio (Cf^*) and Reynolds number (Re) for Case 2
Source: own work.

Figure 15 reveals the relation between the skin friction coefficient and the Reynolds number for both cases (1 and 2) considering various values of the ratio X. When the ratio X is equal to 0.5 and 0.6, the curve of Case 1 and the curve of Case 2 intersect at Re = 60 and Cf^*. When the ratio X is equal to 0.7, 0.8, and 0.9, the curves of both cases intersect at Re between 60 and 80 and Cf^* between 0.18 and 0.183. While the ratio X values become 1 to 1.5, the curves of both cases intersect at Re between 80 and 100 and Cf^* between 0.19 and 0.23. The contrasts in skin friction ratio values appear to some extent. Therefore, it can be deduced that the skin friction is considered independent and the values of the skin friction do not depend

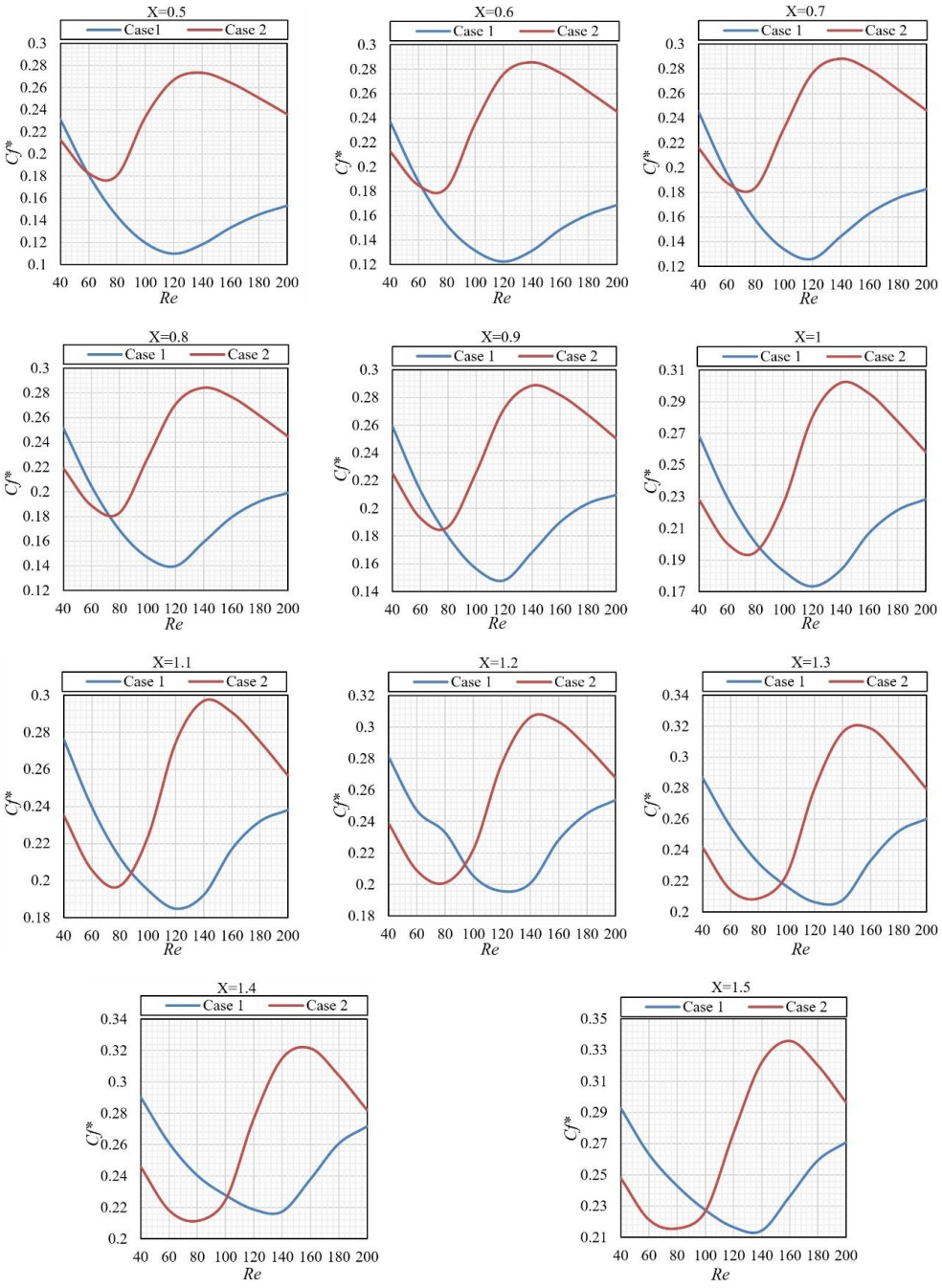

FIGURE 15. The variation in skin friction ration (*Cf**) with Reynolds number (Re) for different values of the ratio *X*

Source: own work.

on the Reynolds numbers and the horizontal distance between the bridge pier and the T-splitter plate.

From the numerical analysis and based on the same value of Cf^* for both cases, a theoretical equation comprises the Reynolds numbers values and the values of the ratio X are obtained. Figure 16 shows the trend of this theoretical equation. The equation has a nonlinear trend with the highest degree equal to a third degree:

$$\mathrm{Re} = A X^3 + B X^2 + C X + D. \tag{8}$$

The values of A, B, C and D are indicated in Figure 16.

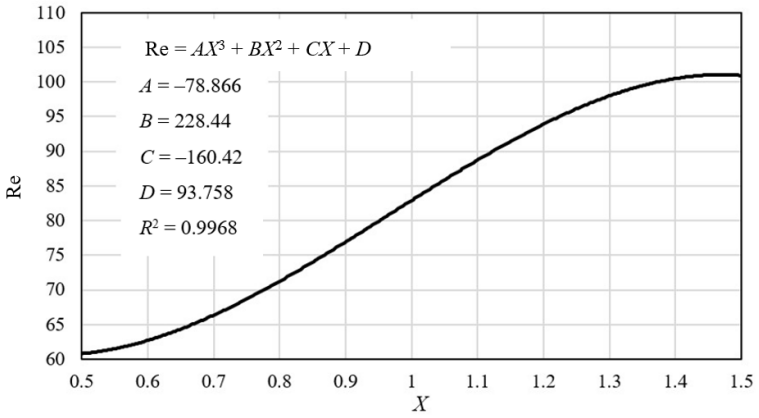

FIGURE 16. The relationship between Reynolds number (Re) and ratio X at same skin friction ratio (Cf^*) for both cases

Source: own work.

Conclusions

In this work, we considered a water-T-shaped splitter plate – water – bridge pier as a new idea in the fluid – structure problem. The influence of the Reynolds number or flow velocity on the hydrodynamic field around the hydraulic system which consists of the three parts (water, T-splitter plate, and pier) has been analysed. So, the following major points have been inferred from this hydraulic analysis. The values of the drag coefficient, lift coefficient, and skin friction coefficient of the pier alone are higher than the corresponding values when the splitter plate exists. The fundamental role of the splitter plate existence is to dominate the flow velocity field around the

pier. In addition, the splitter plate works as a tool to control the separation and dissipation processes at the front of the pier. Also, a nonlinear trend in relation is found among various values of the drag coefficient ratio with the ratio *X* regardless of the values of the Reynolds numbers. It is found that the skin friction coefficient has an inversely proportional relationship with the Reynolds number values and horizontal distance between the pier and the rear portion of the splitter plate. Moreover, the results show that there is no direct or measured relationship between the drag coefficient and lift coefficient due to the following reasons, the drag coefficient depends on the projection area which is perpendicular to the flow area while the lift coefficient depends on the area which is parallel to flow in spite of both coefficients depend on the flow velocity. The flow velocity gradient has a major impact on the values of the skin friction factor. Here, we must mention that the flow velocity gradient has direct proportionality with the shear stress, which is developed and grow at the skin of the pier and this will be reflected directly on the value of the skin friction factor.

References

Ahmed, R. A. (2015). Simulation of unsteady flow around a cylinder. *Wasit Journal of Engineering Sciences*, *3* (2), 28–49. https://doi.org/10.31185/ejuow.vol3.iss2.38

Bai, H. & Li, J. W. (2011). Numerical simulation of flow over a circular cylinder at low Reynolds number. *Advanced Materials Research*, *255–260*, 942–946. https://doi.org/10.4028/www.scientific.net/amr.255-260.942

Carberry, J., Sheridan, J. & Rockwell, D. (2005). Controlled oscillations of a cylinder: forces and wake modes. *Journal of Fluid Mechanics*, *538*, 31–69. https://doi.org/10.1017/s0022112005005197

Dahkil, S. F., Gabbar, T. A. & Jaber, D. K. (2014). Numerical study of the initial pressure and diameters ratio effect on the jet ejector performance. *Basrah Journal for Engineering Science*, *14* (1), 122–135.

Dennis, S. C. R. & Chang, G. Z. (1970). Numerical solutions for steady flow past a circular cylinder at Reynolds numbers up to 100. *Journal of Fluid Mechanics*, *42* (3), 471–489. https://doi.org/10.1017/s0022112070001428

Govardhan, R. & Williamson, C. H. K. (2000). Modes of vortex formation and frequency response of a freely vibrating cylinder. *Journal of Fluid Mechanics*, *420*, 85–130. https://doi.org/10.1017/s0022112000001233

Henderson, R. D. (1995). Details of the drag curve near the onset of vortex shedding. *Physics of Fluids*, *7* (9), 2102–2104. https://doi.org/10.1063/1.868459

Hu, Y. & Wang, J. (2013). The effects of attached flexible tail length on the flow structure of an oscillating cylinder. *Science China Physics, Mechanics and Astronomy*, *56* (2), 340–352. https://doi.org/10.1007/s11433-013-5014-8

Jabbar, T. A., Qasim, R. M. & Faisal, S. H. (2022b). Effect of T-shape splitter on the hydraulic response of the bridge pier. *U.P.B. Scientific Bulletin, Series D*, *84* (4), 263–280.

Jabbar, T., Qasim, R. & Mohammed, B. (2022a). The impact of the vane angle on the hydraulic behaviour around the cylinder. In *Proceedings of 2nd International Multi-Disciplinary Conference Theme: Integrated Sciences and Technologies*, IMDC-IST 2021, 7–9 September 2021, Sakarya, Turkey. https://doi.org/10.4108/eai.7-9-2021.2315298

Mehdi, H., Namdev, V., Kumar, P. & Tyagi, A. (2016). Numerical analysis of fluid flow around a circular cylinder at low Reynolds number. *IOSR Journal of Mechanical and Civil Engineering (IOSR-JMCE)*, *13* (3), 94–101.

Qasim, R. M. & Jabbar, T. A. (2021). An analytic study of the effect of a vane on the hydraulic field around a cylinder. *INCAS BULLETIN*, *13* (3), 123–139. https://doi.org/10.13111/2066-8201.2021.13.3.11

Qasim, R., Jabbar, T. & Abdulhussein, I. (2022a). Flow field simulation between angle vane and cylinder. In *Proceedings of 2nd International Multi-Disciplinary Conference Theme: Integrated Sciences and Technologies*, IMDC-IST 2021, 7–9 September 2021, Sakarya, Turkey. https://doi.org/10.4108/eai.7-9-2021.2315181

Qasim, R. M., Jabbar, T .A. & Faisal, S. H. (2022b). Effect of the curved vane on the hydraulic response of the bridge pier. *Ocean Systems Engineering*, *12* (3), 335–358. https://doi.org/10.12989/ose.2022.12.3.335

Qasim, R. M., Faisal, S. H. & Jabbar, T. A. (2022c). Impact of T-splitter on the laminar flow field around cylinder pier. *Advances in Science and Technology Research Journal*, *16* (5), 202–215. https://doi.org/10.12913/22998624/154795

Rajani, B. N., Kandasamy, A. & Majumdar, S. (2009). Numerical simulation of laminar flow past a circular cylinder. *Applied Mathematical Modelling*, *33* (3), 1228–1247. https://doi.org/10.1016/j.apm.2008.01.017

Sharma, B. & Barman, R. N. (2020). Steady laminar flow past a slotted circular cylinder. *Physics of Fluids*, *32* (7), 073605. https://doi.org/10.1063/5.0007958

Shen, P., Lin, L., Wei, Y., Dou, H. & Tu, C. (2019). Vortex shedding characteristics around a circular cylinder with flexible film. *European Journal of Mechanics – B/Fluids*, *77*, 201–210. https://doi.org/10.1016/j.euromechflu.2019.05.008

Shukla, S., Govardhan, R. N. & Arakeri, J. H. (2013). Dynamics of a flexible splitter plate in the wake of a circular cylinder. *Journal of Fluids and Structures*, *41*, 127–134. https://doi.org/10.1016/j.jfluidstructs.2013.03.002

Summary

Simulation of laminar flow passing through a T-splitter plate and bridge pier. The present analysis focuses on the investigation of the two-dimensional flow passing a bridge pier nearby a splitter plate in different regimes of a laminar flow. The splitter plate is T-shaped and two different cases have been studied based on the form of the splitter plate

relative to the bridge pier. The analysis is implemented for steady and incompressible water flow in an open channel. The current study deals with velocity vectors, drag coefficients, lift coefficients, and skin friction. The analysis of the velocity vector gave a good indicator about the separation process and dissipation, which occurs at the splitter plate before the occurrence of these processes at the front face of the pier, especially the flow separation process. Moreover, the velocity vector gave a good image about the flow direction at two regions, the first region is located between the rear portion of the splitter plate and the frontal face of the pier, while the second region is the wake region, which is located at the downstream of the pier. Negative drag coefficient, lift coefficient, and skin friction coefficient values are obtained from the analysis. This happens due to the existence of the splitter plate that leads to the reduction of these values.

Scientific Review Engineering and Environmental Sciences (2023), 32 (2), 155–174

Sci. Rev. Eng. Env. Sci. (2023), 32 (2) https://srees.sggw.edu.pl

ISSN 1732-9353 (suspended) eISSN 2543-7496 DOI 10.22630/srees.4790

Received: 17.02.2023
Accepted: 05.04.2023

Heni FITRIANI✉ https://orcid.org/0000-0003-1530-1271

Muhammad Agung KURNIAWAN

Febrian HADINATA

Universitas Sriwijaya, Civil Engineering Department, Indonesia

Analysis of tariff adjustment for clean water usage

Keywords: tariff, investment, water, scenario

Introduction

The human need for water never decreases as it continues to grow over time and together with an increasing population. The availability of clean water is one of the important elements that must be fulfilled for daily human needs. The high population growth rate results in a growing demand for clean water (Abdul & Sharma, 2007). The urgency for clean water is also impacted by the number of residents, the number of house connections and the number of people per house (Firat, Yurdusev & Turan, 2009). The provision of clean water is of particular concern, especially for local water supply companies, called in Indonesian *Perusahaan Daerah Air Minum* (PDAM). Meeting the water needs for the community has increased, but the quantity of water available with adequate quality for the community is being increasingly limited. An increase in the number of customers should ideally be accompanied by an increase in services in the distribution of clean water to meet the daily needs of

✉heni.fitriani@unsri.ac.id

customers. However, the reality shows that the community still complains about the services provided by the PDAM because the water distribution does not meet the expectations of the community and has not reached all parts of the area.

As a clean water service provider company in Palembang City, PDAM Tirta Musi, has not been able to meet all of the community's clean water needs. The current service coverage is around 80%, which means that about 20% of the people of Palembang City do not have access to clean water (Tirta Musi, 2020). Although there is the increasing demand of customers of about 97.5%, it is known that thousands of prospective customers queue each year that cannot be processed (Tirta Musi, 2021). The main problem is that the production capacity is already in deficit so if additional customers are added, the deficit of water capacity will be even greater. Another problem is that the population is increasing every year, so the impact on the percentage of service coverage is getting smaller. The above-mentioned problems can be overcome by developing the water stock system, in Indonesian called *Sistem Penyediaan Air Minum* (SPAM), including increasing production capacity, expanding the pipeline network, reducing water loss, etc. (Bello et al., 2019). Water stock system development requires large funds for investment (Massarutto, 2007; Hukka & Katko, 2015; Aswar, 2019). A bank loan is the investment funding scheme chosen by the company loan. This scheme was taken to avoid the risks of investing in water supply for a long duration (above 30 years), such as concession schemes and other agreement schemes (Pribadi & Pangeran, 2015).

Water rates are an important tool for controlling the supply and demand of scarce water resources. Adjusting water rates is a crucial element in the transition to a market economy (Pinto, Tchadie, Neto & Khan, 2018; Pinto, de Carvalho & Marques, 2021). This reform leads to the utility's long-term, sustainable growth, which is based on customer demand and proper financing of all utility expenditures. Tariff reform entails significant changes in water regulation, the business environment, financial management strategies, subsidies, and public relations, in addition to the formulas and levels of tariffs (Babak & Byrne, 2002). Utilities are evaluating whether the current tariff structure is responsive to their current demands and whether it allows charging consumers fairly for their fair share of costs in light of the emerging trends and issues surrounding the tariff setting process. An efficient rate structure's goal is to maximize the utility's pricing objectives, which support the fundamental pricing concepts. After the necessary revenue has been determined, costs are distributed among the various water customers, and after that, rates are created to reflect the price of providing water service.

Reforming the current water pricing practices and tariff structures is crucial, especially when aiming to improve the water supply services (Dinar, Pochat

& Albiac-Murillo, 2015). Governments must consider that managing and operating services involve associated costs when delivering clean water services to the community (Pinto et al., 2018). As the level of profit has been set by Indonesian regulation – Permendagri No 71 of 2016 and not limited by predetermined tariff, various alternatives can be used. When choosing a tariff structure that responds to the goals of the utility and its community, there are significant obstacles in water pricing and tariff design (Whittington, 2003) especially based on the local context. Many previous researchers have discussed tariff adjustment (Juhery & Indryani, 2008; Indayani & Sunarto, 2013) the analysis of which only focuses on the full cost recovery (*FCR*) value – fixed charge in tariff formation (García-Valiñas & Picazo-Tadeo, 2015). According to Nurhotijah and Situmorang (2017), and Supriatini, Jumiari, Agihidayantari and Dewi (2017), the determination of water tariffs is based on the *FCR* method, namely calculating production costs obtained from the total expenditure per cubic meter of water. Furthermore, Artama (2018) provides an example of the analysis of tariff adjustment by fulfilling the *FCR* as well, but also analyzing the feasibility of the investment made financially. Previous research on tariff adjustments only focused on the fulfilment of the *FCR* without analyzing different alternatives yet. There is no optimal strategy that can be advised to single sector, according to these studies that analyze water pricing success across nations. Therefore, this study aims to evaluate the tariff adjustment of water supply company under different scenarios. This paper illustrated that tariff determination was carried out with several scenarios of increasing tariffs. This study is expected to provide a framework and lesson regarding tariff adjustment under different alternatives as well as offering cases of the achievement and failure of pricing policies in a local water company.

Material and methods

This research begins with a background that describes the condition of the availability of clean water in the city of Palembang and the condition of the PDAM Tirta Musi Palembang company. Problems have been found under these conditions. Furthermore, a literature study related to the problems discussed was carried out by identifying library needs, looking for references from previous studies, as well as for government regulations that regulate the provisions in the analysis of this research.

The analysis of the financial condition of the existing tariff is calculated by projecting the income and costs incurred as a result of the investment. Existing tariffs are tested to determine whether the *FCR* is compiled or not. The tariff adjustment

scenario is carried out by the *FCR* test, net profit and feasibility analysis. If it is *FCR*, then proceed to the feasibility analysis, if not then it is recalculated so that it is *FCR*. It refers to recovering all costs from sales in order to meet operational requirements and can be expressed numerically:

$$FCR = AWT > BC. \tag{1}$$

In Eq. (1), *AWT* is an average water tariff, *BC* is a basic cost is calculated based on the overall cost per cubic meter. Furthermore, if the calculation is found to not be feasible, then the tariff adjustment analysis is carried out to produce the feasibility of the investment. The investment is declared financially feasible if $NPV > 0$ and $IRR > 10.9\%$ as the minimum acceptable rate of return value (*MARR*). The Eqs (1) and (2) were used in the discussed method.

$$NPV = \sum_{t=0}^{n} \frac{A_t}{(1+i)^t} - IO. \tag{2}$$

$$IRR = i_1 + \left[\frac{NPV1}{NPV1 - NPV2} \right] (i_2 - i_1). \tag{3}$$

In Eqs (2) and (3), A_t is an annual cash flow after tax in the annual period, i is a discount rate, t is an annual period, *IO* is an initial outlay. Tariff adjustments were made in several scenarios. The tariff adjustment scenario can be seen in Table 1.

TABLE 1. Tariff adjustment scenario

Scenario type*	Increase	Concession period	Information
First scenario	varies	2 years	Achieving *FCR* and financially viable
Second scenario	8%	2 years	Annual inflation, which is 4%
Third scenario	varies	4, 6, 8, 10 years	The *FCR* lasts for a long time and is financially viable

*Description in the text.

Source: own work.

In the first scenario, it is assumed that the tariff increase is carried out every 2 years and the amount of the increase in tariffs varies. The amount of the rate increase is obtained by trial and error until the projected *FCR* value can be met. The determination of the percentage increase is made to a minimum with the shortest increase

time. This assumption is taken because there is hope that a small tariff increase will not burden the community in paying the clean water bill every month. The increase period is assumed to be every 2 years based on the shortest increase period allowed by the adequate Indonesian regulation (Permendagri). This shortest period is carried out to compensate for the small percentage increase in tariffs. If the amount of the increase can meet the *FCR* value, then a financial feasibility analysis is calculated. If the results are feasible, then the tariff can be used.

The second scenario assumes that the existing tariff increases by 8% every 2 years. In this scenario, it is assumed that the increase in water tariffs is equal to the inflation rate. The increase in costs due to inflation is assumed to be 4% per year, so with a period of increase of 2 years, the increase is assumed to be 8% (Bank Indonesia, 2022). The average inflation rate over the previous 10 years provides the basis for the assumption of a rise in inflation each year. Expenses are projected to increase proportionately to inflation. In this scenario, it is tested whether the increase in water tariff equal to the inflation rate can offset the increase in costs, so that it can still meet the *FCR* value. This scenario also analyses the feasibility of investments made after the tariff adjustment.

The third scenario assumes that the amount of increase in the existing water tariff varies. The increment period is assumed to be every 4, 6, 8 and 10 years. The amount of the tariff is carried out by trial and error until it can maintain the *FCR* rate for a period of 4, 6, 8 and 10 years. With a long period of increase, the magnitude of the increase in tariffs will be greater. If the *FCR* value has been met, then the investment feasibility analysis is calculated after the tariff adjustment is made. If the results are declared feasible then the amount of the increase can be used; if not feasible, then try and error is carried out again until the results of the investment feasibility are financially feasible. This scenario is carried out to accommodate the possibility if the increase period cannot be carried out with the shortest period, namely 2 years. This is based on the company's previous experience that the current tariff has not been adjusted for the last 10 years. The previous tariff adjustment was also carried out after 5 years, namely after the water tariff set in 2006 was adjusted to the water tariff in 2011. The increase period of 4, 6, 8 and 10 years was chosen to facilitate the calculation process which is considered to represent tariff adjustments for long periods of increase. The 3 scenarios generate mixed water revenues. This has various impacts on the fulfillment of *FCR*, profit and loss and investment feasibility. This scenario depicts the determination of the amount of the increase in tariffs for the period of the increase taken.

Fitriani, H., Kurniawan, M. A., Hadinata, F. (2023). Analysis of tariff adjustment for clean water usage. *Sci. Rev. Eng. Env. Sci.*, *32* (2), 155–174. DOI 10.22630/srees.4790

Results and discussion

The PDAM Tirta Musi has several infrastructure buildings scattered throughout the service area in running its business. The intake building has functions to take raw water from its source, namely the Musi River located in 5 sites, including: Intake Ogan 1, Ogan 2, Karang Anyar, 1 Ilir and Borang. The raw water taken at the intake is sent to the clean water treatment plant (IPA) located in 7 locations, including: IPA Ogan 1, Ogan 2, Rambutan, Karang Anyar, Polygon, 3 Ilir and Borang. Clean water that has been treated is then sent to customers through distribution pipes. In drainage areas that are far from the IPA, a booster building is needed to temporarily accommodate and re-pump water to the distribution network in order to increase the drainage pressure. As many as 7 boosters are spread in the service area, including: Kertapati, Plaju, Km. 4, Punti Kayu, Alang-alang Lebar, Sako Kenten and Kalidoni. Intake, IPA and booster location maps can be seen in Figure 1.

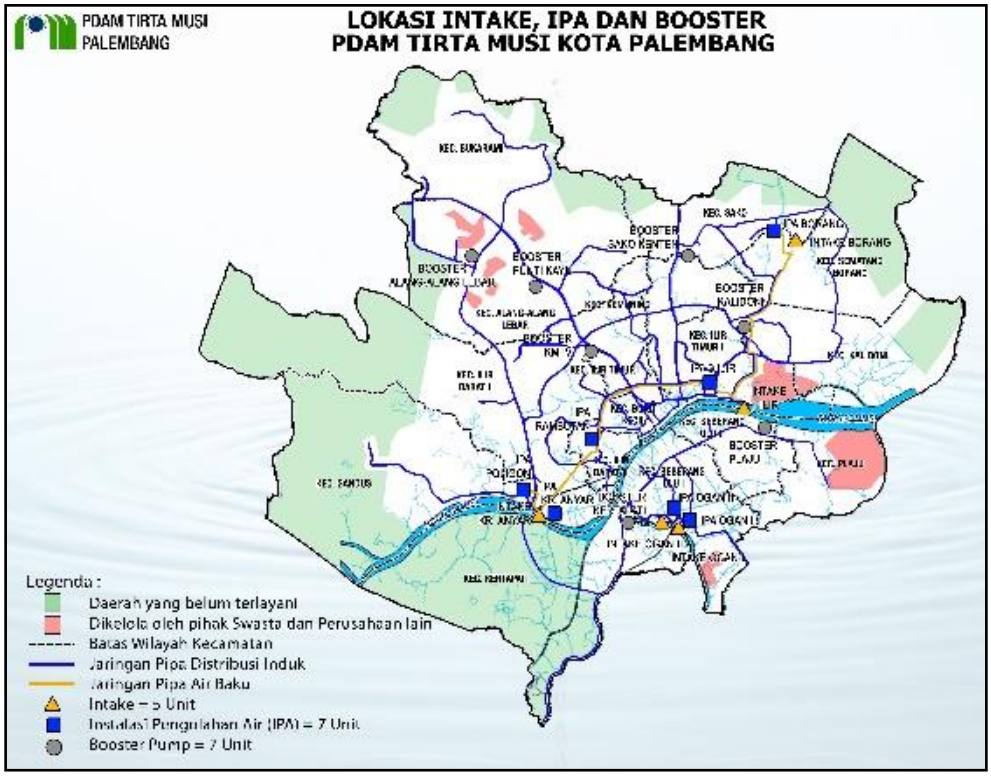

FIGURE 1. Intake, IPA and booster location map
Source: PDAM Tirta Musi Palembang.

The infrastructure buildings have not been able to meet the clean water needs optimally as shown in Figure 1. Production capacity is still experiencing a deficit and the service coverage has not yet reached 100%. Therefore, the company makes investments by preparing several activity program plans, including optimization of existing production, increased production capacity, replacement and addition of new pipelines, decreased water loss and support.

Existing financial analysis

This analysis is carried out on the financial condition prior to the tariff adjustment. The analysis was conducted to determine the impact of the absence of tariff adjustments for the next year on the company's financial performance. The existing tariff, which is still being used to this day, has been set since 2011, so that it has not been adjusted for 11 years. This analysis yields important information about whether tariff adjustments should be made or not. The impacts seen at this stage include the *FCR* and profit and loss generated by the company. Based on amendment Permendagri No 21 of 2020, *FCR* indicators need to be reviewed to determine whether water sales have been able to cover operational needs and the development of drinking water services or not. To obtain this, it is necessary to calculate the projected income and expenses.

Income analysis

Income can be divided into 2 types, namely water income and non-water income. Water revenue is income generated from the sale of water to customers, while non-water revenue is income generated outside of the sale of water that is tied to the PDAM business. Water revenues include water tariffs, fixed charges to customers, water meter maintenance and other water revenues other than piping. Non-water revenues include income from new connection fees, laboratory water inspections, reconnection, fines, replacement of damaged meters, replacement of parcel pipes, and other non-water revenues. Tariff income is obtained by multiplying the number of customers by the respective usage cubication and the water tariff charged. The cubication used uses data on water consumption of existing customers in 2020 as seen in Table 2. Water consumption in the coming year is assumed to have no change in value. The water tariff does not consist of a single value, but is divided into several tariff values that are formed according to the customer category and the volume of usage cubication. The arrangement of

these various tariff values is referred to as the water tariff structure as presented in Table 3. The water tariff structure was formed to accommodate cross subsidies between tariffs for low-income, high-income customers and business customers. In addition, it is subdivided according to the progressive consumption volume of each customer category.

TABLE 2. Existing water consumption data

Customer category	Number of customers	Water consumption [m^3]
IA/General Social	31	35 007
IB/Social	2 203	1 685 603
Very Simple IC/RT	1 277	477 438
Special Social I/D B	624	651 299
Government Hospital I/E	5	620 542
II/A Old Village RT	102 923	32 845 681
II/B Medium RT / Office	151 523	50 861 891
II/C TNI / POLRI Office	602	1 78 040
ll/D Small Business	11 841	5 420 534
ll/E RT and Luxury Boarding House	5 082	2 822 557
III/A Small Commerce	21 339	6 530 937
III/B Big Commerce A	3 337	3 615 130
III/C Big Commerce B	49	630 026
Special Commerce	2	64 813
Water Terminal	–	–
Total amount	300 838	107 739 498

Source: own work.

The calculation of non-water revenue is simplified into 3 parts, namely new connection revenue, other non-water revenue and other income. Revenue for new connections is obtained from customer projections that are adjusted to the customer category multiplied by the tariff for new connections. The percentage of other non-water revenues to water revenues and other revenues to water revenues are used as assumptions for the projection. The percentage assumption is multiplied by the projected water revenue in the projected year. The revenue projections are made under the assumption that there won't be any changes to the tariff, but that there will be more connections overall. The pattern of connection growth over previous 5 years reveals a rise in the number of connections.

The revenue projection is depicted in Figure 2, illustrating that the income increased from 2020 to 2033. However, it decreased slightly in 2034 and was

TABLE 3. Tariff structure

Customer category	Value	Customer category	Value
General Social / IA	×	TNI / POLRI / II C	×
0–10 m^3	605	0–10 m^3	2 365
11–20 m^3	605	11–20 m^3	3 320
21–30 m^3	605	21–30 m^3	3 630
> 30 m^3	605	> 30 m^3	4 840
Special Social A / IB	×	Small business / II D	×
0–10 m^3	800	0–10 m^3	3 630
11–20 m^3	1 000	11–20 m^3	4 235
21–30 m^3	1 340	21–30 m^3	5 740
> 30 m^3	1 600	> 30 m^3	6 645
Special Social B / ID	×	RT and Kos Luxury / II E	×
0–10 m^3	1 000	0–10 m^3	4 235
11–20 m^3	1 825	11–20 m^3	4 840
21–30 m^3	2 420	21–30 m^3	6 050
> 30 m^3	3 025	> 30 m^3	7 550
Very simple RT / IC	×	Small commerce / III A	×
0–10 m^3	935	0–10 M3	4 530
11–20 m^3	1 510	11–20 m3	5 440
21–30 m^3	1 815	21–30 m3	6 050
> 30 m^3	2 420	> 30 m3	9 065
Government hospital / IE	×	Big commerce A / III B	×
0–10 m^3	1 340	0–10 m^3	5 285
11–20 m^3	2 155	11–20 m^3	5 740
21–30 m^3	3 025	21–30 m^3	6 645
> 30 m^3	3 630	> 30 m^3	10 420
Old Village RT / II A	×	Big commerce B / III C	×
0–10 m^3	1 595	0–10 m^3	5 740
11–20 m^3	2 420	11–20 m^3	6 050
21–30 m^3	3 025	21–30 m^3	7 550
> 30 m^3	3 630	> 30 m^3	10 880
Medium RT / Office / II B	×	Special commerce	×
0–10 m^3	1 845	0–10 m^3	18 125
11–20 m^3	2 725	11–20 m^3	18 125
21–30 m^3	3 320	21–30 m^3	18 125
> 30 m^3	4 235	> 30 m^3	18 125
×	×	Water terminal	18 125

Source: own work.

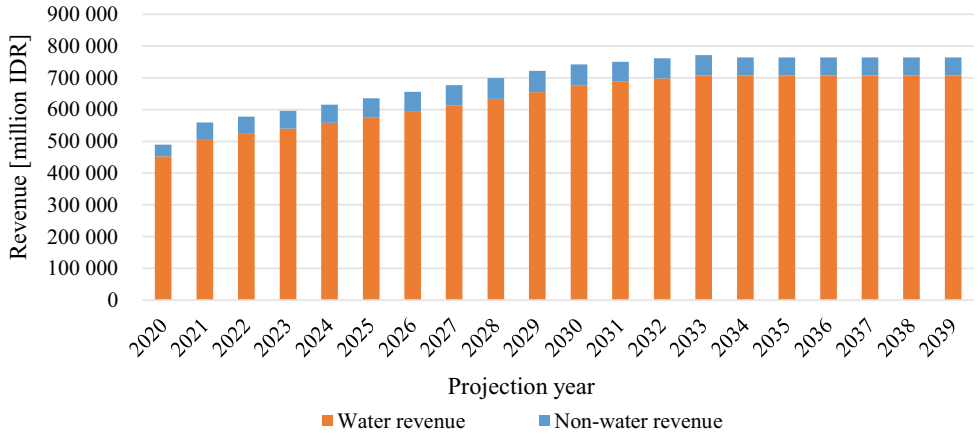

FIGURE 2. Revenue projection (1 USD = 15,000 IDR)
Source: own work.

consistent until 2039. It is also seen that water revenues have a dominant portion in contributing to company revenues. This means that the effect of water tariffs is very large on the company's overall revenue.

Expense cost analysis

The cost components include the operating and maintenance costs, depreciation or amortization, loan interest and other costs. Operation and maintenance costs are the entire series of costs of running a business from water sources, production to distribution. Operation and maintenance costs include personnel costs, electricity/fuel, chemicals, raw water, administration and general and maintenance costs. Depreciation and amortization costs are all depreciation expenses of assets that are in shape or form. Borrowing interest costs are interest costs generated from loans to banks including commitment fees, penalties and other financial costs related to loans. Other costs are unexpected costs that cannot be separated from the company's business.

These costs are assumed to increase due the 4% inflation. Depreciation costs are projected using the straight-line method with a plan life of 20 years, so that the projected expenses are carried out from 2020 to 2039. The projected expenses can be seen in Figure 3 – the highest expenses are personnel costs, while the lowest expenses are other costs. Personnel costs have the highest rate of increase among other costs. Expenses have increased every year. If the total expenses in 2020 are 327,600,842,766 IDR and in 2039 increased to 1,076,940,135,648 IDR.

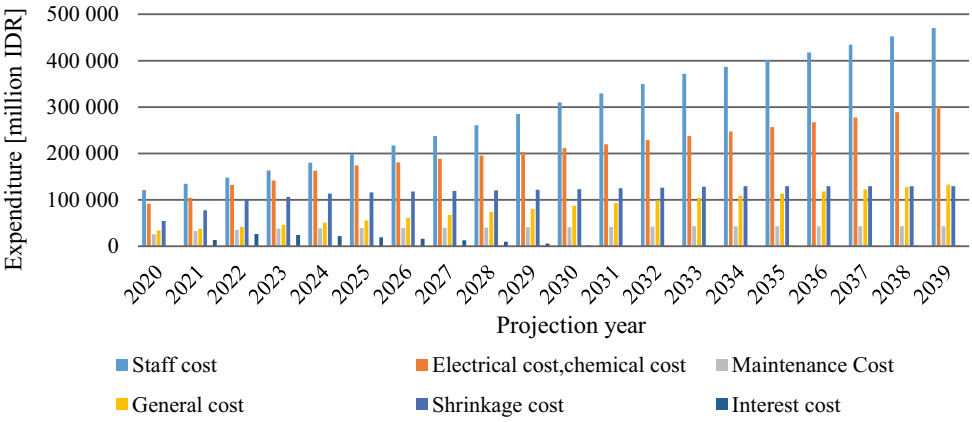

FIGURE 3. Expenditure projection (1 USD = 15,000 IDR)
Source: own work.

Full cost recovery analysis and existing profit and loss

The calculation of the full cost recovery (*FCR*) begins with calculating the cost of goods sold (COGS), which is the sum of all operational costs and development costs. These costs include personnel costs, electricity/fuel, chemicals, raw water, maintenance, administration and general expenses, other costs, depreciation costs and interest costs. The total cost is then divided by the volume of distributed water which has been reduced by the volume of water loss. The volume of water loss is assumed to be 20% according to the actual data. The result is the rupiah (IDR) value per cubic meter called the basic cost. Furthermore, it is essential to calculate the average rate by dividing the tariff revenue by the cubication volume sold, resulting in a per cubic rupiah value. The *FCR* value can be met if the average water tariff is greater than the basic cost. Figure 4 shows that the average water tariff chart trend is stagnant, while the basic cost chart trend is increasing every year. This makes the gap between the average water tariff and the basic cost each year bigger. The *FCR* value fulfilled can only last until 2022, while from 2023 onwards the *FCR* value cannot be fulfilled again. This means that the company only benefits from sales until 2022, while from 2023 the company suffers a loss for every cubication of water sold and the losses increase in the following year.

The calculation of net profit begins by adding up the total revenue, both water and non-water revenues. These costs include operating costs, depreciation, interest and taxes. Net profit is obtained by subtracting the total income by the total

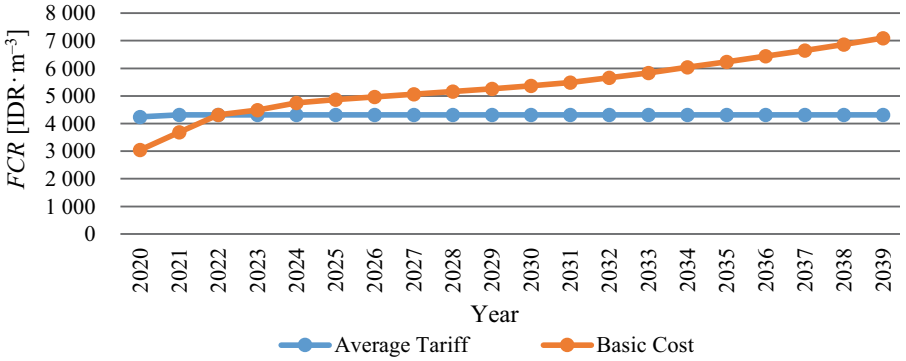

FIGURE 4. The full cost recovery (*FCR*) value projection (1 USD = 15,000 IDR)
Source: own work.

expenses. Figure 5 presented the profit and loss projection. This indicated the net profit projected to decrease every year until 2027. Starting from 2028 the company cannot generate profits and suffer losses until the projected year 2039.

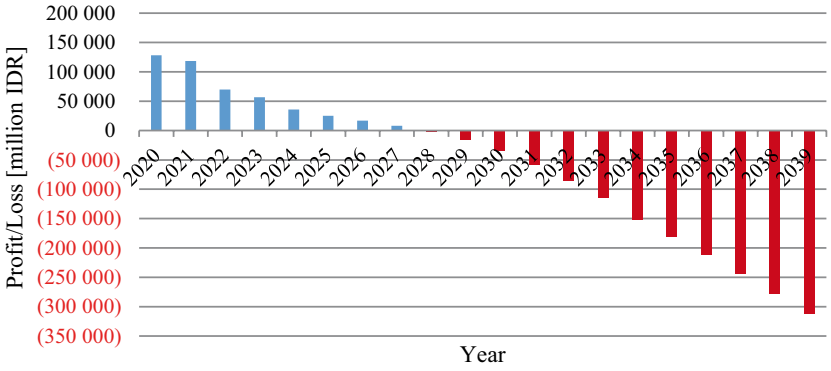

FIGURE 5. Profit and loss projection (1 USD = 15,000 IDR)
Source: own work.

Based on the results depicted in Figure 5, it shows that there is urgency to develop tariff adjustments which is expected to be able to balance the company's income against the company's expenses as well as cover operational costs. Tariff adjustment in this study was carried out in several scenarios. The scenario results inform the impact that occurs after the tariff adjustment.

Price adjustment scenario analysis

Several possible scenarios are developed to make tariff adjustments in order to analyze the full cost recovery (*FCR*), the company's profit and loss projections. In addition, the financial feasibility of the investment is also reviewed if the *FCR* has been fulfilled. The tariff scenario is declared financially feasible if $NPV > 0$ and $IRR > 10.9\%$ as the *MARR* value. The scenario is carried out by increasing the existing tariff structure and is projected for a certain period of increase according to the assumptions made for each scenario. The principle in developing this scenario is that the amount of increase is chosen as small as possible but still meets the *FCR* and is financially feasible. The scenario for the tariff adjustment carried out is as follows:

First scenario rate adjustment

The first scenario assumes that the tariff increase is carried out to achieve the *FCR* value. The existing tariff structure is increased in such a way by means of trial and error calculations, so that the average water tariff can cover the basic cost. In addition to the tariff structure, administrative costs and new connection costs are projected to increase proportionally to the increase in the tariff structure. This scenario is projected to increase the tariff every 2 years. The increase in tariffs in the first scenario also causes the average water tariff to increase. The average water tariff in 2022, which was originally 4,313 *IDR*, has changed to 4,528 IDR, so that the average water tariff exceeds the basic cost in 2022. The projection of the average water tariff can be seen in the projected *FCR* value as shown in Figure 6. Figure 6 illustrates that the increase in tariffs in this scenario can change the average water tariff to increase compared to the average water tariff under the conditions of the existing tariff structure. The graph of the average water tariff which was originally in 2023 and onwards is below the basic cost graph has changed to above the base cost graph. This means that with the increase in tariffs carried out in the first scenario, the *FCR* value can be fulfilled.

The calculation of the financial feasibility of an investment requires a net cash flow value. Net cash flow is obtained by subtracting cash inflows with cash outflows over 20 years. The projected present value of the benefit (*PVB*) can be seen in Table 4.

Table 4 shows that the *NPV* value generated in the first scenario is –486,291,930,693 IDR. This means that the first scenario is not financially

TABLE 4. Projected present value of benefit (*PVB*) projection

Year	Investment value [million IDR]	Net cash flow [million IDR]	Present value of benefits [million IDR]
1	458 832	11 872	10 705
2	455 010	35 715	29 040
3	135 356	40 789	29 905
4	143 728	36 877	24 380
5	42 888	138 331	82 463
6	39 990	132 250	71 089
7	27 232	166 174	80 546
8	28.306	157 718	68 933
9	29 458	173 578	68 409
10	30 622	163 429	58 078
11	31 851	205 700	65 915
12	33 117	215 814	62 359
13	34 459	235 418	61 338
14	35 815	216 794	50 934
15		279 389	59 188
16		257 130	49 119
17		292 572	50 396
18		268 499	41 704
19		297 200	41 624
20		271 164	34 245
Total	1 526 664		1 040 372
NPV = 1 040 372 – 1 526 664 = –486 291			

Note: 1 USD = 15,000 IDR.

Source: own work.

TABLE 5. First scenario rate increase change

Year	% Beginning	% Change
2022	5	8
2024	9	12
2026	5	8
2028	4	7
2030	4	7
2032	5	8
2034	7	10
2036	7	10
2038	6	9

Source: own work.

feasible after $NPV < 0$. Therefore, the tariff increase in the first scenario is recalculated. After the trial and error, the first scenario can be feasible after the rate increase changes as shown in Table 5. Changes in the tariff increase in the first scenario make changes to the fulfillment of the *FCR* value. With the change in the rate increase as shown in Table 5, the investment can be declared feasible after the *NPV* value is 31,107,373,716 IDR and the resulting *IRR* value is 11.095%.

Second scenario tariff adjustment

The tariff adjustment in the second scenario is assumed to increase in tariffs equal to the increase in the inflation rate, so it is expected that the increase of income is equal to the rate of increase in costs incurred. In addition to tariffs, administrative costs and new connection fees are assumed to increase at the rate of inflation. This scenario was taken because the existing tariff conditions can still maintain the *FCR* until 2022, but because revenues are stagnant and costs continue to increase due to inflation. This scenario tests whether the *FCR* can be maintained or not, if the rate of increase in tariffs is the same as the inflation rate. Net income for the 2 periods of increase in general experienced an increase. However, net profit has decreased from 2020 to 2023 with net profit not reaching 100,000,000,000 IDR, but in 2024 and beyond net profit has increased. The feasibility calculation in the second scenario produces an *NPV* value of –99,361,910,101 IDR. The *IRR* value is 10.25%, so the investment is declared financially unfeasible. The results of the analysis in the second scenario show that an increase in tariffs to the level of inflation can result in water tariffs that can meet the *FCR* value. However, this rate increase cannot result in the feasibility of the investment being made. Therefore, tariff adjustment in the second scenario is not recommended for use.

Third scenario tariff adjustment

The tariff adjustment in the third scenario is carried out to determine the amount of tariff increase that can be used if the tariff increase period is longer. In this scenario, it is assumed that the tariff increase period is carried out every 4, 6, 8 and 10 years. The amount of the tariff is obtained by trial and error so that the tariff can maintain its *FCR* value for each period of increase. The first tariff increase is assumed to be in 2022. In addition to the water tariff, it is also assumed that an increase in monthly administrative costs/expenses and the cost of new connections is assumed. The amount and period of increase is carried out in the same year as the tariff increase. Based on the results of trial and error calculations, the amount of tariff increase is obtained so that it reaches the *FCR* value for each period of increase. The amount of the tariff increases for the four-, six-, eight- and ten-year tariff increase periods is 13%, 19%, 25% and 29%, respectively. Figure 6 shows that a longer period of increase has a higher average water tariff at the start of the increase, so it can maintain the average water tariff graph above the basic cost graph longer. On the other hand, a shorter increase period results in a relatively smaller average water tariff.

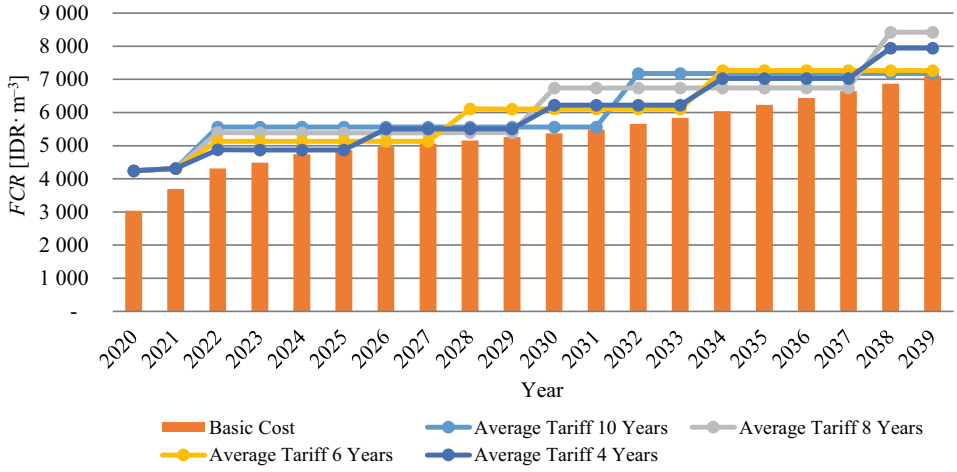

FIGURE 6. The full cost recovery (*FCR*) value projection (1 USD = 15,000 IDR)
Source: own work.

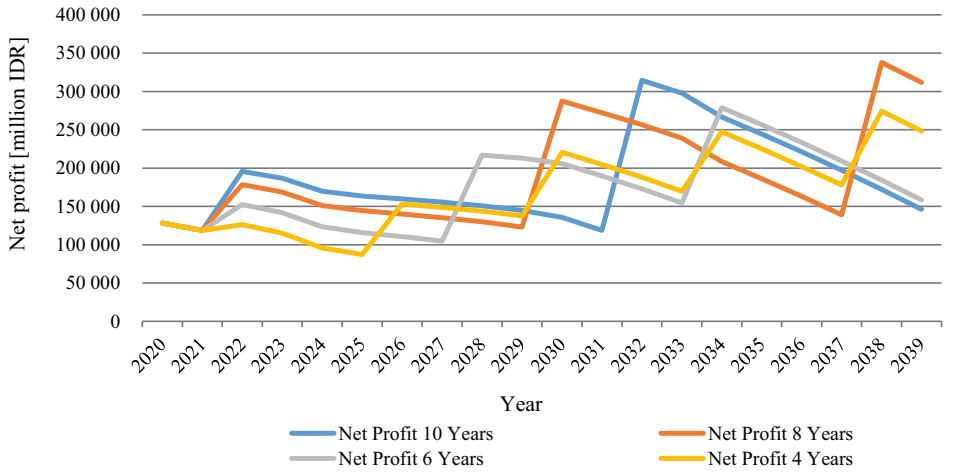

FIGURE 7. Net profit projection (1 USD = 15,000 IDR)
Source: own work.

In Figures 6 and 7, the graph increased sharply in a year where tariffs were increasing. However, in the following year the net profit graph decreased until the tariffs increased again. This means that when there is no tariff adjustment, net profit growth decreases. Based on the analysis of the financial feasibility of investing, the third scenario results in the *NPV* value for the period of increasing 4, 6, 8, and 10 years, respectively, amounting to –248,029,269,288 IDR, –181,682,498,528 IDR,

–70,554,971,185 IDR and –56,008,269,866 IDR. The *NPV* value is still below 0, so with the increase in tariffs carried out in this scenario, the investment is declared unfeasible. Figure 7 shows that the net profit is significantly impacted by the water tariff adjustment. Net profit will decline in the absence of a tariff rise.

The results of the developed tariff adjustment scenario show that a small percentage increase in tariffs can be made if the increase period is relatively short. On the other hand, a large percentage increase in tariffs can last for a relatively long time. An increase in tariffs with an increase equivalent to inflation can only meet the *FCR* value, but is not feasible in the analysis of financial feasibility of investment. The developed scenario also shows that the increase in tariffs cannot be made only to balance the costs that must be incurred, but it must produce a reasonable profit, so that the increase in tariffs designed can be declared feasible for the investment.

Based on the above considerations, the first scenario gives the most ideal result to be applied as a new water tariff. The magnitude of the increase in the first scenario has a relatively small percentage, so customers are expected not to object to the increase made. In terms of the trend of net profit growth, it provides a better trend with gradual net profit growth, so that the company's financial performance appears to be growing consistently. In addition, the investment returns are relatively similar as in the third scenario.

Conclusions

This paper has presented that tariff determination was carried out with several scenarios of increasing tariffs. Based on the results of the analysis carried out on the water demand and the adjustment of water usage tariffs at PDAM Tirta Musi Palembang, tariff adjustment scenarios were carried out with variations in the percentage increase in tariffs and the period of the increase in tariffs. This scenario showed that the increase in tariffs will have an impact on increasing the company's income. The small percentage increase in tariffs must be balanced with a short increase period, so that the *FCR* value can still be met. On the other hand, with a large percentage increase in tariffs, *FCR* compliance can last for a relatively longer period of growth. The most ideal scenario of the 3 developed ones is the first scenario. The first scenario resulted in a relatively smaller increase in tariffs but was able to meet the *FCR*. In addition, the net profit growth trend generated by the first scenario increases gradually. To conclude, this study has provided a framework and lesson regarding tariff adjustment under different alternatives as well as offering cases of the achievement and failure of pricing policies in a local water company.

References

Abdul, S. & Sharma, R. N. (2007). Water consumption patterns in domestic households in major cities. *Economic and Political Weekly*, *42* (23), 2190–2197.

Aswar, K. (2019). Financial performance of local government in Indonesia. *European Journal of Business and Management Research*, *4* (6), 1–6.

Artama, I. P. (2018). Analysis of Determination of Drinking Water Tariffs for Lamongan District Water Supply Based on Full Cost Recovery Principles. *Journal of Civil Engineering*, *33* (1), 10–19.

Babak, A. & Byrne, V. (2002). *Tariff reform in the municipal water supply: first expert workshop tariff rules: cost identification, cost allocation and rate structuring – possibilities for Ukraine*. Paris: Planning and Development Collaborative International.

Bank Indonesia (2022). *Target Nilai Inflasi Periode Tahun 2001–2021*. Retrieved from: https://www.bi.go.id/id/statistik/indikator/target-inflasi.aspx [accessed 06.06.2022].

Bello, O., Abu-Mahfouz, A. M., Hamam, Y., Page, P. R., Adedeji, K. B. & Piller, O. (2019). Solving management problems in water distribution networks: a survey of approaches and mathematical models. *Water*, *11* (3), 562.

Dinar, A., Pochat, V. & Albiac-Murillo, J. (2015). *Water pricing experiences and innovations*. Berlin: Springer.

Firat, M., Yurdusev, M. A. & Turan, M. E. (2009). Evaluation of artificial neural network techniques for municipal water consumption modeling. *Water Resources Management*, *23* (4), 617–632.

García-Valiñas, M. A. & Picazo-Tadeo, A. J. (2015). Introduction to reforming water tariffs: experiences and reforms. *Utilities Policy*, *34*, 34–35.

Hukka, J. J. & Katko, T. S. (2015). Appropriate pricing policy needed worldwide for improving water services infrastructure. *Journal – American Water Works Association*, *107* (1), E37–E46.

Indayani, I. P. & Sunarto, S. (2013). Analisis Kelayakan Tarif Air Berdasarkan Peraturan Menteri Dalam Negeri Nomer 23 Tahun 2006 Data Tahun 2009 s.d 2012 Study Kasus di PDAM Tirta Dharma kabupaten Sleman [Feasibility analysis of water tariffs based on Minister of Home Affairs Regulation Number 23 of 2006, data for 2009 s.d 2012. Case Study at Pdam Tirta Dharma, Sleman Regency]. *Jurnal Akuntansi*, *1* (2), 60–73.

Juheri & Indryani, R. (2008). Analisa penentuan tarif air minum PDAM Kota Palangka Raya [Analysis of determination of drinking water tariffs for PDAM Palangka Raya City]. In R. Basuki (Ed.), *Prosiding Seminar Nasional Aplikasi Teknologi Prasarana Perkotaan tanggal 31 juli 2008*. Surabaya.

Massarutto, A. (2007). Water pricing and full cost recovery of water services: economic incentive or instrument of public finance? *Water Policy*, *9* (6), 591–613.

Nurhotijah, Y. & Situmorang, M. (2017). *Analysis of calculation of cost of water production as the basis of selling price determination in PDAM Tirta Jaya Mandiri, Sukabumi Regency* [unpublished].

Peraturan Kementerian Dalam Negeri (Permendagri) tentang Perhitungan Dan Penetapan Tarif Air Minum Peraturan Menteri Dalam Negeri Republik Indonesia nomor 71 tahun 2016 tentang

perhitungan dan penetapan tarif air minum [Regulation of the Ministry of Home Affairs No 71 of 2016 concerning Calculation and Determination of Drinking Water Tariffs]. Republik Indonesia Tahun 2016 Nomor 1400.

Peraturan Kementerian Dalam Negeri (Permendagri) tentang Perubahan Atas Peraturan Menteri Dalam Negeri Nomor 71 Tahun 2016 Tentang Perhitungan Dan Penetapan Tarif Air Minum [Regulation of the Minister of Home Affairs of the Republic of Indonesia No 21 of 2020 about amendment to regulation of Regulation of the Ministry of Home Affairs No 71 of 2016 concerning Calculation and Determination of Drinking Water Tariffs]. Republik Indonesia Tahun 2020 Nomor 406.

Pinto, F. S., Carvalho, B. de & Marques, R. C. (2021). Adapting water tariffs to climate change: linking resource availability, costs, demand, and tariff design flexibility. *Journal of Cleaner Production*, *290*, 125803.

Pinto, F. S., Tchadie, A. M., Neto, S. & Khan, S. (2018). Contributing to water security through water tariffs: some guidelines for implementation mechanisms. *Journal of Water Sanitation and Hygiene for Development*, *8* (4), 730–739.

Pribadi, S. & Pangeran, M. H. (2015). Important risks on public-private partnership scheme in water supply investment in Indonesia. *EACEF*, *2015*, 67–74.

Supriatini, K. A., Jumiari, N. K. V., Agihidayantari, M. D. A. F. E. & Dewi, L. P. D. C. (2017). Analisis perhitungan harga pokok produksi air sebagai dasar penentuan harga jual air pada perusahaan daerah air minum (PDAM) Kabupaten Buleleng [Analysis of the calculation of the cost of water production as a basis for determining the selling price of water at the regional drinking water company (PDAM) of Buleleng Regency]. *Jurnal Ilmiah Akuntansi dan Humanika*, *7* (3), 207–212.

Tirta Musi (2020). *Research and Development Study Report of PDAM Tirta Musi*. Palembang [unpublished].

Tirta Musi (2021). *Research and Development Study Report of PDAM Tirta Musi*. Palembang [unpublished].

Whittington, D. (2003). Municipal water pricing and tariff design: a reform agenda for South Asia. *Water Policy*, *5* (1), 61–76.

Summary

Analysis of tariff adjustment for clean water usage. This study aims to assess the water supply company's tariff modification under various circumstances. To evaluate the financial situation if no tariff modifications were made, the study first conducted an examination of the existing financial data. A tariff adjustment scenario is also run through an investment feasibility test and until it reaches the full cost recovery (*FCR*). A variety of scenarios for tariff adjustment were run, each one with a different percentage increase in tariffs and a different time period for the increase in tariffs. These scenarios were based on the findings of the

analysis done on the water demand and the adjustment of water usage tariffs at PDAM Tirta Musi Palembang. This hypothetical situation demonstrated how higher tariffs will affect the company's ability to increase revenue. To sum up, this study has offered a framework about tariff adjustment under various alternatives, and examples of successful and unsuccessful pricing strategies in the local water company.

Scientific Review Engineering and Environmental Sciences (2023), 32 (2), 175–185

Sci. Rev. Eng. Env. Sci. (2023), 32 (2) https://srees.sggw.edu.pl

ISSN 1732-9353 (suspended) eISSN 2543-7496 DOI 10.22630/srees.4889

Received: 28.04.2023
Accepted: 18.05.2023

Stefan IGNAR[1]✉ https://orcid.org/0000-0002-5080-8695

Sylwia SZPORAK-WASILEWSKA[2] https://orcid.org/0000-0001-8012-0894

Małgorzata GREGORCZYK[3]

[1]Warsaw University of Life Sciences – SGGW, Institute of Environmental Engineering, Poland
[2]Warsaw University of Life Sciences – SGGW, Water Centre, Poland
[3]Warsaw University of Life Sciences – SGGW, Foreign Language Teaching Centre, Poland

Spatial mapping of the leaf area index using remote sensing and ground measurements – the Biebrza National Park case study

Keywords: leaf area index, wetlands, remote sensing, spectral vegetation indices, Biebrza

Introduction

The leaf area index (*LAI*) is one of the most important parameters describing the vegetation structure in terrestrial ecosystems. It is related to many environmental processes, including biophysical processes affecting the exchange of matter and energy between soil, vegetation and the atmosphere, such as photosynthesis, transpiration, evapotranspiration, interception, biomass and net primary production. The parameter is fundamental to studies of the dynamics of vegetation change and, above all, to studies of the exchange of energy and mass fluxes within the vegetation–atmosphere interface. It is defined as the summed ratio of the one-sided leaf area to the substrate area over which it is located:

$$LAI = \frac{one\ sided\ leaf\ area}{substrate\ area}[\mathrm{m}^2].$$

✉stefan_ignar@sggw.edu.pl

The parameter is one of the most difficult to estimate correctly due to its considerable spatial as well as temporal variability. In the field, it can be determined by several direct and indirect measurement methods. Direct measurement methods are among the most accurate but are time-consuming and difficult to implement on a large scale. Indirect measurement methods include, but are not limited to, optical methods that infer *LAI* from the transmission of radiation through vegetation cover using the radiative transfer theory (Welles & Cohen, 1996). These are non-invasive methods that describe vegetation structure in a statistical and probabilistic approach. They use Beer–Lambert's law, according to which the total amount of radiation intercepted by a vegetation cover depends on the vegetation structure, optical properties and instantaneous irradiance (Szporak, 2012). Measurements using non-invasive methods enable rapid and efficient acquisition of information about the *LAI* values of the vegetation present in a given area, which can then be used to determine the spatial variability of the index from remotely sensed data.

In the analyses conducted as part of this study, the LAI-2000 Plant Canopy Analyzer from LI-COR Biosciences was used to measure the leaf area index. The instrument measures diffuse blue light (320–490 nm) at a 148-degree viewing angle (fisheye lens). To calculate the *LAI* value at a given research area, it is necessary to take measurements both above the vegetation cover (reference measurement) and in the plant community. Based on the amount and intensity of diffuse blue light reaching the sensor, the projected area of leaves is estimated using algorithms implemented in the control console (LI-COR Biosciences, Inc., 1992). Measurements of the index were made for wetland vegetation of the Biebrza river valley, taking into account selected communities of sedge rushes (*Caricetum appropinquatae*, *Caricetum elatae*), willow scrub (*Salicetum pentandro-cinereae*), alder (*Ribeso nigri-Alnetum*) in the lower Biebrza and acid low sedge mire (*Carici canescentis-Agrostietum caninae*) in the upper Biebrza river valley. Unfortunately, measurements of the *LAI* for this vegetation type are still rare in the national as well as the world literature. Most studies on the formation of this index mainly concern forests and agricultural land. In Europe, studies on the formation of spatial variability of *LAI* for grass or sedge vegetation of wetlands were conducted, among others, by Darvishzadeh, Skidmore, Atzberger and Wieren, (2008), Dąbrowska-Zielińska, Gruszczyńska, Lewiński, Hościło and Bojanowski (2009), Budzyńska, Dąbrowska-Zielińska, Turlej, Małek and Bartold (2011), Darvishzadeh, Atzberger, Skidmore and Schlerf (2011), and Szporak (2012). Measurements of the leaf area index carried out within the framework of these studies made it possible to work out both its seasonal variability in 2007 and to determine its spatial variability using Landsat 5TM remote sensing data.

Study area

The study was carried out in north-eastern Poland in the Biebrza river valley within the boundaries of the Biebrza National Park (Fig. 1). In relation to adjacent areas, the valley is marked as an area with different thermal and humidity characteristics. This is due to the overlapping of climate features associated with the extensive peatlands, the valley form and the general climate features of north-eastern Poland. The climate is close to continental with subboreal elements. It is characterized by a long winter, a long pre-winter and the shortest (except in the mountains) growing season.

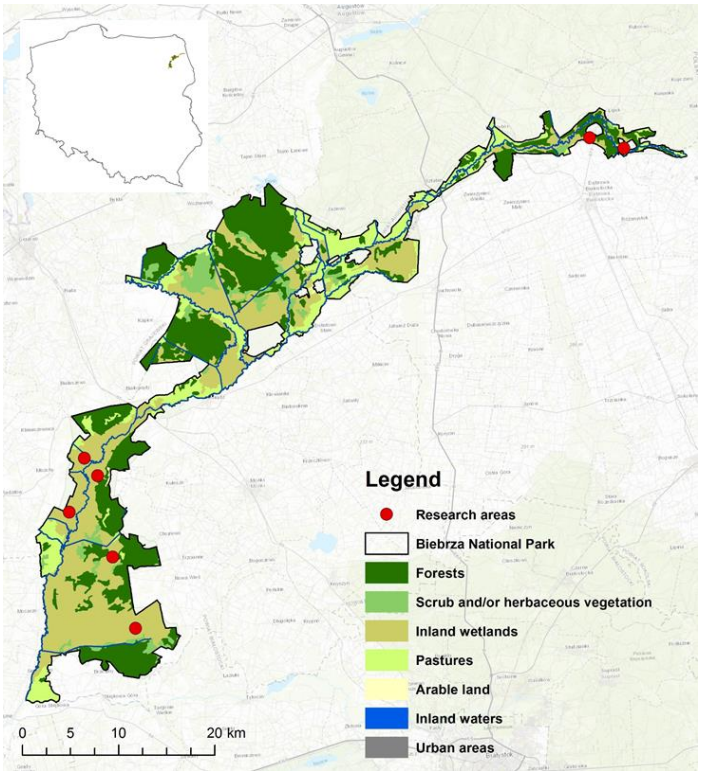

FIGURE 1. Location of research areas in Biebrza National Park
Source: own work.

In the Biebrza basin area, a decrease in temperature from south-west to north-east is observed between November and March. In the coldest month of the year, February, the average monthly temperature decreases from approx. –4.5°C on the

south-western edges (lower basin) to approx. –5.5°C at the north-eastern extremities (upper basin), with a maximum average of about –1.5 to 2.5°C and a minimum average of approx. –8.5 to –9.0°C. Winter starts the earliest in the north-east (27 November) and the latest in the south-west (4 December). It lasts 107–108 days in the lower basin and 116–117 days in the upper basin. Average annual precipitation in the northern part of the Biebrza basin ranges from 470 to 550 mm, while in the southern part it is about 550 mm. The highest precipitation falls in summer, with a maximum in July (70–90 mm), and the lowest in January to March, with a minimum in January (20–25 mm). In the north-eastern part of the Biebrza basin, summer semiannual precipitation exceeds 67% of the annual total, while in the rest of the basin it is about 65%. The Biebrza river flows in a valley with low gradients, and groundwater feeding the valley flows slowly towards the riverbed or exfiltrates in the bottom of the wetlands that occur here. The wetlands of the Biebrza valley are primarily peatland ecosystems. Covering an area of over a 100 thous. ha, they form one of the largest peat complexes in Poland.

Methodology

Field measurements

The leaf area index field measurements were made at a fixed altitude with the same azimuthal position of the sensor and at several locations of the plant community under study so as to capture its heterogeneity and obtain a representative sample for the *LAI* models implemented in the LAI-2000 recorder. The *LAI* value at a given measurement point was usually the average of 10–11 measurements. Measurements for the selected plant community were taken within a limited area, the size of which was dictated by the size of the plant community patch, as well as the spatial resolution of the Landsat 5TM satellite image. In the case of *LAI* measurements in the forest, reference measurements were usually taken at the forest edge or in adequately large clearings within them.

Remote sensing data

A medium-resolution satellite image from the Landsat 5TM satellite (U.S. Geological Survey [USGS], 2023) from 28 May 2007 was used in the estimation of the spatial variability of *LAI*. The image was subjected to atmospheric correction using the MODTRAN radiative transfer model based on the physical characteristics of the actual atmospheric conditions. The estimation of the spatial distribution of the *LAI* is based on an empirical relationship between vegetation parameters measured in the field and spectral vegetation indices developed from the satellite

image. The vegetation index is calculated based on a combination of several spectral bands, whose values are added, divided or multiplied between each other to obtain a value representing the area and condition of the vegetation cover. Due to the type of remote sensing data processed, selected broadband indices were used in the analyses (Table 1). The simplest spectral index is the simple ratio (SR) representing the ratio between near-infrared and red reflectance.

TABLE 1. Selected spectral indices

Spectral index	Abbreviation	Equation	References
Difference vegetation index	*DVI*	$NIR - Red$	Tucker (1979)
Enhanced vegetation index	*EVI*	$\frac{2.5 \cdot (NIR - Red)}{1 + NIR + 6 \cdot Red - 7.5 \cdot Blue}$	Birth and McVey (1968)
Global environment monitoring index	*GEMI*	$\eta(1 - 0.25\eta)\frac{Red - 0.125}{1 - Red}$ $\eta = \frac{2(NIR^2 - Red^2) + 1.5 \cdot NIR + 0.5 \cdot Red}{NIR + Red + 0.5}$	Pinty and Verstraete (1992)
Modified soil adjusted vegetation index	*MSAVI2*	$0.5\left[2 \cdot NIR + 1 - \sqrt{(2 \cdot NIR + 1)^2 - 8 \cdot (NIR - Red)}\right]$	Qi, Chehbouni, Huete, Kerr and Sorooshian (1994)
Moisture stress index	*MSI*	$\frac{SWIR}{NIR}$	Rock, Vogelmann, Williams, Vogelmann and Hoshizaki (1986)
Modified simple ratio	*MSR*	$\frac{\left(\frac{NIR}{RED} - 1\right)}{\left(\sqrt{\frac{NIR}{RED}} + 1\right)}$	Chen (1996)
Normalized difference vegetation index	*NDVI*	$\frac{NIR - Red}{NIR + Red}$	Rouse, Haas, Schell and Deering (1974)
Renormalized vegetation index 1	*RDVI1*	$\sqrt{NDVI \cdot DVI}$	Roujean and Breon (1995)
Renormalized vegetation index 2	*RDVI2*	$\frac{NIR - Red}{\sqrt{NIR + Red}}$	Roujean and Breon (1995)
Soil and atmospherically resistant vegetation index	*SARVI*	$\frac{(1+1) \cdot (NIR - Rrb)}{NIR + Rrb + 1}$ $Rrb = Red - 1 \cdot (Blue - Red)$	Kaufman and Tantré (1992)
Soil adjusted vegetation index	*SAVI*	$(1 + L)\frac{NIR - Red}{NIR + Red + L}$	Huete (1988)
Simple ratio	*SR*	$\frac{NIR}{Red}$	Jordan (1969)
Triangular vegetation index	*TVI*	$0.5 \cdot [120 \cdot (NIR - Green) - 200 \cdot (Red - Green)]$	Broge and Leblanc (2000)

Source: own work.

Results

Results of field measurements

The study shows that the highest values of the *LAI* coefficient are observed for the majority of plant communities in the Biebrza valley during the full growing season, i.e., in June and July (Fig. 2). The growing season in this part of Poland is quite short (about 192 days), and already in August we observe a decrease in the leaf projection area of the majority of the analyzed plant communities.

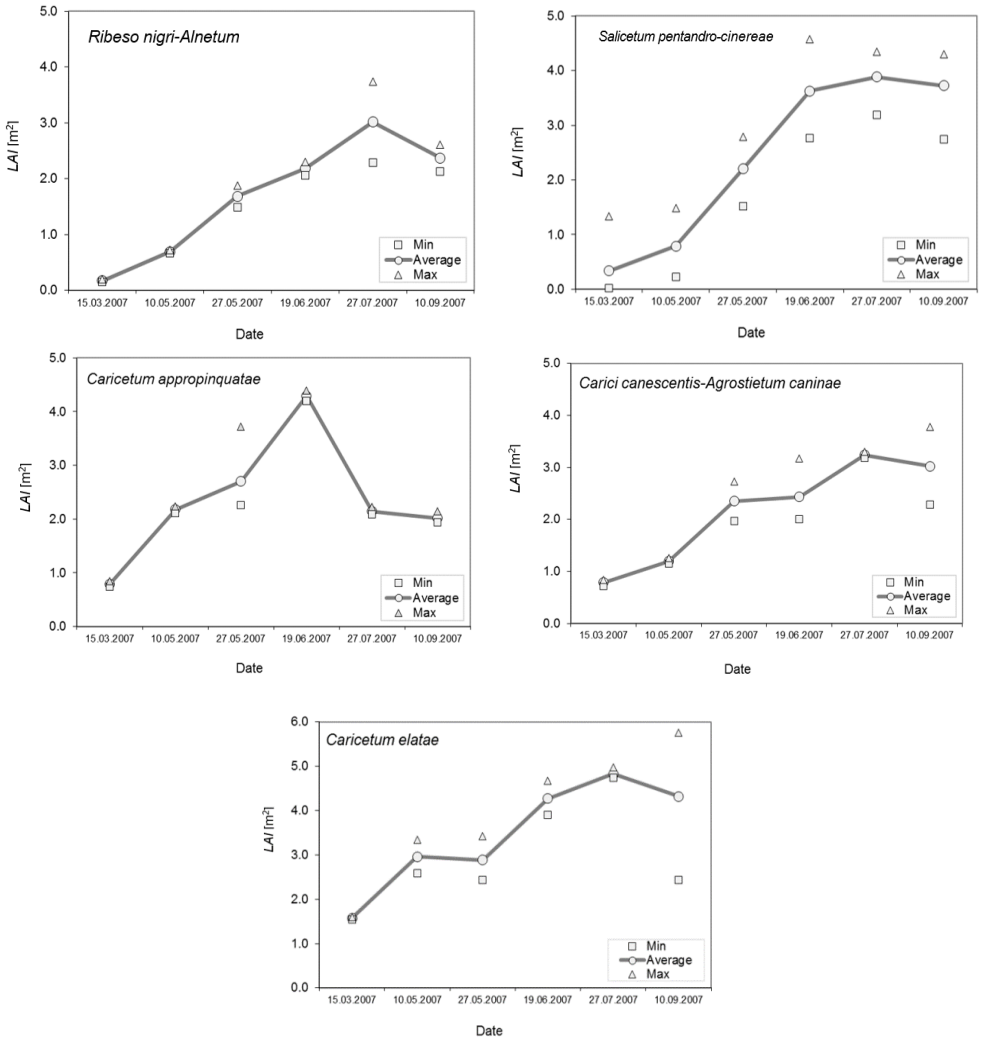

FIGURE 2. Seasonal variation of the leaf area index (*LAI*) for selected plant communities in the Biebrza valley

Source: own work.

The seasonal variation of the *LAI* for low vegetation is somewhat different from that of willow scrub and alder. The difference is particularly marked at the beginning of the growing season when the leaf area index of low vegetation increases more dynamically. The situation reverses in June when there is a gradual, further increase in *LAI* for forest and scrub communities, and a smaller increase for sedge communities and meadows, which are mown at this time. The fieldwork shows that the vegetation of natural river valleys is characterized by a high degree of variability not only in space, but also in the duration of the growing season.

Results of remote sensing analyses

The statistical relationship between the *LAI* values measured in the field and the spectral indices calculated for the satellite image is shown in Table 2 and Figure 3. All spectral indices were significantly correlated with the *LAI* ($p < 0.05$). The highest coefficient of determination and the highest correlation coefficient were obtained for *NDVI* (0.7174). The linear regression models and the obtained coefficients of determination for the analyzed spectral vegetation indices are presented in Table 2.

TABLE 2. Spectral vegetation indices (*SVI*) with developed linear regression model and coefficient of determination

Spectral vegetation indices (*SVI*)	Regression model	R^2
NDVI	9.7686*x* – 1.9528	0.7174
SAVI	8.886*x* – 1.9520	0.7173
MSI	–3.6807*x* + 6.4378	0.6982
MSR	3.276*x* – 0.438	0.6958
SR	1.1813*x* – 0.7640	0.6652
RDVI2	0.7296*x* – 1.1814	0.6290
SARVI	1.8348*x* – 2.012	0.5979
TVI	0.0008*x* – 0.2074	0.5756
RDVI1	0.8219*x* – 3.6049	0.5282
MSAVI2	0.0482*x* – 0.2378	0.5172
DVI	0.05*x* – 0.2491	0.5069
GEMI	0.0003*x* + 1.4864	0.4589
EVI	–5.2764*x* + 0.1103	0.4147

Source: own work.

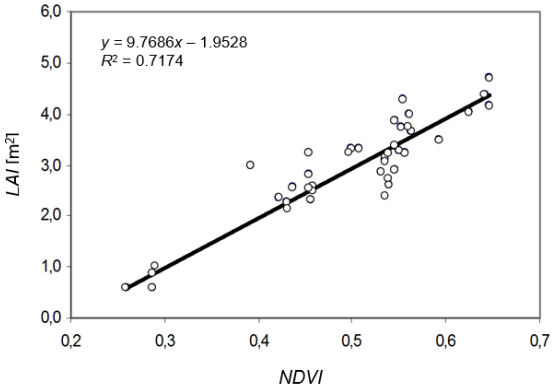

FIGURE 3. Linear regression model (*LAI*), based on normalized difference vegetation index (*NDVI*), selected for further analysis

Source: own work.

Ignar, S., Szporak-Wasilewska, S., Gregorczyk, M. (2023). Spatial mapping of the leaf area index using remote sensing and ground measurements – the Biebrza National Park case study. *Sci. Rev. Eng. Env. Sci.*, *32* (2), 175–185. DOI 10.22630/srees.4889

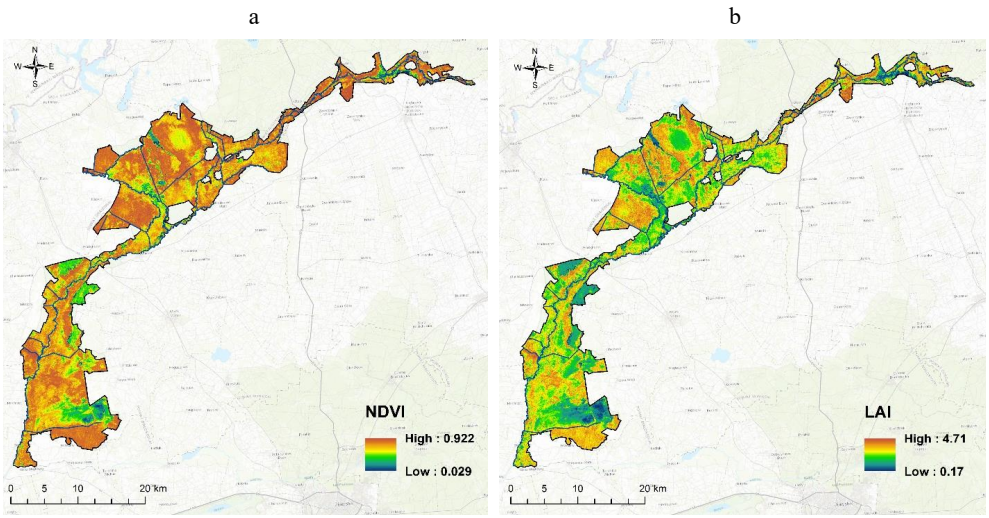

FIGURE 4. Map of the spatial variability of the normalized difference vegetation index – *NDVI* (a) and the leaf area index – *LAI* (b)

Source: own work.

From the analysis of the satellite image taken in May, the *LAI* reached the highest values in that part of the valley where significant areas are covered by reed and sedge rushes and deciduous forests (alder and swamp birch) characterized by high biomass. The lowest values of the index were observed in groundwater-logged areas in the Ławki Marsh, as well as areas directly adjacent to the bed of the Biebrza river and its tributaries, where surface water flooding persisted in places (southern and south-western parts of the middle Biebrza valley and the middle part of the upper Biebrza valley).

Conclusions

The measurements of the leaf area index show that the vegetation of natural river valleys is characterized by high spatial and seasonal variability. The highest values of the *LAI* index were observed from the second half of June to the end of July for all considered plant communities of the Biebrza valley. The seasonal variability of the *LAI* for sedge communities developed differently from that of willow scrub and alder. At the beginning of the growing season, the *LAI* for sedge communities increases more dynamically. The situation changes in June, when, with a gradual increase in the *LAI* for forest and scrub communities reaching its maxi-

mum in mid-July, there is a smaller increase in the index for sedge communities. The main reason for this difference is the use of open areas of peatlands, which are mown in June. The study of the *LAI* on such a large extensively used area therefore additionally requires knowledge of the methods of use, as well as the timing of the application of individual agrotechnical measures.

Among the tested vegetation indices developed from the Landsat 5TM satellite imagery, the *NDVI* and *SAVI* indices produced the best results in estimating the spatial variability of the *LAI*. In the analysis carried out, these indices obtained a coefficient of determination value above 0.70.

References

Birth, G. S. & McVey, G. R. (1968). Measuring the colour of growing turf with a reflectance spectrophotometer. *Agronomy Journal*, *60* (6), 640–643. https://doi.org/10.2134/agronj1968.00021962006000060016x

Broge, N. H. & Leblanc, E. (2000). Comparing prediction power and stability of broadband and Hyperspectral vegetation indices for estimating of green leaf area index and canopy chlorophyll density. *Remote Sensing of Environment*, *76* (2), 156–172. https://doi.org/10.1016/S0034-4257(00)00197-8

Budzyńska, M., Dąbrowska-Zielińska, K., Turlej, K. Małek, I. & Bartold, M. (2011). Monitoring przyrodniczy Bagien Biebrzańskich z zastosowaniem teledetekcji. *Woda – Środowisko – Obszary Wiejskie*, *11* (3), 39–64.

Chen, J. M. (1996). Evaluation of vegetation indices and a modified simple ratio for boreal applications. *Canadian Journal of Remote Sensing*, *22* (3), 229–242.

Dąbrowska-Zielińska, K., Gruszczyńska, M., Lewiński, S., Hościło, A. & Bojanowski, J. (2009). Application of remote sensing and in situ information to the management of wetlands in Poland. *Journal of Environmental Management*, *90* (7), 2261–2269. https://doi.org/10.1016/j.jenvman.2008.02.009

Darvishzadeh, R., Skidmore, A., Atzberger, C. & Wieren, S. van (2008). Estimation of vegetation *LAI* from hyperspectral reflectance data: effects of soil type and plant architecture. *International Journal of Applied Earth Observation and Geoinformation*, *10* (3), 358–373. https://doi.org/10.1016/j.jag.2008.02.005

Darvishzadeh, R., Atzberger, C., Skidmore, A. & Schlerf, M. (2011). Mapping grassland leaf area index with airborne Hyperspectral imagery: A comparison study of statistical approaches and inversion of radiative transfer models. *ISPRS Journal of Photogrammetry and Remote Sensing*, *66* (6), 894–906. https://doi.org/10.1016/j.isprsjprs.2011.09.013

Huete, A. R. (1988). A soil-adjusted vegetation index (*SAVI*). *Remote Sensing of Environment*, *25* (3), 295–309. https://doi.org/10.1016/0034-4257(88)90106-X

Jordan, C. F. (1969). Derivation of leaf area index from quality of light on the forest floor. *Ecology*, *50* (4), 663–666. https://doi.org/10.2307/1936256

Kaufman, Y. J. & Tanré, D. (1992). Atmospherically resistant vegetation index (ARVI) for EOS--MODIS. *IEEE Transactions Geoscience of Remote Sensing*, *30* (2), 261–270. https://doi.org/10.1109/36.134076

LI-COR Biosciences, Inc. (1992). *LAI-2000 Plant Canopy Analyzer. Instruction Manual*. Retrieved form: https://licor.app.boxenterprise.net/s/q6hrj6s79psn7o8z2b2s [accessed: 27.04.2023].

Pinty, B. & Verstraete, M. M. (1992). GEMI: A non-linear index to monitor global vegetation from satellites. *Vegetatio*, *101*, 15–20. https://doi.org/10.1007/BF00031911

Qi, J., Chehbouni, A., Huete, A. R., Kerr, Y. H. & Sorooshian, S. (1994). A modified soil adjusted vegetation index. *Remote Sensing of Environment*, *48* (2), 119–126. https://doi.org/10.1016/0034-4257(94)90134-1

Rock, B. N., Vogelmann, J. E., Williams, D. L., Vogelmann, A. F. & Hoshizaki, T. (1986). Remote detection of forest damage. *BioScience*, *36* (7), 439–445. https://doi.org/10.2307/1310339

Roujean, J. L. & Breon, F. M. (1995). Estimating PAR absorbed by vegetation from bidirectional reflectance measurements. *Remote Sensing of Environment*, *51* (3), 375–384. https://doi.org/10.1016/0034-4257(94)00114-3

Rouse, J. W., Haas, R. H., Schell, J. A. & Deering, D. W. (1973). Monitoring vegetation systems in the Great Plains with ERTS. *NASA Special Publications*, *351* (1), 309–317.

Szporak, S. (2012). *Zastosowanie metod teledetekcyjnych dla szacowania ewapotranspiracji na przykładzie Dolnego Basenu rzeki Biebrzy* [*Remote sensing methods in assessment of evapotranspiration in the Biebrza River Lower Basin*] (doctoral thesis). Warsaw University of Life Sciences, Warsaw.

Tucker, C. J. (1979). Red and photographic infrared linear combinations for monitoring vegetation. *Remote Sensing of Environment*, *8* (2), 127–150. http://dx.doi.org/10.1016/0034-4257(79)90013-0

U.S. Geological Survey [USGS] (2023). Earth Explorer portal. Retrieved from: https://earthexplorer.usgs.gov [accessed 27.04.2023].

Welles, J. M. & Cohen, S. (1996). Canopy structure measurement by gap fraction analysis using commercial instrumentation. *Journal of Experimental Botany*, *47* (9), 1335–1342. https://doi.org/10.1093/jxb/47.9.1335

Summary

Spatial mapping of leaf area index using remote sensing and ground measurements – the Biebrza National Park case study. The purpose of the described research was an attempt to estimate the leaf area index (*LAI*) parameter describing the structure of the vegetation based on Landsat 5TM satellite imagery and field measurements made with the use of an optical plant canopy analyzer. The study was carried out in north-eastern Poland in the Biebrza river valley within the boundaries of the Biebrza National Park during the growing season of the year 2007. There were 13 spectral indices given in the literature known to be

correlated with the *LAI*. The highest coefficient of determination and the highest correlation coefficient was obtained for the normalized difference vegetation index (*NDVI*) and the soil adjusted vegetation index (*SAVI*) indices for wetland areas in the Biebrza river valley. The field measurements of the leaf area index and its spatial representation on satellite image show that the vegetation of natural river valleys is characterized by high spatial and seasonal variability. The study of *LAI* on such large natural areas that are extensively used also requires knowledge of the methods of land use and the application of individual agrotechnical measures.

Scientific Review Engineering and Environmental Sciences (2023), 32 (2), 186–197

Sci. Rev. Eng. Env. Sci. (2023), 32 (2) https://srees.sggw.edu.pl

ISSN 1732-9353 (suspended) eISSN 2543-7496 DOI 10.22630/srees.4583

Received: 22.12.2022
Accepted: 27.04.2023

Mus'ab A. Al-TAMIR

Abdullah I. IBRAHIM✉ https://orcid.org/0000-0002-7391-3885

University of Mosul, College of Engineering, Environmental Engineering Department, Iraq

Spatial distribution prediction for the ground water quality in Mosul City (Iraq) using variogram equations

Keywords: GIS, geospatial interpolation, groundwater quality, kriging, semivariogram model

Introduction

Spatially distributed data sets play a crucial role in environmental modeling and monitoring. Geological information system (GIS) has been applied successfully in this field over the last two decades. GIS-aided environmental studies achieved high quality outputs in many aspects, such as water quality policies and modeling, as well as improving controls and assisting confident decisions (Sukkuea & Heednacram, 2022). In addition, integration of GIS-based tools with in-situ measurements have been used extensively to identify and describe spatial and temporal variation of pollutants in surface and groundwater (Xue et al., 2023). The GIS-based tools provide reliable interpolation for specific information even at a regional scale (Kourgialas, Karatzas & Koubouris, 2017). Furthermore, the combination of data visualization and mapping with GIS platform is a powerful tool for extracting information and results interpretation (Fan, Fleischmann, Collischonn, Ames & Rigo, 2015). The GIS platform also has a capability to display and analyze geospatial data as well as to create multiple scenarios for land use (Alqahtany, 2023). Geostatistical analysis is one of the powerful tools embedded in the GIS software. It relies on a combination of several techniques that were employed to

✉abdullah.ibrahim@uomosul.edu.iq

solve problems and predict outputs with respect to spatial distribution of data (Montero, Fernández-Avilés & Mateu, 2015). Thus, the geostatistical analysis is widely used to determine the data magnitude for the positions where measurements are lost or unsampled due to safety restrictions, materials availability, or cost considerations (Sukkuea & Heednacram, 2022). The geostatistical analysis consists of a set of steps as spatial interpolation, kriging interpolation, and data fit and error assessment.

Spatial interpolation

Spatial interpolation is to estimate an unknown data point based on the known or investigated points. The influence of known points is proportional to the distance between points. In other words, the weight of nearby points has higher impact on unknown point than those distant data points. The data at unknown points can be calculated as follows.

$$z_p(x) = \sum_{i=1}^{n} w_i \cdot z(X_i), \tag{1}$$

where $z_p(x)$ donating the value of targeted unknown data point, $z(X_i)$ the value of investigated points S_i at point $i = 1, 2$ through n, and w_i is the weight that assigned to each known point. The summation of weight at each single point has to equal to 1.

Semivariance

Semivariance is a function of the distance between the observed and unknown data points. It measures the average degree of dissimilarity between unsampled sites and nearby data values (Koike et al., 2022). Semivariance is proportional to spatial distribution of data points, the lower semivariance associated to lower distance and vice versa. The optimum semivariogram model simulates natural variability of water quality parameters with least root mean square error (*RMSE*) when compared to real water quality parameters. The semivariogram model that achieves minimum *RMSE* is flexible enough to describe the spatial distribution of the studied parameters. The semivariance (γ_h) calculated according to Eq. (2) is then optimized to find the most representative outputs or surface.

$$\gamma_h = \frac{1}{2n(h)} \sum_{i=1}^{n(h)} \left[z(x_i) + z(x_{i+h}) \right]^2, \tag{2}$$

where $n(h)$ is the number of pairs separated by distance h, $Z(x)$ is the value of z at location x, $z(x + h)$ is the value of z at location $x + h$.

Semivariogram models

Semivariogram function fits the spatially autocorrelated paired data points through certain geostatistical procedures. Each set of parameters can fit many empirical models of a semivariogram, such as spherical, circular, quadratic, exponential, rational, tetraspherical, pintaspherical, Gaussian, K-Bessel, J-Bessel, hole effect and stable models (Silva et al., 2023). The selected semivariogram model influences the interpolation of the unknown or missing data. The more the shape of the semivariogram curve is approaching the realistic investigations, the more accurately interpolation will be achieved at virtual or uninvestigated stations (Koike et al., 2022). In other words, the steeper the curve nearby the origin, the higher influence of closed neighbor points on the interpolated surface (Raju, 2016).

According to the regionalized variable theory, two steps need to be followed in the geostatistical analysis to generate a surface. The first step is to construct an empirical semivariogram model with least square error, and then the second step is to produce an interpolation based on the existing known data and the empirical semivariogram model (Grynyshyna-Poliuga, 2019; Sukkuea & Heednacram, 2022).

Kriging interpolation

Kriging interpolation was developed in the 1960s to estimate gold deposited in a rock from a few random core samples (Beana, Sun & Maguire, 2022). Since then, kriging has found its way into other scientific disciplines. Among various spatial interpolation methods, such as trend surface estimation, spline interpolation, and inverse distance weighting, kriging interpolation is the most commonly used in environmental studies (Thanoon, 2018; Yang, Chiu & Yen, 2023). Kriging or Gaussian process regression is an advanced geostatistical approach that uses the semivariogram model to generate unbiased estimation for spatially distributed surface (Sukkuea & Heednacram, 2022). Among many forms of linear and nonlinear kriging, ordinary kriging and lognormal kriging are most commonly used to run interpolation process. Therefore, these kriging procedures were used in this study.

Data fit and error assessment

The collected data were used to generate an empirical semivariogram. Afterward, a reasonable theoretical semivariogram model was fitted based on the least root mean square error (*RMSE*) value (Boroh, Lawou, Mfenjou & Ngounouno, 2022). The *RMSE* was calculated using Eq. (3). The *RMSE* investigate the gap between observed and predicted data points.

$$RMSE = \sqrt{\frac{SSE}{n}}, \tag{3}$$

$$SE = \left\{ \sum_{i=1}^{n} (p_i - o_i)^2 \right\}^{\frac{1}{2}}, \tag{4}$$

where *SSE* is a *t* square root of the sum of squared errors (predicted-observed values) and *n* is the number of pairs (errors).

The *RMSE* is frequently used to evaluate errors in GIS and mapping and many other prediction methods. Thus, it was employed in this study to evaluate outputs of several semivariogram models. A properly fitted semivariogram model was then used to generate autocorrelation to reflect the spatial distribution of the studied variables to produce a mapped surface.

Although the kriging algorithms are used extensively in semivariogram modeling, there is a lack of knowledge about how to optimize this approach to meet water quality modeling requirements (Sukkuea & Heednacram, 2022).

This study aimed to discover the optimum ordinary semivariogram model to predict pH, EC and temperature for groundwater quality for selected wells in the Mosul Province of northern Iraq. The second objective of this study was to explore the pattern of spatial distribution of these parameters over the study area.

Study area and data used

Mosul is the largest city in northern Iraq in terms of population. It is located approximately 400 km North of Baghdad, the capital of Iraq. The latitude coordinate of Mosul City is 36.340000 and the longitude coordinate is 43.130001. According to the latest census, the population of Mosul City is over 3.7 million. Although the Tigris River is the major water supply resource in Mosul, groundwater is also used in some sectors in daily bases for other uses rather than household purposes (Al-Tamir, 2021). Representative groundwater samples were collected from 30 different sites (wells) distributed over different places in Mosul City (Fig. 1). Then the collected samples were analyzed for pH, electrical conductivity (EC), and temperature as a model for groundwater quality in Mosul City.

Al-Tamir, M. A., Ibrahim, A. I. (2023). Spatial distribution prediction for the ground water quality in Mosul City (Iraq) using variogram equations. *Sci. Rev. Eng. Env. Sci.*, *32* (2), 186–197. DOI 10.22630/srees.4583

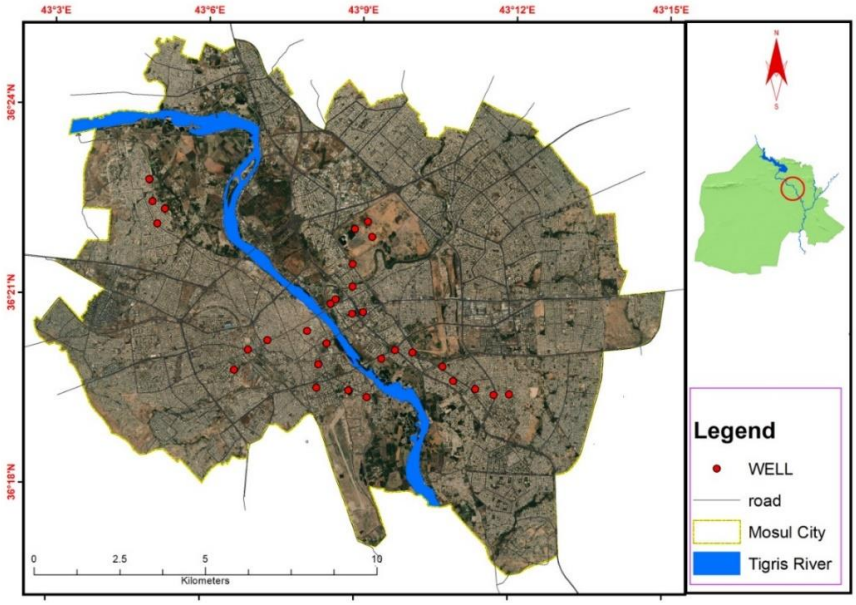

FIGURE 1. Wells distribution map in Mosul City
Source: own work.

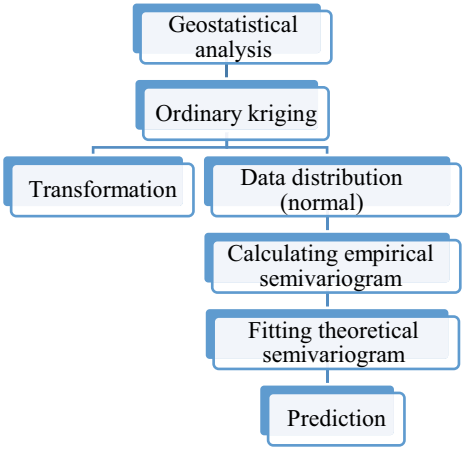

FIGURE 2. Geostatistical analysis steps
Source: own work.

Methodology

The GIS-aided spatial interpolation was applied on the collected data to predict the selected parameters (i.e., pH, EC, and temperature). The geostatistical analysis was applied according to the steps presented in Figure 2.

The normality of the collected data was tested prior to applying the geostatistical analysis. The transformation process was applied, as needed, on data to meet the normal distribution requirements (Fig. 3).

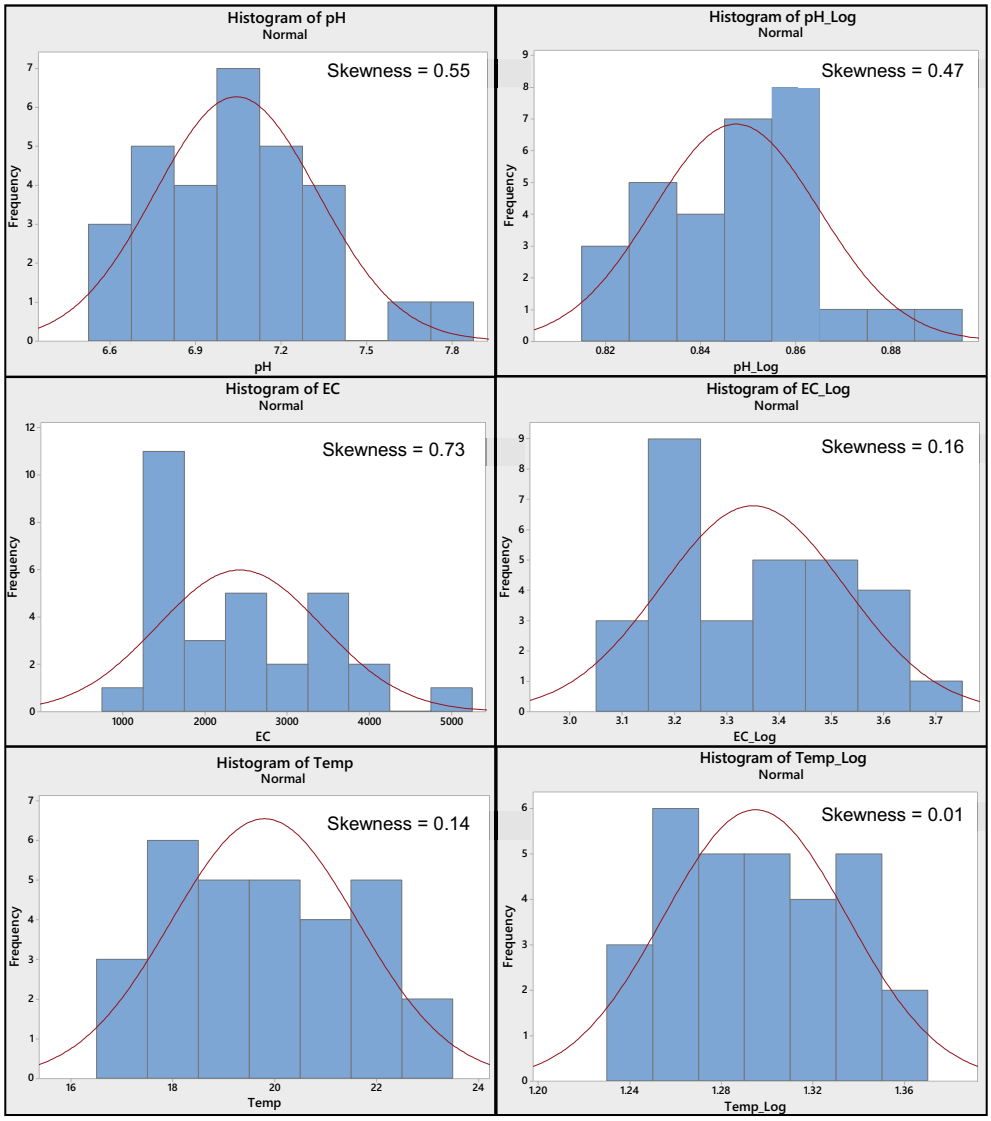

FIGURE 3. Original and transformed normal distribution histogram for each parameter
Source: own work.

The final step was to calculate the empirical semivariogram and compare it with the fitted theoretical semivariogram. The main objective of this procedure was to fit the optimum semivariogram model to represent groundwater quality in sites that have not been sampled. The statistical analysis was performed using Minitab 17 (Minitab 17, 2010).

Al-Tamir, M. A., Ibrahim, A. I. (2023). Spatial distribution prediction for the ground water quality in Mosul City (Iraq) using variogram equations. *Sci. Rev. Eng. Env. Sci.*, *32* (2), 186–197. DOI 10.22630/srees.4583

Results and discussion

Statistical indices

The statistical summary of the collected groundwater quality properties is presented in Table 1. The mean values of pH, EC, and temperature were 7.04, 2426, and 19.8, respectively, while the variance of these parameters was 0.082, 999521, and 3.338, also respectively. Since the variance measures variability of data set from the mean, it shows that the variance of pH and temperature values was close to mean values while the variance of EC was large, which indicates that the collected samples were highly deviated from the mean of the data set. Consequently, this indicates that water quality is impacted by the spatial distribution of wells. This finding is confirmed by the standard deviation test of the same samples (Table 1). Although, the skewness test shows that the data sets of all studied parameters had positive skewness (skewed right), pH and EC were moderately skewed while the temperature data set distribution was fairly symmetrical (Fig. 3). Which means that the distribution of data sets of pH and EC were slightly deviated from the normal distribution. However, the skewness of temperature data set was less than the skewness of other parameters (Table 1). Various functions, such as Log, exponential and square root, were applied on the collected data sets to adjust the normality of distribution. Log was the optimum transformation function because it produced the minimum skewness value (as shown in Table 1). The kurtosis test shows that the distribution of pH and EC data sets was mesokurtic (i.e., kurtosis values between +1 and –1) while the distribution of temperature data set was too flat (platykurtic), (Hair, Hult, Ringle & Sarstedt, 2014).

TABLE 1. The statistical summary for the studied water quality parameters*

Indicator	pH [-]	Electrical conductivity (EC) [-]	Temperature [°C]
Mean	7.04	2 426	19.8
Standard error	0.05	183	0.33
Median	7	2 250	20
Mode	7.2	2 500	18
Standard deviation	0.286	1 000	1.83
Variance	0.082	999 521	3.338
Kurtosis	0.47	–0.23	–1.11
Skewness	0.55	0.73	0.14
Range	1.2	3 850	6
Minimum	6.6	1 150	17
Maximum	7.8	5 000	23
Sum	211.3	72 765	594
Count	30	30	30

*Descriptive statistical analysis indicators were calculated according to common statistical functions.

Source: own work.

Semivariogram model fitting

The empirical semivariogram was computed according to the setting shown in Figure 4. The lag size for pH and temperature was 0.2 for each one, while it sat to 0.4 for EC. The number of lags was 12 for all data sets. The best-fit semivariogram model was selected based on the *RMSE* value (Table 2), the semivariogram model with the least *RMSE* was considered the optimal one. Accordingly, J-Bessel was the best-fit semivariogram model for all investigated parameters because it achieved the minimum *RMSE* as shown in Table 2.

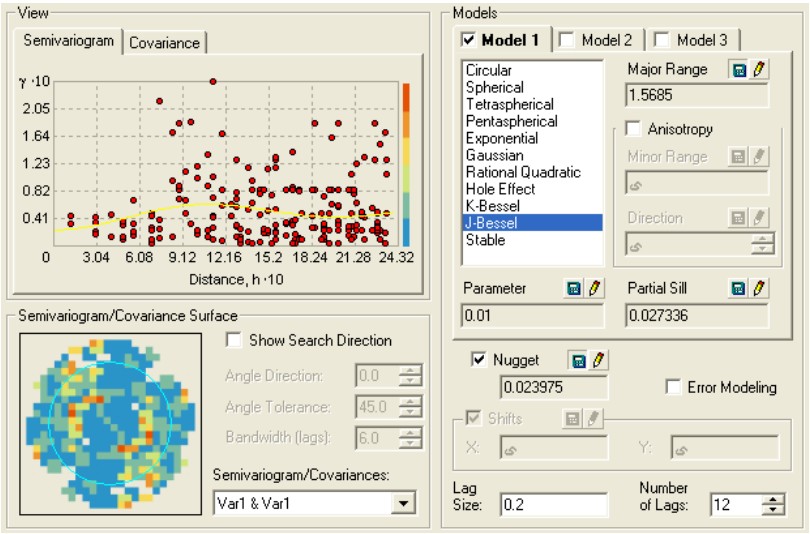

FIGURE 4. Empirical semivariogram settings for each water quality parameter

Source: own work.

TABLE 2. The root mean square error values for the examined models for each studied parameter*

Semivariogram model	pH [-]	Electrical conductivity (EC) [-]	Temperature [°C]
	Lag size: 0.2	Lag size: 0.4	Lag size: 0.2
Circular	0.2248	794.7	1.432
Tetraspherical	0.2261	790.6	1.447
Pentaspherical	0.2262	797.9	1.455
Exponential	0.2263	789.9	1.457
Gaussian	0.2292	886.7	1.554
Rational	0.2237	828	1.474
Quadratic	0.2266	774.6	1.514
Hole effect	0.2239	798.3	1.269
K-Bessel	0.2247	818.3	1.485
J-Bessel	0.2217	740.5	1.209
Stable	0.2237	–	1.492

*For more details refer to Table 1.

Source: own work.

Interpolation maps

Kriging type, output, transformation function, and semivariogram model were set to ordinary kriging, prediction, log, and J-Bessel, respectively. All above settings have been applied to create continuous interpolated surfaces for pH, EC, and temperature in Mosul City (Figs 5–7).

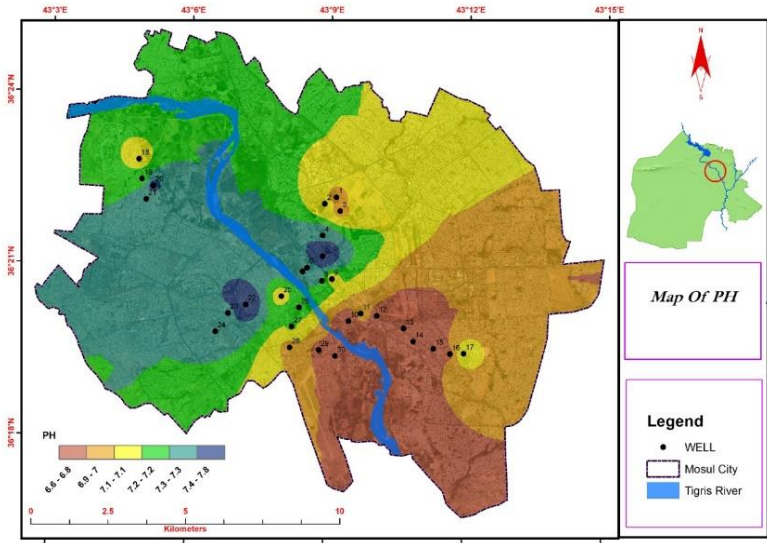

FIGURE 5. Interpolation map of pH in Mosul City
Source: own work.

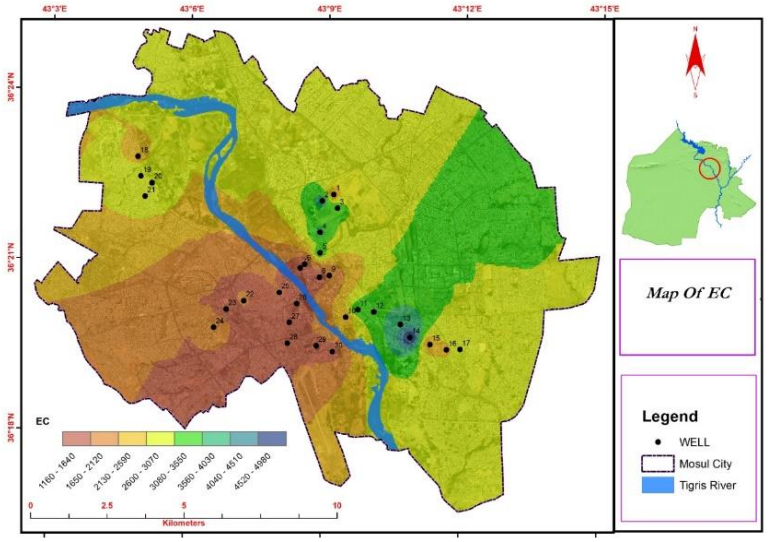

FIGURE 6. Interpolation map of electrical conductivity (EC) in Mosul City
Source: own work.

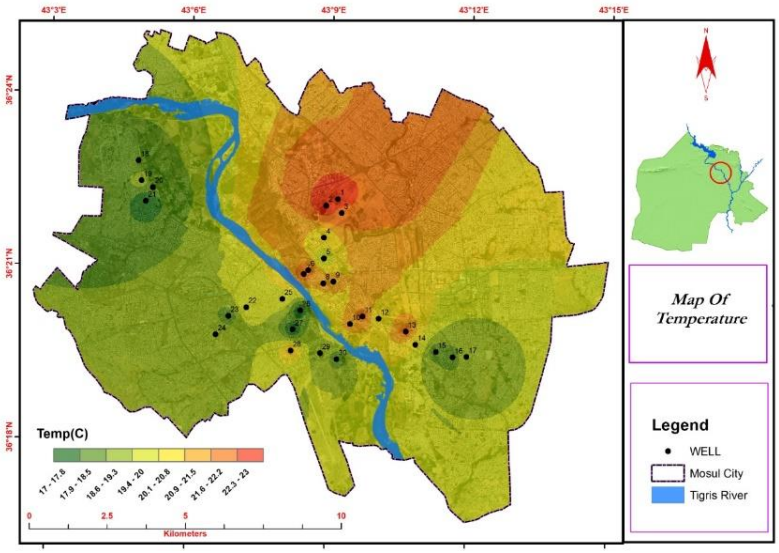

FIGURE 7. Interpolation map of temperature in Mosul City
Source: own work.

The geospatial analysis of the selected groundwater parameters can be considered optimal because it was created using the semivariogram model that has minimum *RMSE* values, as shown in Table 2. The limitation on availability of detailed data due to restricted limitations on drilling of water wells within the city border led to the lack of information regarding groundwater quality. Therefore, the suggested semivariogram model is likely the reliable selection for groundwater spatial modeling in Mosul City and thus it can be used to predict the groundwater parameters in unsampled sites.

Conclusions

Various semivariogram models were applied and optimized to find the best fit model to represent the spatial variability selected groundwater quality parameters in Mosul City. The high restrictions on digging water wells within the city border resulted in small sample size of acquired data sets. Therefore, the skewness test was employed to assess the normality of the data sets distribution. According to that test, natural logarithms were the best fit function to adjust the normality of data sets distribution. The J-Bessel semivariogram model was selected as the opti-

mum model based on the least *RMSE* for all selected groundwater parameters. In spite of the small sample size in terms of the number of wells, interpolation maps for pH, EC, and temperature showed a significant smoothness to represent interpolation surfaces for the studied parameters. Consequently, the adjusted settings are optimal and can be applied successfully for modeling the groundwater quality relaying on a small sample size.

References

Al-Tamir, M. A. (2021). Stability evaluation of Tigris River raw water and treated drinking water from main water treatment plants within Mosul City. *Desalination and Water Treatment*, *226*, 52–61.

Alqahtany, A. (2023). GIS-based assessment of land use for predicting increase in settlements in Al Ahsa Metropolitan Area, Saudi Arabia for the year 2032. *Alexandria Engineering Journal*, *62*, 269–277.

Beana, B., Sun, Y. & Maguire, M. (2022). Interval-valued kriging for geostatistical mapping with imprecise inputs. *International Journal of Approximate Reasoning*, *140*, 31–51.

Boroh, A. W., Lawou, S. K., Mfenjou, M. L. & Ngounouno, I. (2022). Comparison of geostatistical and machine learning models for predicting geochemical concentration of iron: case of the Nkout iron deposit (south Cameroon). *Journal of African Earth Sciences*, *195*, 104662.

Fan, F. M., Fleischmann, A. S., Collischonn, W., Ames, D. P. & Rigo, D. (2015). Large-scale analytical water quality model coupled with GIS for simulation of point sourced pollutant discharges. *Environmental Modelling & Software*, *64*, 58–71.

Grynyshyna-Poliuga, O. (2019). Characteristic of modelling spatial processes using geostatistical analysis. *Advances in Space Research*, *64*, 415–426.

Hair, J. F., Hult, J. G. T. M., Ringle, C. M. & Sarstedt, M. S. (2014). *A primer on partial least squares structural equation modeling (PLS-SEM)*. Thousand Oaks: SAGE Publications.

Koike, K., Kiriyama, T., Lu, L., Kubo, T., Heriawan, M. N. & Yamada, R. (2022). Incorporation of geological constraints and semivariogram scaling law into geostatistical modeling of metal contents in hydrothermal deposits for improved accuracy. *Journal of Geochemical Exploration*, *233*, 106901.

Kourgialas, N. N., Karatzas, G. P. & Koubouris, G. C. (2017). A GIS policy approach for assessing the effect of fertilizers on the quality of drinking and irrigation water and wellhead protection zones (Crete, Greece). *Journal of Environmental Management*, *189*, 150–159.

Minitab (2010). *Minitab 17 Statistical software*. State College: Minitab.

Montero, J. M., Fernández-Avilés, G. & Mateu, J. (2015). *Spatial and spatio-temporal geostatistical modeling and kriging*. Hoboken: John Wiley & Sons.

Raju, N. J. (2016). *Geostatistical and geospatial approaches for the characterization of natural resources in the environment challenges, processes and strategies*. Berlin: Springer.

Silva, M. V. da, Pandorfi, H., Almeida, G. L. P. de, Silva, R. A. B. da, Morales, K. R. M., Guiselini, C., Santana, T. C., Cangela, G. L. Ch. de, Filho, J. A. D. B., Moraes, A. S., Montenegro, A. A. A. & Oliveira Júnior, J. F. de (2023). Spatial modeling via geostatistics and infrared thermography of the skin temperature of dairy cows in a compost barn system in the Brazilian semiarid region. *Smart Agricultural Technology*, *3*, 100078.

Sukkuea, A. & Heednacram, A. (2022). Prediction on spatial elevation using improved kriging algorithms: An application in environmental management. *Expert Systems with Applications*, *207*, 117971.

Thanoon, S. R. (2018). Application trend surface models with estimation. *Tikrit Journal of Pure Science*, *23* (10), 118–122.

Xue, S., Korna, R., Fan, J., Ke, W., Lou, W., Wang, J. & Zhu, F. (2023). Spatial distribution, environmental risks, and sources of potentially toxic elements in soils from a typical abandoned antimony smelting site. *Journal of Environmental Sciences*, *127*, 780–790.

Yang, J. W., Chiu, S. Y. & Yen, K. C. (2023). Does the realized distribution-based measure dominate particular moments? Evidence from cryptocurrency markets. *Finance Research Letters*, *51*, 103396.

Summary

Spatial distribution prediction for the ground water quality in Mosul City (Iraq) using variogram equations. The GIS-aided spatial interpolation was applied on collected groundwater data to predict selected parameters (i.e., pH, electrical conductivity, and temperature) for the selected water wells distributed over Mosul City in Iraq. A descriptive statistical analysis was conducted on collected samples to explore the statistical indices. The skewness test was also employed to test the distribution of data sets around their mean values. The natural logarithms function achieved least skewness values and thus was applied to transfer data sets in order to adjust normality of the data sets distribution. Among all applied semivariogram models, the J-Bessel semivariogram model was optimal in terms of root mean square error (*RMSE*) values. The average standard errors were 0.2217, 740.5, and 1.209 for pH, EC, and temperature, respectively.

Instruction for Authors

The journal publishes in English languages, peer-reviewed original research, critical reviews and short communications, which have not been and will not be published elsewhere in substantially the same form. Author of an article is required to transfer the copyright to the journal publisher, however authors retain significant rights to use and share their own published papers. The published papers are available under the terms of the principles of Open Access Creative Commons CC BY-NC license. The submitting author must agree to pay the publication charge (see Charges).

The author of submitted materials (e.g. text, figures, tables etc.) is obligated to restricts the publishing rights. All contributors who do not meet the criteria for authorship should be listed in an Acknowledgements section of the manuscript. Authors should, therefore, add a statement on the type of assistance, if any, received from the sponsor or the sponsor's representative and include the names of any person who provided technical help, writing assistance, editorial support or any type of participation in writing the manuscript.

Uniform requirements for manuscripts

The manuscript should be submitted by the Open Journal System (OJS) at https://srees.sggw.edu.pl/about/submissions. All figures and tables should be placed near their reference in the main text and additionally sent in a form of data files (e.g. Excel, Visio, Adobe Illustrator, Adobe Photoshop, CorelDRAW). Figures are printed in black and white on paper version of the journal (color printing is combined with an additional fee calculated on a case-by-case basis), while on the website are published in color.

The size of the manuscript should be limited up to 10 pages including overview, summary, references and figures (the manuscript more than 13 pages is unacceptable); Please set the text format in single column with paragraphs (A4 paper format), all margins to 25 mm, use the font Times New Roman, typeface 12 points and line spacing one and half.

The submitted manuscript should include the following parts:

- name and SURNAME of the author(s) – up to 5 authors
- affiliation of the author(s), ORCID Id (optional)
- title of the work
- key words
- abstract (about 500 characters)
- text of the paper divided into: Introduction, Material and Methods, Results and Discussion, Conclusions, References and Summary
- references in APA style are listed fully in alphabetical order according to the last name of the first author and not numbered; please find the details below
- post and mailing address of the corresponding author:

  Author's address:
  Name, SURNAME
  Affiliation
  Street, number, postal code, City
  Country
  e-mail: adress@domain

- Plagiarism statement (https://srees.sggw.edu.pl/copyright)

Reference formatting

In the Scientific Review Engineering and Environmental Sciences the APA 6th edition style is used.

Detailed information

More information can be found: https://srees.sggw.edu.pl